

LATERAL MODE RESONATORS FOR IN LIQUID BIOSENSING  
APPLICATIONS WITH A SECOND HARMONIC BASED READ OUT  
METHOD

A THESIS SUBMITTED TO  
THE GRADUATE SCHOOL OF NATURAL AND APPLIED SCIENCES  
OF  
MIDDLE EAST TECHNICAL UNIVERSITY

BY  
EREN AYDIN

IN PARTIAL FULFILLMENT OF THE REQUIREMENTS  
FOR  
THE DEGREE OF MASTER OF SCIENCE  
IN  
ELECTRICAL AND ELECTRONICS ENGINEERING

SEPTEMBER 2017





Approval of the thesis:

**LATERAL MODE RESONATORS FOR IN LIQUID BIOSENSING  
APPLICATIONS WITH A SECOND HARMONIC BASED READ OUT  
METHOD**

Submitted by **EREN AYDIN** in partial fulfillment of the requirements for the degree of **Master of Science in Electrical and Electronics Engineering, Middle East Technical University** by,

Prof. Dr. Gülbin Dural Ünver  
Director, Graduate School of **Natural and Applied Sciences** \_\_\_\_\_

Prof. Dr. Tolga Çiloğlu  
Head of Department, **Electrical and Electronics Engineering** \_\_\_\_\_

Prof. Dr. Haluk Külâh  
Supervisor, **Electrical and Electronics Eng. Dept., METU** \_\_\_\_\_

**Examining Committee Members:**

Prof. Dr. Tayfun Akın  
Electrical and Electronics Engineering Dept., METU \_\_\_\_\_

Prof. Dr. Haluk Külâh  
Electrical and Electronics Engineering Dept., METU \_\_\_\_\_

Assistant Prof. Dr. Kıvanç Azgın  
Mechanical Engineering Dept., METU \_\_\_\_\_

Assistant Prof. Dr. Serdar Kocaman  
Electrical and Electronics Engineering Dept., METU \_\_\_\_\_

Assistant Prof. Dr. Ender Yıldırım  
Mechanical Engineering Dept., Çankaya University \_\_\_\_\_

**Date:** \_\_\_\_\_

**I hereby declare that all information in this document has been obtained and presented in accordance with academic rules and ethical conduct. I also declare that, as required by these rules and conduct, I have fully cited and referenced all material and results that are not original to this work.**

Name, Lastname: Eren Aydın

Signature :

## **ABSTRACT**

### **LATERAL MODE RESONATORS FOR IN LIQUID BIOSENSING APPLICATIONS WITH A SECOND HARMONIC BASED READ OUT METHOD**

Aydın, Eren

M. Sc., Electrical and Electronics Engineering

Supervisor: Prof. Dr. Haluk Külâh

September 2017, 117 pages

This thesis presents design and implementation of lateral mode electrostatic resonators for in liquid biosensing applications and a novel read-out approach for eliminating parasitic feedthrough current and enhance Q of the resonating system at the same time.

The main objective of this thesis is to make resonators operating under when the microchannel is filled with liquid. Liquid injection inside the microchannel of resonators brings lots of mechanical and electrical problems together. These problems are categorized as damping and feedthrough current.

In the scope of this thesis, new resonators are designed suitable for operation under liquid flow optimizing their damping. Calculations show that all types of the designed resonators have Q higher than 45 on liquid.

The designed devices are fabricated using silicon-glass anodic bonding process and coated with 500 nm parylene layer. One type of the tested devices without parylene coating has 590 Q and 330 kHz resonance frequency in air and after parylene coating Q has decreased to 93 and resonance frequency increased to 407 kHz. After liquid injection inside the microchannel Q of the resonator has

decreased to 54 and the resonance frequency of the resonator has increased to 480 kHz. This is the first time illustration of resonance of a lateral mode electrostatic resonator on liquid without postprocessing.

Moreover a new resonance characterization method based on sensing second harmonic component of the resonators is developed. Utilizing this method, feedthrough current is eliminated and resonance peak was increased from 1 dB to 35 dB. Moreover it is shown that this method is suitable for eliminating both capacitive and resistive feedthrough current without using complex resonator design and circuitry. Furthermore this method also improves Q of the resonating system 66%.

**Keywords:** MEMS, resonator, mass sensor, second harmonic, in-liquid biosensing.

## ÖZ

### **SIVI İÇERİSİNDE BİYO ALGILAYICI UYGULAMALARI İÇİN YANAL MODLU REZONATÖRLER VE İKİNCİ HARMONİK TEMELLİ BİR OKUMA YÖNTEMİ**

Aydın, Eren

Yüksek Lisans, Elektrik ve Elektronik Mühendisliği Bölümü

Tez Yöneticisi: Prof. Dr. Haluk Külah

Eylül 2017, 117 sayfa

Bu tez, sıvı içi biyo-algılayıcı uygulamaları için yanal mod elektrostatik rezonatörlerin tasarımını, gerçekleştirmesini ve parazitik kaçak akımını ortadan kaldırarak rezonans sisteminin Q'sunu aynı anda arttırmak için yeni bir okuma yöntemi sunmaktadır.

Bu tezin temel amacı, rezonatörleri sıvı akışı altında çalıştırmaktır. Rezonatörlerin mikrokanalının içindeki sıvı enjeksiyonu, birçok mekanik ve elektriksel problemi birlikte getirir. Bu problemler, sönümleme ve geçiş akımı olarak sınıflandırılır.

Bu tez çalışması kapsamında, yeni rezonatörler, sönümlenmeyi en iyi hale getiren sıvı akış altında çalışacak şekilde tasarlanmıştır. Hesaplamalar, her tür tasarlanmış rezonatörün, sıvı üzerinde 45'in üzerinde Q'ya sahip olduğunu gösterir.

Tasarlanan cihazlar, silikon-cam anodik bağlama yöntemi kullanılarak üretilir ve 500 nm parilen tabakasıyla kaplanır. Parilen kaplamasız test edilen cihazların bir türü havada 590 Q ve 330 kHz rezonans frekansına sahiptir ve parilen kaplamadan sonra Q 93'e düşmüştür ve rezonans frekansı 407 kHz'e yükselmiştir. Rezonatörün

kalite faktörü mikrokanalının içindeki sıvı enjeksiyonu sonrasında, 54'e düşmüş ve rezonatörün rezonans frekansı 480 kHz'e yükselmiştir. Sıvı akışı atında veri üzerinde herhangi bir işlem olmaksızın bir yanal mod elektrostatik rezonatör rezonansı ilk kez gösterilmiştir.

Ayrıca, rezonatörlerin ikinci harmonik bileşenini algılamaya dayanan yeni bir rezonans karakterizasyon yöntemi geliştirilmiştir. Bu yöntemi kullanarak kaçak akımı giderilmiş ve rezonans pik değeri 1 dB'den 35 dB'ye yükseltilmiştir. Dahası, bu yöntemin karmaşık rezonatör tasarımı ve devresi kullanmadan hem kapasitif hem de rezistif kaçak akımını ortadan kaldırmak için uygun olduğu gösterilmiştir. Ayrıca bu yöntem aynı zamanda rezonans sisteminin kalite faktörünü %66 oranında iyileştirir.

**Anahtar Kelimeler:** mikrosistemler, rezonatör, kütle sensörü, ikinci harmonik, sıvı içerisinde çalışan biyo-algılayıcılar,

*To my dearest wife Hilal*

## ACKNOWLEDGEMENTS

I would like to express my deepest thanks to my thesis advisor Prof. Dr. Haluk Kulah for his support, supervision and trust and also for giving the opportunity to be involved in such an exciting project. I would like to extend my thanks to Prof. Dr. Tayfun Akin for his support and for providing the clean room facilities of METU MEMS Research and Application Center.

I would also like to thank our post-master Mustafa Kangül for developing previous techniques and resonator structures. His valuable help, discussions and contributions to my research are much appreciated. I am thankful to Furkan Gökçe for his collaboration in development, fabrication and testing phases of my research. I am also grateful to Taylan Berkin Töral for developing the previous fabrication process and his guidance in clean room. I am gratified to Dr. Özlem Şardan Sukas, Özge Zorlu and Ebru Özgür for their patience and help during my research. I enjoyed sharing my time with the members of BioMEMS and PowerMEMS and their friendship.

My special thanks to METU-MEMS Center staff especially Adem Saraç and Levent Abat. I would also like to thank Orhan Akar for sharing his deep knowledge on microfabrication and for his help in the cleanroom.

Finally, I am grateful to my parents, Handan Aydın and Suhat Aydın for their precious support, enforcement and unconditional love. I also would like thank my brother Ertuğrul Aydın for his friendship. I am also grateful to my parents-in-law Gönül Dumanlı and Prof. Dr. Nazir Dumanlı and my sisters Dr. Sema Dumanlı Oktar, Dr. Ayça Dumanlı Özcan and Dr. Esmâ Dumanlı Kadızade who have always treated me as one of their own. Last but not least I would like to thank my dearest wife Hilal Kübra Dumanlı Aydın by heart for her endless support, love and encouragement. I could not have done it without her.

Note: This work was supported by TUBITAK under grant number 213E024.

## TABLE OF CONTENTS

ABSTRACT.....	v
ÖZ .....	vii
ACKNOWLEDGEMENTS.....	x
TABLE OF CONTENTS.....	xi
LIST OF TABLES .....	xv
LIST OF FIGURES .....	xvi
CHAPTERS	
1.INTRODUCTION .....	1
1.1. Resonant Based Sensors .....	1
1.2. Resonant Based Biosensors .....	6
1.3. Research Objectives and Thesis Organization.....	15
2. THEORETICAL BACKGROUND .....	19
2.1. Theory of Resonance, Single Degree of Freedom (SDOF) Systems..	19
2.1.1. Free Vibration .....	20
2.1.2. Harmonically Forced Vibration .....	21
2.2. Electrostatic Actuation and Sensing .....	24
2.2.1. Electrostatic Actuation.....	25
2.2.2. Electrostatic Sensing.....	29

2.3. Damping Mechanisms Effective on Resonators Operating in Viscous Medium .....	31
2.4. Conclusion .....	35
3. DESIGN OF RESONATORS .....	37
3.1. Design Parameters .....	37
3.1.1. Spring Constant .....	38
3.1.2. Mass.....	39
3.1.3. Damping .....	39
3.2. Design Considerations .....	40
3.2.1. Quality Factor (Q) .....	40
3.2.2. Output Current.....	46
3.3. Resonator Design.....	51
3.3.1. Resonator with Basic Structure (RBS) .....	51
3.3.2. Resonator with Tree Finger Structure (RTFS) .....	52
3.3.3. Differential Resonator with Side Fingers (DRSF) .....	54
3.3.4. Differential Resonator with Parallelogram Shape (DRPS) ...	56
3.4. Effect of Parylene Coating on the operation of resonators.....	57
3.5. Conclusion and Comparison of Designs .....	60
4. FEEDTHROUGH CURRENT ELIMINATION AND SECOND HARMONIC METHOD .....	61
4.1. Feedthrough Current.....	61
4.2. A novel read-out method: Second Harmonic Method.....	64
4.3. The proposed read-out method .....	70

4.4. Conclusion.....	72
5. FABRICATION OF RESONATORS .....	73
5.1. Former Fabrication Process.....	73
5.2. The New Fabrication Process.....	75
5.2.1. Wafer selection and Cleaning .....	77
5.2.2. Coating with an isolation layer .....	78
5.2.3. Metal Routing on Silicon .....	78
5.2.4. Device patterning .....	80
5.2.5. Microchannel and Recess Construction .....	80
5.2.6. Electrode Formation.....	82
5.2.7. Anodic Bonding .....	82
5.2.8. Handle layer and buried Oxide Removal. ....	83
5.2.9. Releasing Suspended Structures .....	84
5.2.10. Parylene Coating .....	84
5.3. Parylene Bonding Process.....	85
5.4. Conclusion.....	87
6. EXPERIMENTAL RESULTS .....	89
6.1. Test Setup and Read-out Circuitry .....	89
6.2. Resonator Characterization Results and Comparison of Experimental Results and Simulation Results.....	92
6.2.1. RBS .....	92
6.2.2. RTFS .....	94

6.2.3. DRSF .....	95
6.2.4. DRPS .....	97
6.2.5. Comparison of Experiments and Simulations .....	97
6.3. Test of parylene coated devices and test under liquid flow.....	99
6.4. Second Harmonic Measurements .....	101
6.5. Conclusion .....	105
7. CONCLUSION AND FUTURE WORK.....	109
REFERENCES .....	113

## LIST OF TABLES

Table 3-1: Comparison of the designed resonator structure .....	60
Table 5-1: The proposed fabrication step with explanations .....	75
Table 6-1: Comparison of calculations with experiments .....	98

## LIST OF FIGURES

Figure 1-1: (a) the schematic view of a MEMS based accelerometer, (b) mathematical model of the accelerometer .....	2
Figure 1-2: Operation principle of a resonant accelerometer [12] .....	3
Figure 1-3: The Foucault pendulum. If an observer is outside of the rotation frame (i.e. the earth), the pendulum swing will be observed as fixed for a particular axis. However if an observer is inside the rotation frame, deviation of swing from a particular axis will be observed due to the Coriolis effect.[12].....	3
Figure 1-4: (a) the schematic view of a vibratory gyroscope, (b) mechanical model of a vibratory gyroscope .....	4
Figure 1-5: Non-contact operation principle of AFM [18].....	5
Figure 1-6: The operation principle of the MEMS resonant strain sensor presented in [7] .....	6
Figure 1-7: Illustration of surface activation for biosensing with different recognition agents [21] .....	7
Figure 1-8: Varius examples of continious flow resonant based biosensing applications. a: piezoelectricly excited millimeter sized cantilever are utilized to detect biological sample [23]. b: streptavidin is detected with a cantilever and optical measurement setup [25]. c: Hepatitis A and Hepatitis C antigens are detected using an array of cantilever and an optical sensing setup including photodiode is proposed [24]. .....	8
Figure 1-9: Sensor response presented in [26] with different solutions .....	9

Figure 1-10: Resonance frequency shift with different concentrations of prostate specific antigens(PSA) [28] .....	10
Figure 1-11: Frequency spectra and sensitivity of the nanoelectromechanical cantilevers. (a) Measured frequency spectra of as fabricated $l=6\mu\text{m}$ oscillator (black), with additional antibody (green) and bacullovirus (red) mass loading. Insets schematically depicts binding of AcV1 to the substrate (left) and immobilization of bacullovirus (right) (b) Frequency shift as a function of the bacullovirus concentration for $6\mu\text{m}$ (black)-, $8\mu\text{m}$ (red)-, and $10\mu\text{m}$ (blue)-long cantilevers. (c) Frequency spectra of control measurements with $l=8\mu\text{m}$ cantilevers (black), with antibodies (green), buffer solution without bacullovirus (blue) and a buffer solution containing bacullovirus of $108\text{pfu/ml}$ concentration (red) [29].....	11
Figure 1-12: SEM photograph of resonator proposed in [30].....	12
Figure 1-13: (a): Illustration of SMR, (b) Measurement with trapping the particle with antibody, (c) measurement with continuous flow [31] .....	12
Figure 1-14: Schematic of the lateral mode resonator proposed in [9].....	13
Figure 1-15: Air trapping method introduced in [33] .....	14
Figure 1-16: Photograph and test result of RoM illustrated in [34].....	14
Figure 2-1: The mathematical model of SDOF system .....	19
Figure 2-2: Illustration of a parallel plate capacitor with related variables .....	25
Figure 2-3: Slide film damping schematic structure .....	32
Figure 2-4: The mechanism of squeeze film damping.....	33
Figure 2-5: The rectangular plate which is exposed to squeeze film damping.....	34
Figure 2-6: Variation of $\beta$ with respect to $B/L$ [42].....	35
Figure 3-1: Conceptual schematic of a lateral mode electrostatic resonator .....	37

Figure 3-2: The schematic of a folded beam .....	38
Figure 3-3: Illustration of damping in resonator-on-microchannel. There are basically three damping factors. When operated in the air, the dominant damping mechanism is squeeze film damping. However since viscosity of water is much higher than air, the dominant damping mechanism becomes slide film damping caused by DI water. ....	40
Figure 3-4: Effect of thickness to Q in air environment.....	42
Figure 3-5: Effect of thickness to Q under liquid flow.....	42
Figure 3-6: Effect of gap on Q in air environment .....	43
Figure 3-7: Effect of gap on Q under liquid flow .....	43
Figure 3-8: Effect of resonator length on Q in air environment.....	44
Figure 3-9: Effect of resonator length on Q in liquid environment.....	44
Figure 3-10: Effect of resonator width on Q in air .....	45
Figure 3-11: Effect of resonator width on Q in liquid environment.....	45
Figure 3-12: Effect of thickness on output current in air .....	47
Figure 3-13: Effect of thickness on the output current in liquid environment .....	47
Figure 3-14: Effect of actuation gap on the output current in air .....	48
Figure 3-15: Effect of actuation gap on the output current in liquid environment .....	48
Figure 3-16: Effect of resonator length on resonator current in air.....	49
Figure 3-17: Effect of resonator length on resonator current in liquid environment .....	49
Figure 3-18: Effect of resonator width on the current in air.....	50

Figure 3-19: Effect of resonator width on the current in liquid environment.....	50
Figure 3-20: Mask drawing of RBS .....	51
Figure 3-21: Calculated frequency response of RBS in air (red) and liquid environment (blue) .....	52
Figure 3-22: Mask drawing of RTFS with related design parameters .....	53
Figure 3-23: Calculated frequency response of RTFS in air (red) and liquid environment (blue) .....	54
Figure 3-24: The schematic of DRSF .....	55
Figure 3-25: Calculated frequency response of DRSF in air (red) and liquid environment (blue) .....	55
Figure 3-26: The schematic of DRPS with related parameters.....	56
Figure 3-27: Calculated frequency response of DRPS in air (red) and liquid environment (blue) .....	57
Figure 3-28: Effect of parylene coating on Q in air environment.....	58
Figure 3-29: Effect of parylene coating on Q of resonator operating under liquid flow .....	58
Figure 3-30: Effect of parylene coating on output current measured in air environment.....	59
Figure 3-31: Effect of parylene coating on output current measured in liquid environment.....	59
Figure 4-1: The feedthrough current elimination method based on utilizing two resonators .....	62
Figure 4-2: The feedthrough current elimination method using differential resonators .....	63

Figure 4-3: Time and frequency domain solutions of nonlinear differential equations with different excitement frequencies. In (a), the resonator is excited with  $\omega_0/2$ . Although it was excited with half of the resonance frequency second harmonic term at the electrostatic force causes second harmonic term at the displacement. In (b), the resonator is excited with  $\omega_0$ . Higher order harmonics components of the force are filtered out by the resonator itself and there is no distortion term. In (c), resonator is excited with 280 KHz excitation signal. Although it is not subharmonic or superharmonic of the resonance frequency resonance frequency component is observed at the displacement due to the transient response of the resonator. In (d) the resonator is excited with  $2\omega_0$  and the resonance frequency component is observed at the spectrum of displacement. ... 67

Figure 4-4: Time and frequency domain solutions of output current expression with different excitement frequencies. In (a) the resonator is excited with  $\omega_0/2$  and the resonance frequency term at the displacement is reflected into the output current. In (b), the resonator is excited with its resonance frequency  $\omega_0$  and despite of the fact that displacement is almost completely linear, there is second harmonic term at the output due to the nonlinearity of sensing mechanism. In (c) the resonator is excited with 280 KHz signal and the resonance frequency term at the displacement is reflected into output current term. In (d) the resonator is excited with  $2\omega_0$  but the resonance frequency term observed at the displacement term is reflected into output current term. .... 69

Figure 4-5: The schematic of the proposed method ..... 71

Figure 4-6: Magnitudes of second harmonic and main tone signals with different excitement frequencies ..... 72

Figure 5-1: The former fabrication process of resonators[35] ..... 74

Figure 5-2: Patterned SiO<sub>2</sub> layer on the silicon surface. As seen, BHF etching is isotropic and corners are rounded due to the overcut of BHF..... 79

Figure 5-3: Photograph of the silicon surface after lift-off process .....	79
Figure 5-4: Microscope views of patterned devices .....	80
Figure 5-5: SEM images of patterned devices and various regions of wafer. As seen, 2 $\mu\text{m}$ gap is achieved and scallops on the walls are observed .....	80
Figure 5-6: Microchannel and recess opened on glass wafer .....	81
Figure 5-7: Electrodes constructed on the glass wafer.....	82
Figure 5-8: Contact regions of metals and resonating devices after anodic bonding .....	83
Figure 5-9: microscope views of suspended resonators.....	84
Figure 5-10: Pads and microchannel inlets after breaking the lids .....	84
Figure 5-11: Cross section of wafers and process masks.....	86
Figure 5-12: Parylene bonding process proposed by Gokce et. al. [48] .....	87
Figure 5-13: Fabricated die photographs (left: top view, right: bottom view).....	88
Figure 6-1: The test setup with probe station.....	90
Figure 6-2: Image of the holder designed to test resonators. After resonators are placed inside the chip housing front cover is closed on the back cover. Electrical and microfluidic connections are done from the front cover. Liquid flow may be observed from the microscope hole. ....	91
Figure 6-3: Schematics of inverting (a) and noninverting (b) transimpedance amplifiers.....	92
Figure 6-4: Schematic of second harmonic measurement setup .....	93
Figure 6-5: Raw frequency response of RBS taken from the network analyzer...	93
Figure 6-6: Postprocessed characterisation of RBS .....	94

Figure 6-7: Raw frequency response of RTFS taken from the network analyzer	95
Figure 6-8: Postprocessed resonance characteristics of RTFS	95
Figure 6-9: Raw frequency response of DRSF taken from the network analyzer	96
Figure 6-10: Postprocessed resonance characteristics of DRSF	96
Figure 6-11: Raw frequency response of DRPS taken from the network analyzer	97
Figure 6-12: Postprocessed resonance characteristics of DRPS	98
Figure 6-13: The test result of parylene coated device. Resonance frequency increased after parylene coating. This means parylene coating does not only increase the damping coefficient also increases the spring constant	99
Figure 6-14: Postprocessed test result of parylene coated RBS	100
Figure 6-15: Raw frequency response of RBS taken from the network analyzer after liquid injection inside the microchannel	100
Figure 6-16: Postprocessed resonance characteristics of RBS when liquid injected inside the microchannel	101
Figure 6-17: Second harmonic characterization of RBS	102
Figure 6-18: Characterization of RBS performed with the traditional method	103
Figure 6-19: Characterization of resonators with second harmonic method (left), and the traditional method (right) when an external 6 M $\Omega$ resistance is connected between the drive and sense electrodes of the resonator	104
Figure 6-20: Characterization of resonators with second harmonic method (left), and the traditional method (right) when an external 6 M $\Omega$ resistance and 1 pF capacitor is connected between the drive and sense electrodes of the resonator	104
Figure 6-21: Postprocessed data extracted from second harmonic measurements	105

Figure 6-22: Resonance characteristics of RBS under different conditions ..... 106

Figure 6-23: Postprocessed test results of RBS in air environment with the traditional method and second harmonic method ..... 107



## CHAPTER 1

### INTRODUCTION

“If you want to understand the universe, you should think in terms of energy, frequency and vibration.” says N. Tesla. A resonator designer requires also thinking in terms of energy, frequency and vibration. Therefore designing a resonator is a big step of understanding the universe.

Resonating structures have great importance in daily lives of people. For example a violin has four strings which resonate in different frequencies. A violin player changes resonance frequency of strings pressing fingers to fingerboard to create different notes. As a result, people can hear music.

Resonating structures have found themselves applications in micro-nano technology as well. MEMS based resonators have lots of utilization areas such as High Q filters[1]-[2], gyroscopes [3]-[4], accelerometers[5]-[6], strain sensors[7], AFM probes [8] or mass sensors[9]-[10] .

#### **1.1. Resonant Based Sensors**

One of the most common utilization areas of MEMS resonators is inertial sensors: accelerometers and gyroscopes. Inertial sensors transform linear or angular motion into electrical signals. While accelerometers sense axial acceleration, gyroscopes measure rate of rotation. Utilization of these sensors together leads 6 degree of freedom inertial measurement unit (IMU) [11]. Such units are used in

navigation systems in enclosed regions where GPS signals are not available. In Figure 1-1(a) the schematic of a MEMS based accelerometer and in Figure 1-1 (b) mathematical model of the accelerometer , the schematic of a single axis accelerometer is shown [12].

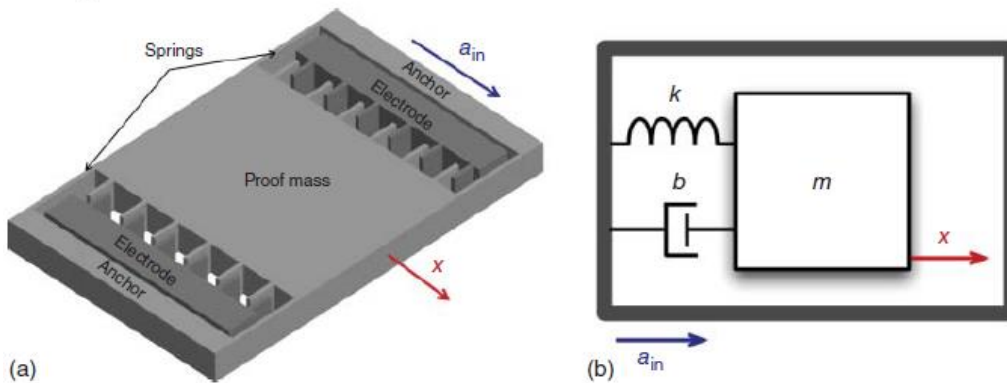


Figure 1-1: (a) the schematic view of a MEMS based accelerometer, (b) mathematical model of the accelerometer

As seen from Figure 1-1(a), a MEMS accelerometer is composed of a movable proof mass which is anchored to a reference frame with springs. Therefore, it can be modeled as a second order spring-mass-damper system as shown in Figure 1-1 (b). When the reference frame moves, an inertial force is exerted on the movable proof mass. Consequently, the movable proof mass moves. The motion of proof mass is sensed by measuring the capacitance between electrodes and proof mass. Q factor of designed system should be high and operation frequency should be lower than the operating frequency to have a frequency independent response and eliminate effect of damping and. As a result, acceleration force can be measured properly. Measuring static response of the resonant system is not the only method of sensing accelerometer. Another way of implementing an accelerometer is making movable proof mass self-oscillate at its resonance frequency. In Figure 1-2, working principle of a resonant accelerometer is illustrated [12]. As a result of the inertial force, torsion-spring will pull or push the resonator beam which will

result in softening and hardening of the beam. As a result of change in spring constant, self-oscillation frequency will change. Acceleration can be computed using oscillation frequency. [13] and [14] are examples of resonant accelerometers.

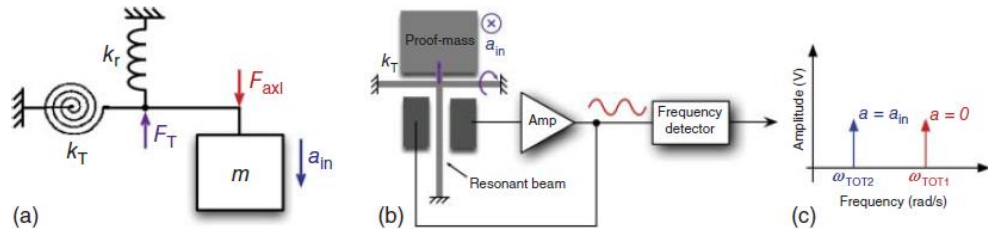


Figure 1-2: Operation principle of a resonant accelerometer [12]

Gyroscopes are another popular inertial sensors implemented utilization of resonators. Gyroscopes respond to rotation rate using Coriolis force [12]. The operation principle of gyroscopes can be understood considering Foucault pendulum [12] as shown in Figure 1-3.

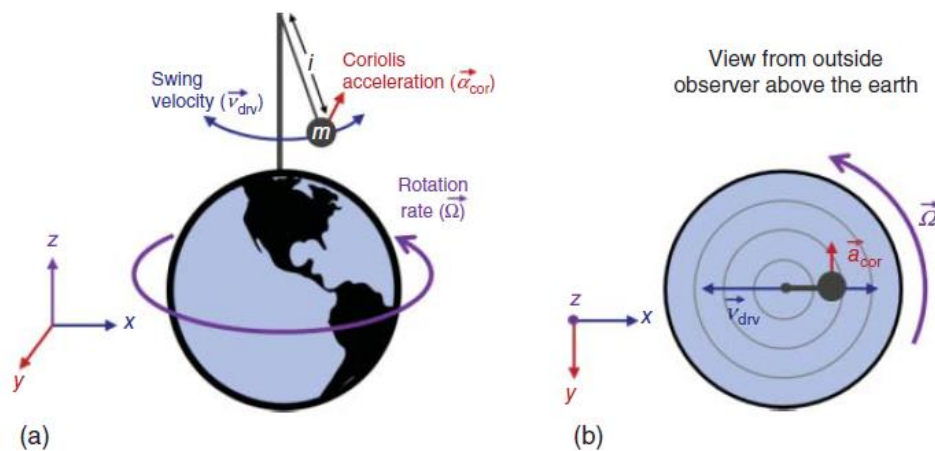


Figure 1-3: The Foucault pendulum. If an observer is outside of the rotation frame (i.e. the earth), the pendulum swing will be observed as fixed for a particular axis. However if an observer is inside the rotation frame, deviation of swing from a particular axis will be observed due to the Coriolis effect. [12]

In Figure 1-4, schematic of a vibratory gyroscope is illustrated [12]. The device is composed of two movable proof masses anchored to a substrate with springs that allows proof masses displace in both x and y directions. The proof masses are excited in x axis out of phase to eliminate common mode signals. If an angular velocity is applied to this system around z axis, the proof masses will experience Coriolis force that makes them move in y axis. Using different sensing methods, movement will be sensed and then converted into angular velocity. A vibratory gyroscope can be modeled as two independent and orthogonal second order systems that disturb each other in the presence of Coriolis force.

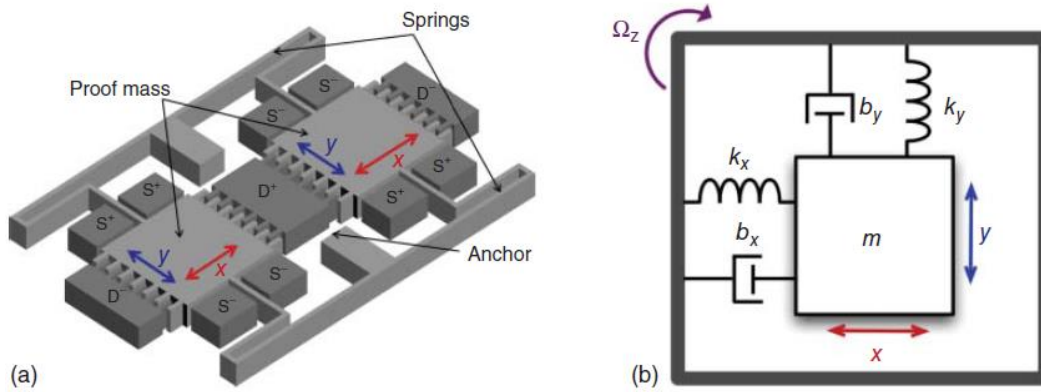
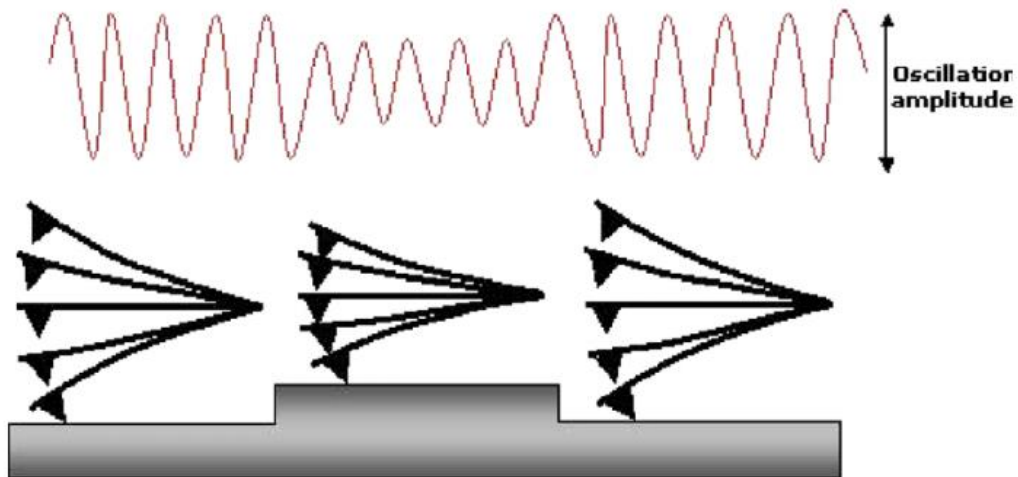


Figure 1-4: (a) the schematic view of a vibratory gyroscope, (b) mechanical model of a vibratory gyroscope

Gyroscopes can be implemented different resonator types such as tuning fork gyroscopes [15], resonating star gyroscopes [16], bulk acoustic wave gyroscopes [17].

Another utilization area of resonators is atomic force microscopes. Atomic force microscopes are used to measure profile of a surface. An AFM probe basically consists of a cantilever and a tip placed to the cantilever. Basically AFM probe is vibrated very close to the measured surface. Atomic forces applied to probe tip affects the operation of cantilever. If the cantilever is driven at constant frequency,

vibration amplitude changes with changing profile. If the cantilever is vibrated at constant amplitude, vibration frequency changes with changing surface profile. In Figure 1-5 the resonator oscillates with constant frequency and oscillation amplitude changes with surface profile [18].



*Figure 1-5: Non-contact operation principle of AFM [18]*

Strain sensors are another resonant based sensors utilized in many applications. The operation principle of such sensors is similar to resonant accelerometers. A beam is self-oscillated using positive feedback. If a tensile or compressive force is applied to the beam, resonance frequency of beam will change. Observing resonance frequency, even small strains can be sensed easily. In Figure 1-6, an example of strain sensor is shown [7].

MEMS resonators are also utilized in energy harvesting applications. Increasing displacement causes more energy storage for mechanical energy harvesters. Therefore, vibration in resonance frequency increases efficiency of energy harvester. Piezoelectric materials with cantilevers are widely used for MEMS energy harvesters [19]. To increase bandwidth of energy harvester more than one resonator can be coupled each other[20].

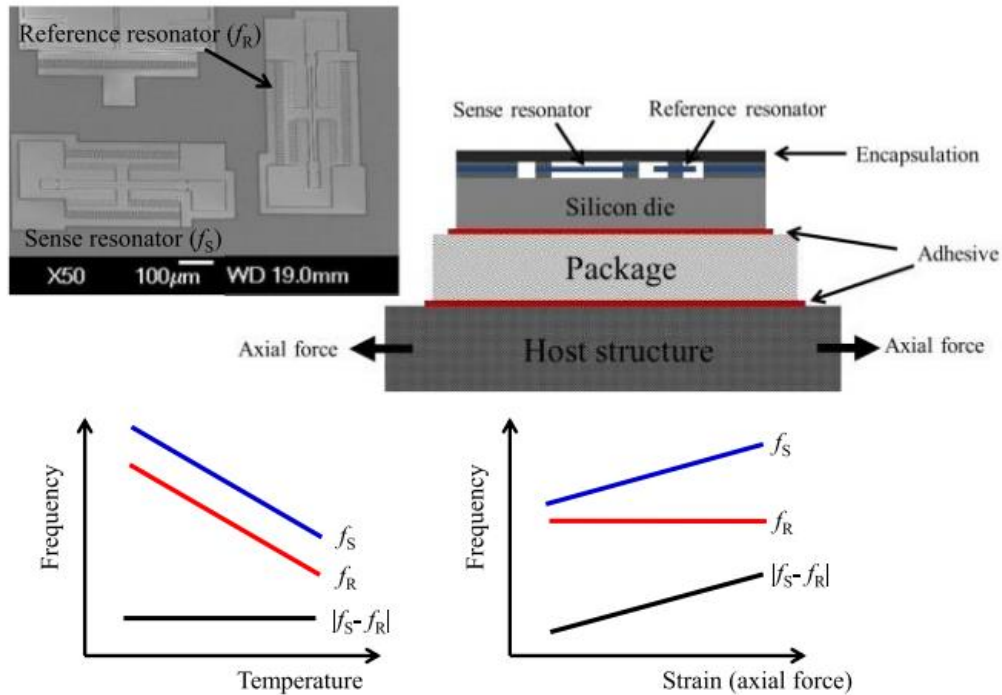


Figure 1-6: The operation principle of the MEMS resonant strain sensor presented in [7]

## 1.2. Resonant Based Biosensors

Biosensors using MEMS resonators are generally based on mass change of resonating structure. Since resonance frequency of resonator depends on mass, mass change results in resonance frequency shift. To use a resonator as a biosensor, biosensors surface should be functionalized for selective recognition.

Functionalization of biosensors surface is basically three steps: preparation, immobilization, and passivation [21]. Firstly the surface which biological reactions will occur should be prepared with chemical modification to create a facilitating reactive layer unless the resonator surface has proper reactive groups for immobilization of bio-recognition agent. After preparation of surface, recognition agents should be immobilized to the surface of resonator in an

orientation so that target molecule binds to the surface easily. The last step of surface functionalization is passivation. Passivation process is performed in case there are bare regions which may cause non-selective binding. Therefore such regions should be passivated to prevent non-selective binding processes. As recognition agents different molecules such as antibodies or nucleic acids can be used. In Figure 1-7 [21], functionalized surfaces with different recognition agents are exemplified.

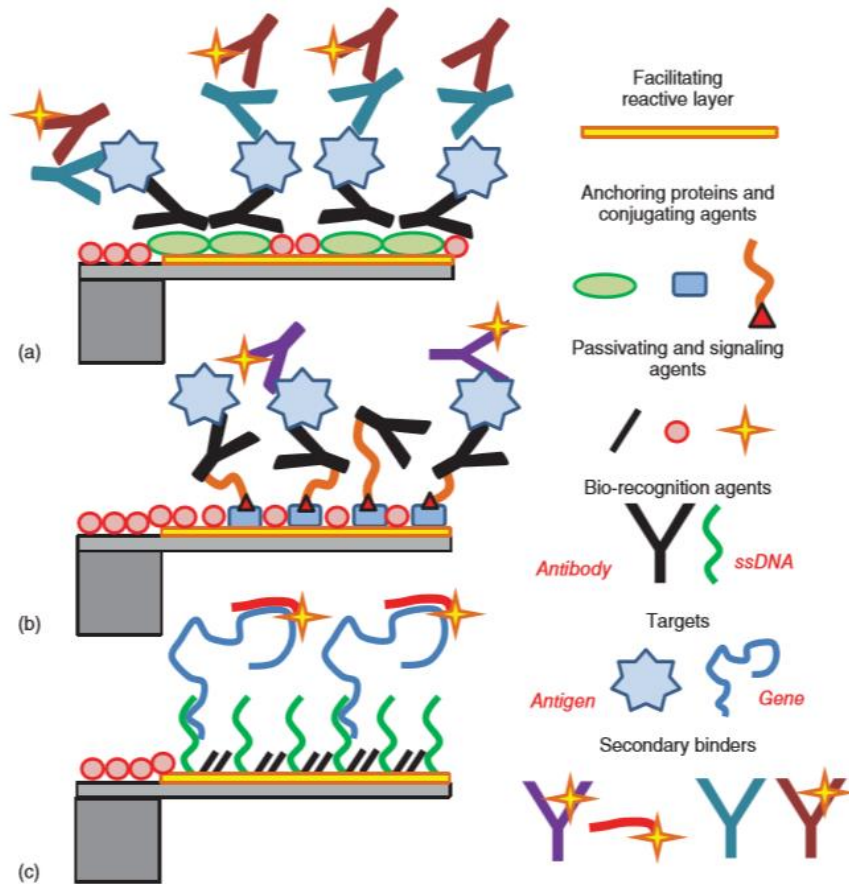


Figure 1-7: Illustration of surface activation for biosensing with different recognition agents [21]

Basically there are two operation methods for resonant based biosensors: Dip-Dry-Measure Method [22] and Continuous Flow Method [23], [24]. As understood from the name, in Dip-Dry-Measure method, functionalized biosensor is immersed in a sample and then removed, rinsed and dried. After drying the sensor, resonant frequency of the resonator is measured again. Although this method is the simplest measurement technique, it may not be reliable for all the time. If target molecule is affected from rinsing or drying, this method is not applicable. For example if growth of a cancer cell will be measured using resonant biosensor, this method may not be suitable since drying of sensor may cause death of cancer cell. The second method is continuous flow method. This method is much more reliable than the dip-dry-measure method since in this method, resonant sensor is self-oscillated and sample liquid flows continuously. Therefore after catching target molecules, no extra treatment is required. Self-oscillation frequency is tracked and then amount of target molecule in the sample may be computed. In Figure 1-8, continuous flow method is explained with examples.

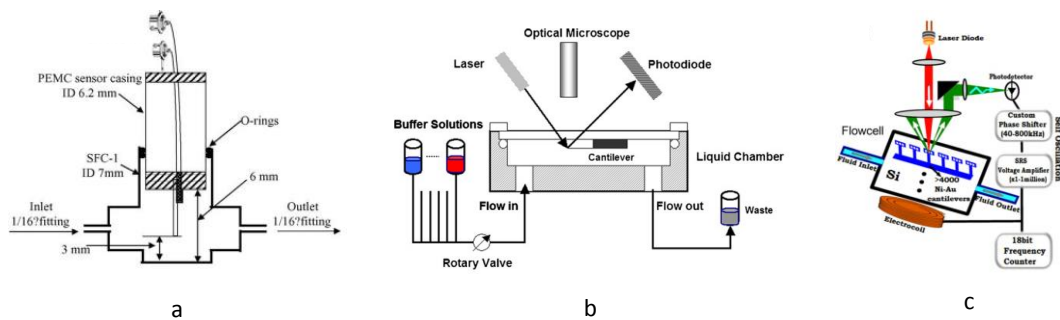


Figure 1-8: Various examples of continuous flow resonant based biosensing applications. a: piezoelectrically excited millimeter sized cantilever are utilized to detect biological sample [23]. b: streptavidin is detected with a cantilever and optical measurement setup [25]. c: Hepatitis A and Hepatitis C antigens are detected using an array of cantilever and an optical sensing setup including photodiode is proposed [24].

Functionalizing resonator surface, resonators can be used as biosensors in a wide range of applications. Foodborne pathogen detection is one of the important applications. For example, *Listeria monocytogenes* is an important foodborne pathogen that can cause high mortality rate (30 %). In [26], Sharma and Mutharasan are proposed a biosensor detecting *Listeria monocytogenes* in milk and buffer solution. Minimum detectable cell concentration of this sensor is 100 cells/ml. The sensor used in this work is presented in [27]. In Figure 1-9, sensor response for various concentrations of *Listeria monocytogenes* in PBS and 25% milk concentration is illustrated. As seen from Figure 1-9, more cells can be caught in PBS compared to milk.

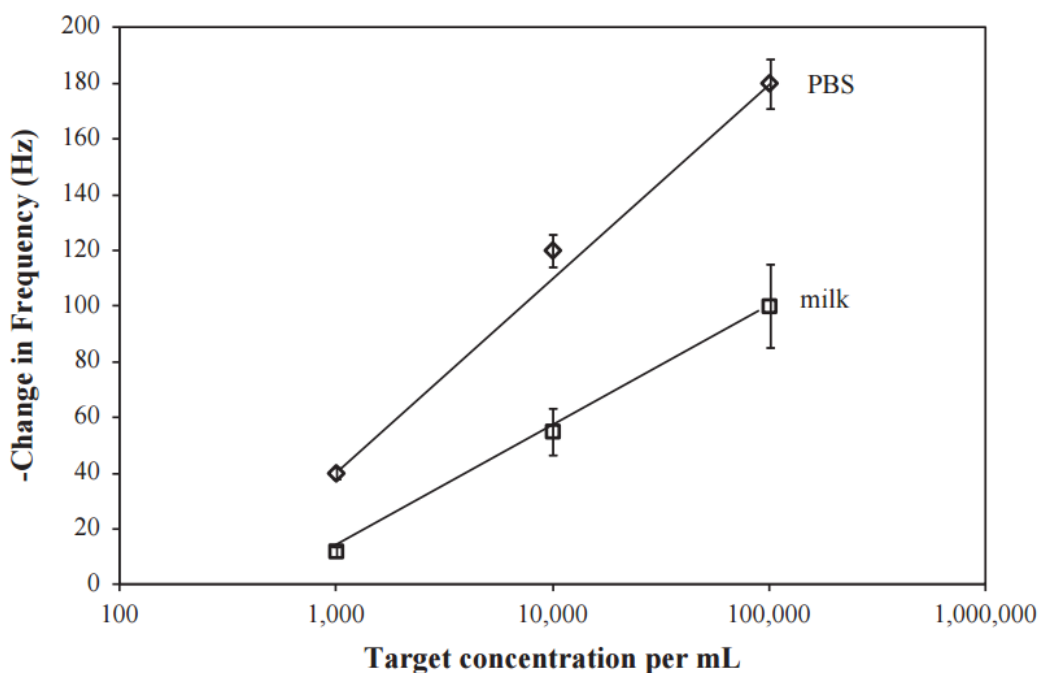


Figure 1-9: Sensor response presented in [26] with different solutions

Resonant biosensors may be used to detect cancer biomarkers as well. In [28], PZT resonators are utilized for label-free detection of prostate specific antigens with 10 pg/ml sensitivity. In Figure 1-10, resonance frequency change in different

concentration of prostate specific antigens is given. As seen from the figure, resonance frequency shift depends on PSA concentration. Using such sensors, prostate cancer can be detected easily.

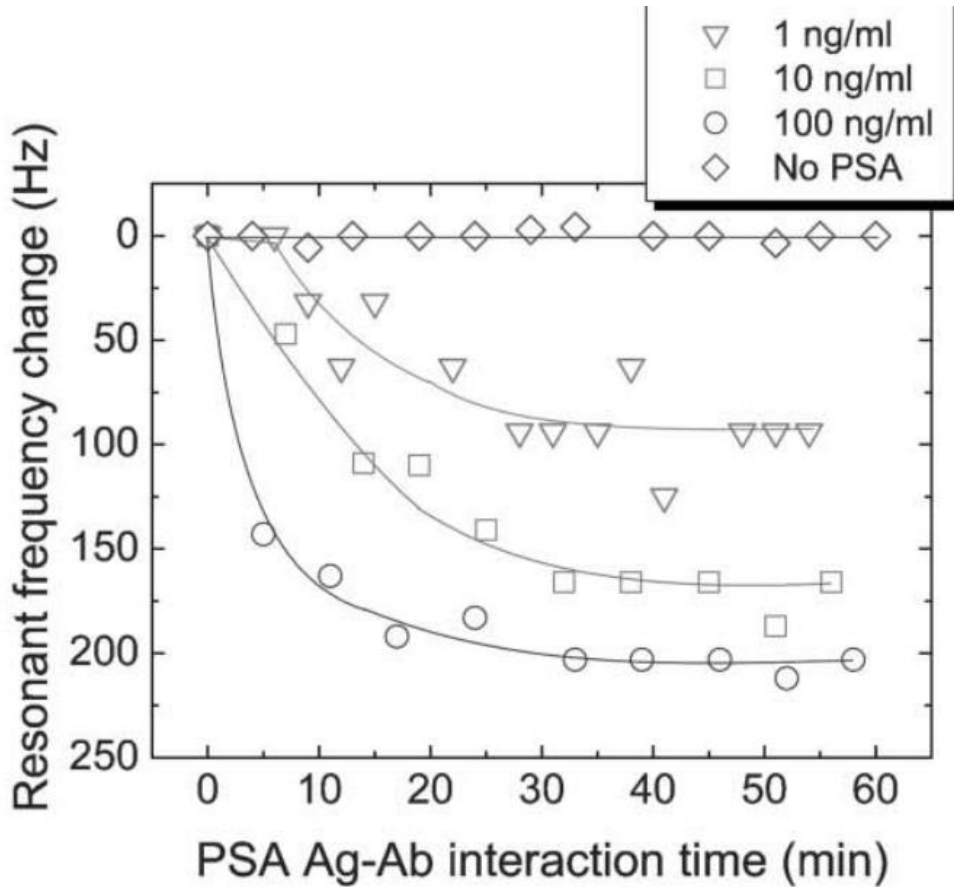


Figure 1-10: Resonance frequency shift with different concentrations of prostate specific antigens(PSA) [28]

Another important biosensing application area of resonant biosensors is, virus detection [24], [29]. In Figure 1-11, a biosensors for virus detection is shown. The proposed sensors are fabricated with polysilicon deposited on SiO<sub>2</sub> sacrificial layer. As seen from Figure 1-11, resonance frequency shifts left when virus attached to the sensor surface.

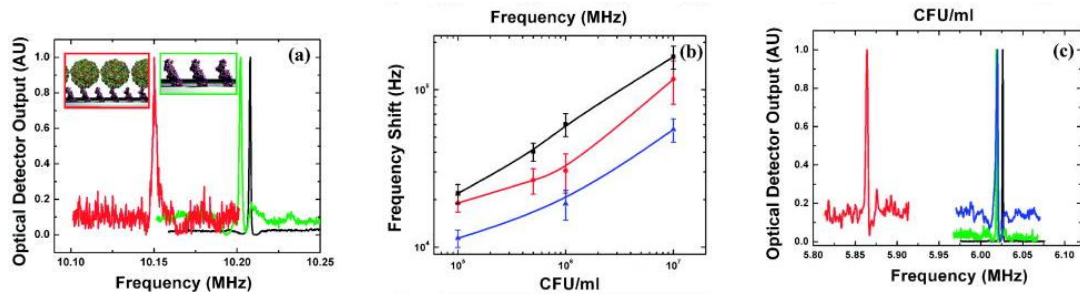


Figure 1-11: Frequency spectra and sensitivity of the nanoelectromechanical cantilevers. (a) Measured frequency spectra of as fabricated  $l=6\mu\text{m}$  oscillator (black), with additional antibody (green) and baculovirus (red) mass loading. Inset schematically depicts binding of AcV1 to the substrate (left) and immobilization of baculovirus (right) (b) Frequency shift as a function of the baculovirus concentration for  $6\text{-}\mu\text{m}$  (black)-,  $8\text{-}\mu\text{m}$  (red)-, and  $10\text{-}\mu\text{m}$  (blue)-long cantilevers. (c) Frequency spectra of control measurements with  $l=8\mu\text{m}$  cantilevers (black), with antibodies (green), buffer solution without baculovirus (blue) and a buffer solution containing baculovirus of  $108\text{pfu/ml}$  concentration (red) [29].

Cantilever structures given in the literature, has some problems, one of the most important issue is mass nonuniformity. Mass sensitivity of cantilevers depends on the target position. Whereas mass sensitivity is higher at the tip of cantilevers, regions close to substrate have lower mass sensitivity. This situation poses a problem especially for particle or cell counting applications. To solve this problem sensing area may be designed smaller but this solution causes inefficient utilization of sensors. To solve mass nonuniformity problem, Park et. al. proposed a cantilever-like sensor. This sensor vibrates at z direction and experimental results indicate that 4.5% difference between maximum and minimum average mass [30]. In Figure 1-12, SEM photograph of the proposed sensor is given. However the given resonator may be overdamped under liquid flow. Achieving high Q is a challenging task under liquid flow. Suspended microchannel resonators are very neat solution to enhance Q of cantilevers under liquid flow.

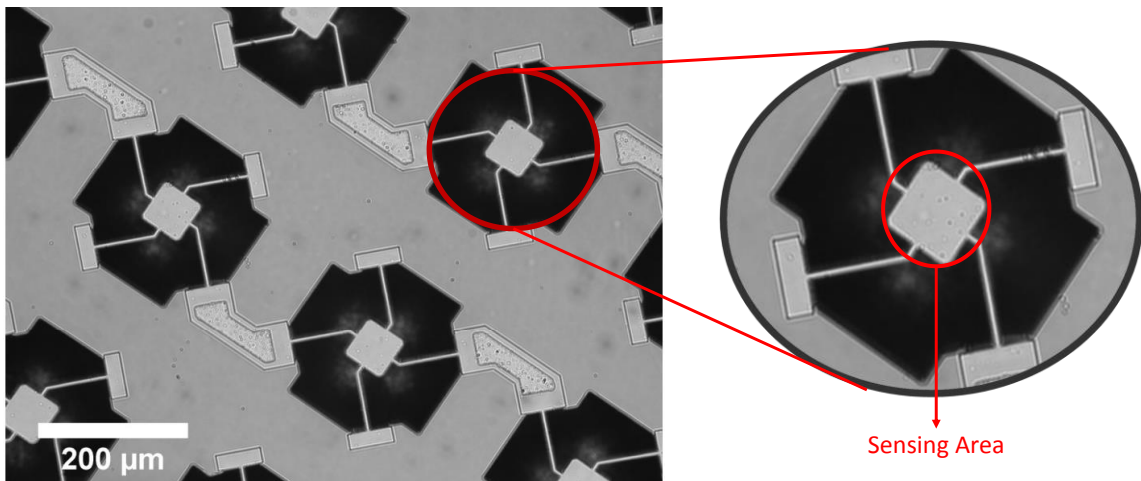


Figure 1-12: SEM photograph of resonator proposed in [30]

Suspended microchannel resonators (SMR) can be operated under vacuum or air. As a result of eliminating liquid environment around the cantilever, effect of viscous damping is avoided. Utilizing SMRs fluid density measurements, protein detection, single cell detection, single cell growth observation applications can be achieved. Burg et al. proposed an SMR for weighing biomolecules, single cells and nanoparticles [31]. Q of such resonators is measured about 15000 and total resonator mass is 100 ng. In Figure 1-13, operation principle of SMRs is given.

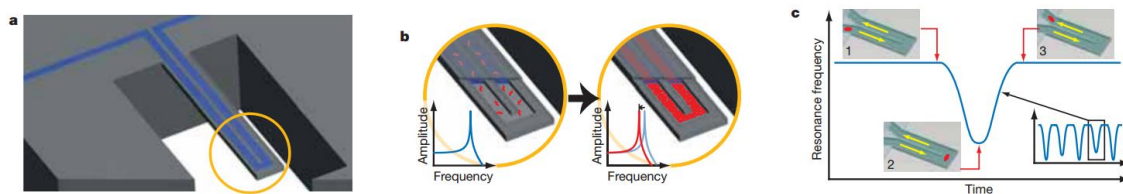
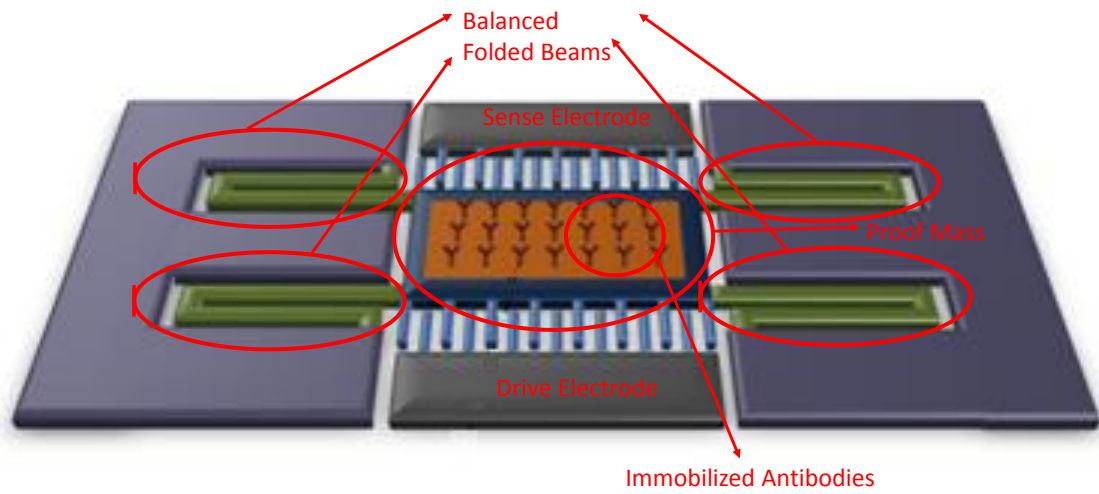


Figure 1-13: (a): Illustration of SMR, (b) Measurement with trapping the particle with antibody, (c) measurement with continuous flow [31]

Basically there are two different measurement methods in SMRs. In the first method walls of microchannel is functionalized and as a result of target binding, frequency response of cantilever changes permanently. In the other method when a target pass from microchannel resonance frequency decreases with time. After

the targets passes whole microchannel, resonance frequency turns back to its other value. However the last method does not give to measure specific detection.

Although SMRs have very high Q compared to its counterparts, microchannel height cannot be higher than a few micrometers due to its fabrication limits. Most biological targets are larger than the height of SMRs. For example a circulating tumor cell (CTC) has a diameter around 15  $\mu\text{m}$ . To achieve resonant based sensing of such targets a laterally resonating structure is proposed [9]. In Figure 1-14 the schematic of the structure proposed in [9] is given.



*Figure 1-14: Schematic of the lateral mode resonator proposed in [9]*

A PDMS microchannel is placed on the top of the resonator. Resonator moves laterally to eliminate squeeze film damping due to liquid flowing through the microchannel. The cells are caught by immobilized antibodies. Mass change results in resonant frequency shift as mentioned in other applications.

It is also shown that the effect of added mass on resonance frequency is position independent. In [32] only 1.9% standard deviation is observed when a microbead is placed on the top of the resonator surface. One of the major problems of laterally moving resonators is liquid leakage between actuation gaps while

working under liquid flow. This problem is solved via air trapping method which is proposed in [33]. With thin parylene-c coating liquid leakage is prevented as shown in Figure 1-15.

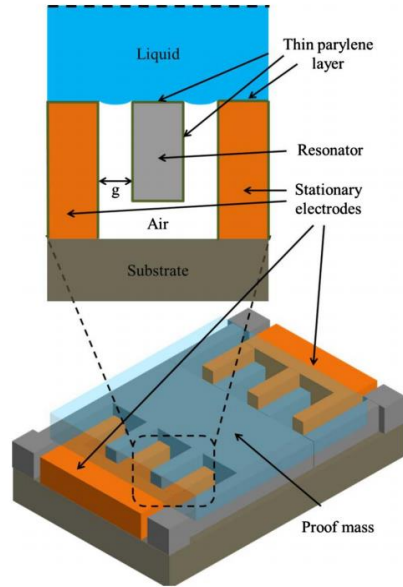


Figure 1-15: Air trapping method introduced in [33]

Instead of PDMS microchannel, resonator structures are anodically bonded to glass microchannels. Such structures are named as resonator-on-microchannel (RoM) [34]. Kangul et.al proposed the first RoM in 2016. The proposed device has Q 100 and 50 in air and liquid environment respectively. In Figure 1-16, photograph and resonance characteristics of RoM are shown.

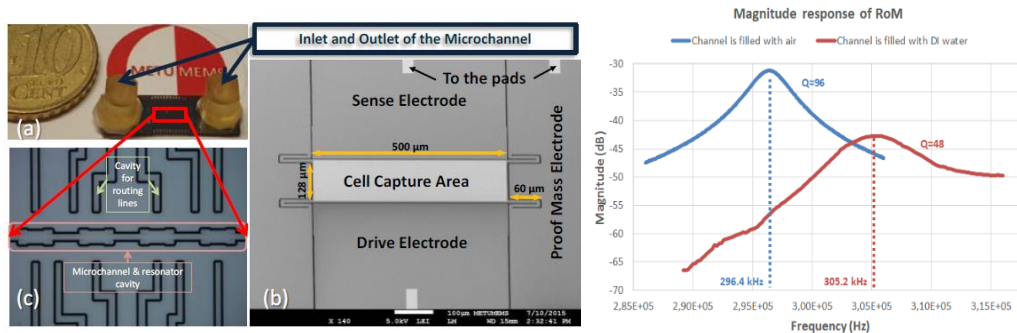


Figure 1-16: Photograph and test result of RoM illustrated in [34]

In this section, resonant based sensing platforms and resonators for biosensing applications are mentioned and high impact studies are exemplified. It is seen resonators are used widely in biosensing applications. Moreover in liquid sensing dramatic drop of quality factors is observed which results lack of sensitivity of the sensor. To increase quality factor, SMRs were proposed but SMRs are not good choices for large bio-particle sensing applications. For cell detection purposes lateral mode resonators are proposed and Kangul et. al achieved in liquid operation resonators embedded on microchannel wall for the first time in the literature. Although in liquid operation has achieved, the resonance characteristics could not be observed for real time or without any postprocessing. To achieve this, resonator structures should be optimized in terms of output current and quality factor. To achieve higher mass resolution, mass of resonating structure should be also decreased. In this thesis optimization of resonating structures is achieved and a new read-out approach is developed. Problems of current sensors and solution of the problems will be given in the following chapters.

### **1.3. Research Objectives and Thesis Organization**

The purpose of this thesis to design, fabricate and test of MEMS based electrostatic resonators that embedded on top wall of a microchannel for in liquid biosensing applications. These sensors are aimed to be used in Circulating Tumor Cell (CTC) sensing applications. Proposed sensor structures may also be used in bacteria sensing, cell growth observation or chemical target detection applications.

Considering the review and discussion from the previous chapter main research objectives can be listed as follows:

1. Development a mathematical model for liquid damping on resonators,
2. Investigation of the effect of resonator dimensions and additional structures on Quality factor and transconductance,

3. Design and fabrication of resonators embedded on top wall of a microchannel that are able to operate properly under liquid flow,
4. Development of a read-out system that enhances sensing performance of resonating systems,
5. Achievement of proper operation of resonating devices under liquid flow.

The first item in the list above is to understand dynamics of resonator performance deeply and insight to resonator operation. To improve performance of resonators and develop a resonator that properly operates under liquid flow, effect of resonator on the performance of resonators should be discussed in detail and reasons why other researchers could not achieve this goal should be figured out. Thus the second and third items in the list aim to improve the resonator performance. The sensing performance of sensors does not only depend on performance of sensors but also depends on the performance of read-out electronics. Read-out electronics also can enhance performance of the overall sensing system. In the fourth item, a novel read-out method is aimed. Finally achieving the four it is aimed to make resonators operate on liquid as mentioned in the fifth item on the list. In order to achieve the aims mentioned above the following works are planned and realized.

1. Modeling of resonators and liquid damping mechanisms effective on the resonating structures.
2. Design of new resonator structures and optimization of these structures to achieve maximum Q and transconductance on liquid
3. Development and realization of a fabrication process to manufacture the designed resonators
4. Development of a novel read-out method to eliminate feedthrough current without changing the sensor structure (without addition of new electrodes or changing the resonance mode) and enhancing Q of the resonating system.

5. Test setup for resonator tests
6. Verification of the new read-out method
7. Test of resonators under liquid flow

This thesis is organized as follows:

Chapter 2 gives the required theoretical background. Second order mass spring damper systems are analyzed and then effect of damping and damping mechanisms effective on lateral mode resonators under liquid flow are investigated. After analysis of damping, actuation and sensing methods are given and capacitive actuation and sensing are studied in detail.

In Chapter 3 resonator design is investigated in detail. First of all design consideration and tradeoffs between design considerations are mentioned. After analyzing design considerations, calculation of design considerations is determined. Resonator structures proposed in [35] is optimized using the mathematical model. After the optimization, optimized resonators are proposed.

In Chapter 4, feedthrough elimination methods from literature are analyzed and effect of liquid flowing through microchannel on feedthrough current is analyzed in detail. After the analysis a new read-out method eliminating both capacitive and resistive feedthrough currents and enhancing Quality factor of resonator system is proposed and mathematical calculations is given.

In Chapter 5, fabrication flow of resonating structures is given. Drawbacks of the previous fabrication processes are analyzed and addition of new process steps to the previous fabrication process is mentioned.

In Chapter 6, test results of newly designed resonators are presented. Characterization of resonators in air and liquid environments using new and traditional read-out methods are shown and these methods will be compared experimentally. After characterization mass measurement and cell counting test results will be given and experimental and theoretical results will be compared.

Finally Chapter 7 concludes this thesis. Research achievements and future work suggestions are given

## CHAPTER 2

### THEORETICAL BACKGROUND

In this chapter, theoretical background of the designed sensor and mathematical analysis is presented. First of all, theory of resonance and single degree of freedom systems are analyzed and related theoretical information to design a micro-resonator is given. After resonance theory, electrostatic actuation and sensing is investigated in detail and nonlinearity sources of actuation and sensing is mentioned briefly. Finally damping mechanisms effective on resonators operating in viscous media is studied in detail.

#### 2.1. Theory of Resonance, Single Degree of Freedom (SDOF) Systems

Most MEMS based resonators may be modeled as SDOF mass-spring-damping system as shown in Figure 2-1, since their vibrational response can be described in terms of a single time-dependent position coordinate.

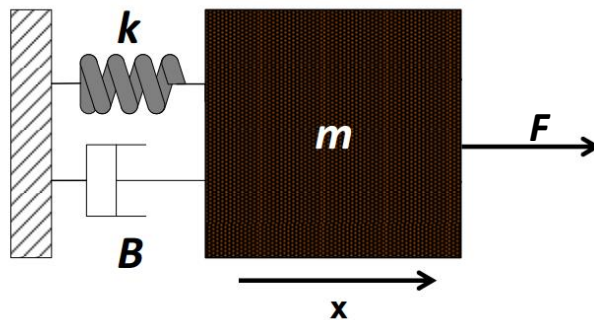


Figure 2-1: The mathematical model of SDOF system

To model resonators correctly and understand the behavior, we need to assume that energy loss is due to a viscous damping mechanism (proportional to velocity), effective mass, spring constant and damping constants are constant (not depend on time and frequency) and the system is linear. Under these conditions equation of motion can be written in Equation (2-1

$$m\ddot{x}(t) + b\dot{x}(t) + kx(t) = F(t) \quad (2-1)$$

### 2.1.1. Free Vibration

In free vibration case there is no external force and Eq. 1 can be modified as Equation (2-2.

$$m\ddot{x}(t) + b\dot{x}(t) + kx(t) = 0 \quad (2-2)$$

Using the coefficients in Equation (2-2, we can define dynamic properties of the system, natural frequency ( $\omega_0$ ) and the damping ratio ( $\zeta$ ) in Equations (2-3and (2-4.

$$\omega_0 = \sqrt{\frac{k}{m}} \quad (2-3)$$

$$\zeta = \frac{b}{2\sqrt{km}} \quad (2-4)$$

For the cases damping ratio is less than unity the system is called as underdamped and this is the case for most MEMS resonators. Free vibration of underdamped resonators can be defined as Eq.5.

$$x(t) = e^{-\zeta\omega_0 t} (A\cos(\omega_d t) + B\sin(\omega_d t)) \quad (2-5)$$

Where  $\omega_d$  is damped natural frequency and  $A$  and  $B$  are the constants depending on initial conditions of the system.

$$\omega_d = \omega_0 \sqrt{1 - \zeta^2} \quad (2-6)$$

For the small values of damping ratio ( $\zeta < 0.2$ ), damped natural frequency and resonance frequency are almost the same.

Another way of expressing how the resonant system is damped is Quality factor (Q). Q is defined in Equation (2-7):

$$Q = \frac{1}{2\zeta} = \frac{\sqrt{km}}{b} \quad (2-7)$$

### 2.1.2. Harmonically Forced Vibration

In this case, the resonator is driven with a harmonic force. And the motion equation is expressed as in Equation (2-8).

$$m\ddot{x}(t) + b\dot{x}(t) + kx(t) = F_0 \cos(\omega t) \quad (2-8)$$

The steady state solution of Equation (2-8) is:

$$x(t) = \frac{F_0}{k} D(r, \zeta) \sin(\omega t + \theta(r, \zeta)) \quad (2-9)$$

where

$$r = \frac{\omega}{\omega_0} \quad (2-10)$$

$$D(r, \zeta) = \frac{1}{\sqrt{(1-r^2)^2 + 2\zeta^2 r^2}} \quad (2-11)$$

$$\theta(r, \zeta) = \arctan\left(\frac{2\zeta r}{1-r^2}\right) \quad (2-12)$$

The exact resonant frequency of the system can be found the frequency which Equation (2-11) is maximized as shown in Equation (2-13).

$$\omega_{res} = \omega_0 \sqrt{1 - 2\zeta^2} \quad (2-13)$$

The maximum value of  $D_{max}$  can be calculated as in Equation (2-14).

$$D_{max} = \frac{1}{2\zeta\sqrt{1-\zeta^2}} \quad (2-14)$$

For an underdamped system,  $D_{max}$  occurs very close to  $r=1$ , and in this case,  $D_{max}$  can be estimated as in Equation (2-15).

$$D_{max} \approx \frac{1}{2\zeta} = Q \quad (2-15)$$

As inferred from Equation (2-15)  $Q$  of system can be estimated experimentally from resonance plot using resonant amplification method [36]. The ratio of maximum and minimum displacement of the system gives  $Q$  of the resonant system. However it may be hard to determine the static displacement which is almost equal to displacements of very low frequencies. Sharper  $D$  plots indicate low damping and high  $Q$  system. For MEMS based mass sensors, high  $Q$  systems are desired since it is easier to measure resonance frequency shift due to mass addition in high  $Q$  systems. For the systems which  $\zeta > \sqrt{2}/2$ , resonant peak will not be observed. For  $r = 1$ , the phase lag is equal to  $\pi/2$ , regardless of the damping ratio.

Another definition of  $Q$  is based on the energies when the resonator is excited harmonically as stated in Equation (2-16).

$$Q = 2\pi \frac{U_{max}}{\Delta W} |_{r=1} \quad (2-16)$$

Where  $U_{max}$  is the maximum energy stored by the spring and  $\Delta W$  is the dissipated energy per cycle of steady state vibration.

$$U_{max} = \frac{1}{2} k x_{max}^2 = \frac{1}{2} k \left[ \frac{F_0}{k} D(r, \zeta) \right]^2 = \frac{F_0^2}{2k} \{D(r, \zeta)\}^2 \quad (2-17)$$

The energy dissipated in one cycle can be calculated as in Equation (2-18)

$$\begin{aligned}
\Delta W &= \int_0^{2\pi/\omega} F(t)x(t)dt \\
&= \int_0^{2\pi/\omega} F_0 \sin(\omega t) \left[ \frac{F_0}{k} D(r, \zeta) \omega \cos(\omega t - \theta) \right] dt \quad (2-18) \\
&= \frac{2\pi\zeta r F_0^2 [D(r, \zeta)]^2}{k}
\end{aligned}$$

Then Q can be calculated as in Equation (2-19):

$$Q \equiv \frac{1}{2\zeta r} \Big|_{r=1} = \frac{1}{2\zeta} = \frac{\sqrt{km}}{b} \quad (2-19)$$

Half power method [36] is another way of experimentally estimating Q of a resonance system. This method is known as -3 dB method. In this method, frequency response of the output of the resonator is measured (i.e. current or voltage). After determining the frequency response Equation (2-20) is applied.

$$Q \equiv \frac{\omega_{res}}{\Delta\omega} = \frac{f_{res}}{\Delta f} \quad (2-20)$$

$\omega_{res}$  is the resonant frequency and  $\Delta\omega$  is the frequency bandwidth where frequency response of the system is larger than  $D_{max}/\sqrt{2}$ .

There are different sources of damping in resonators. Contribution of these sources can be modeled separately and then Q of total system can be calculated.

$$Q = 2\pi \frac{U_{max}}{\Delta W_1 + \Delta W_2 + \Delta W_3 \dots + \Delta W_n} \Big|_{r=1} \quad (2-21)$$

$\Delta W_i$  ( $i=1,2,3,\dots,n$ ) represents power dissipation of different damping mechanisms

$$\frac{1}{Q} = \frac{1}{2\pi} \frac{\Delta W_1 + \Delta W_2 + \Delta W_3 \dots + \Delta W_n}{U_{max}} \Big|_{r=1} \quad (2-22)$$

or

$$Q = \frac{1}{\frac{1}{Q_1} + \frac{1}{Q_2} + \dots + \frac{1}{Q_n}} \quad (2-23)$$

If one of the damping mechanisms is dominated the others, modeling only the dominant mechanism may be enough and in this case  $Q$  can be estimated as in Equation (2-24).

$$Q \cong Q_{min} \quad (2-24)$$

## 2.2. Electrostatic Actuation and Sensing

Actuation is a very crucial phenomenon in MEMS. It is basically converting electrical energy into mechanical force. Electrostatic actuation is one of the most popular actuation methods used in a number of applications [37], [38], [39].

The main advantages of capacitive actuation and sensing can be listed as following [40]:

- Any conductive material can be employed as capacitive electrode. Therefore there are lots of alternatives for capacitive electrodes.
- Degrees of freedom of actuation and sensing can be arranged by using appropriate geometries of MEMS capacitors.
- MEMS capacitors are scalable and only limited with cost and fabrication capabilities.
- Capacitive systems do not draw DC current at steady state which enables low power integration.
- Electrostatic interactions may be used to arrange transducer gain and nonlinear effects may be used to tune resonant frequency with polarization voltage.
- Since an ideal capacitor has no internal noise, it is preferred in low noise sensing applications.

Despite of the advantages, it has some disadvantages. The main problem with electrostatic actuation and sensing is that electrostatic force efficiency is lower compared with electrothermal and piezoelectric transduction [40]. To generate higher forces, it is required higher polarization voltages and smaller transduction gaps which may increase damping and it is limited by fabrication constraints.

### 2.2.1. Electrostatic Actuation

Electrostatic actuation is defined as generation of electrostatic forces and making the movable mass of actuator move with the generated electrostatic force.

Force can be defined as the gradient of energy.

Energy of a capacitor can be shown in Figure 2-2 can be defined as in Equation (2-25).

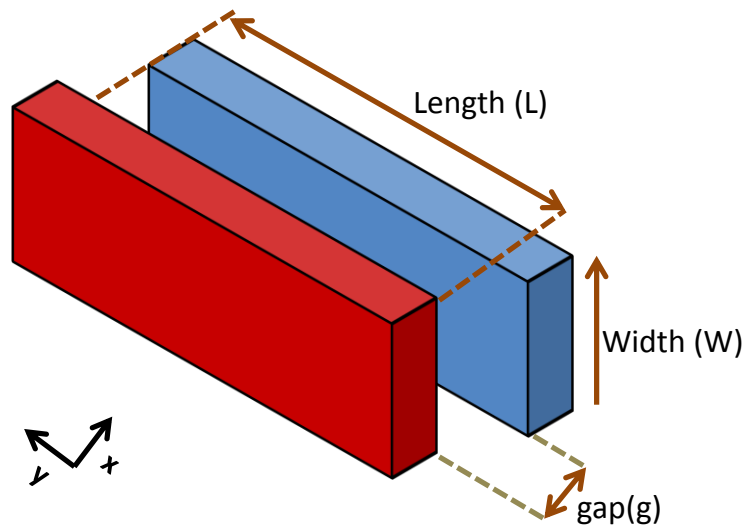


Figure 2-2: Illustration of a parallel plate capacitor with related variables

$$E = \frac{1}{2} C(x, y, z) V^2 \quad (2-25)$$

The capacitance of the parallel plate which is shown in Figure 2-2 can be calculated as in Equation (2-26).

$$C(x, y, z) = \varepsilon \frac{(L + y)(W + z)}{(g - x)} \quad (2-26)$$

Then the force can be calculated as in Equation (2-27).

$$\begin{aligned} F_{electrostatic} &= \nabla E \\ &= \frac{1}{2} \varepsilon V^2 \left( \frac{(L + y)(W + z)}{(g - x)^2} \vec{a}_x + \frac{(W + z)}{(g - x)} \vec{a}_y \right. \\ &\quad \left. + \frac{(L + y)}{(g - x)} \vec{a}_z \right) \end{aligned} \quad (2-27)$$

Voltage is generally summation of a DC and AC voltage

$$V = V_{dc} + v \cos(\omega t) \quad (2-28)$$

Then the force can be defined as in Equation (2-29).

$$\begin{aligned} F_{electrostatic} &= \nabla E \\ &= \frac{1}{2} \varepsilon \left( \frac{(L + y)(W + z)}{(g - x)^2} \vec{a}_x + \frac{(W + z)}{(g - x)} \vec{a}_y \right. \\ &\quad \left. + \frac{(L + y)}{(g - x)} \vec{a}_z \right) \left( \left( V_{dc}^2 + \frac{v^2}{2} \right) + 2V_{dc}v \cos(\omega t) \right. \\ &\quad \left. + \frac{1}{2} v \cos(2\omega t) \right) \end{aligned} \quad (2-29)$$

### 2.2.1.1. Varying Gap Actuation

In this type of actuation, capacitive area is constant (y and z displacements are zero). The only displacement is in x direction. The electrostatic force can be defined as Equation (2-30).

$$\begin{aligned}
F_{electrostatic} &= \nabla E \\
&= \frac{1}{2} \varepsilon \frac{LW}{(g - x(t))^2} \left( \left( V_{dc}^2 + \frac{v^2}{2} \right) + 2V_{dc}v\cos(\omega t) \right. \\
&\quad \left. + \frac{1}{2}v\cos(2\omega t) \right) - \frac{1}{2} \varepsilon \frac{LW}{(g + x(t))^2} V_{dc}^2
\end{aligned} \tag{2-30}$$

When we assume there are two symmetrical electrodes and AC signal is applied from one electrode and the other electrode is grounded we can write Equation (2-31). As understood, Equation (2-31) is nonlinear. When we assume that,  $V_{dc} \gg v$  we can ignore  $\cos(2\omega t)$  term at the output. Moreover due to the bandpass characteristics of resonator, effect of  $\cos(2\omega t)$  can be ignored.

$$\begin{aligned}
mx''(t) + bx'(t) + kx(t) \\
&= \frac{1}{2} \varepsilon \frac{LW}{(g - x(t))^2} \left( V_{dc}^2 + 2V_{dc}v\cos(\omega t) \right) \\
&\quad - \frac{1}{2} \varepsilon \frac{LW}{(g + x(t))^2} V_{dc}^2
\end{aligned} \tag{2-31}$$

Let's apply Taylor's series expansion to  $1/(g - x)^2$  and  $1/(g + x)^2$  terms:

$$\frac{1}{(g - x)^2} \cong \frac{1}{g^2} + \frac{2x}{g^3} + O(x) \tag{2-32}$$

$$\frac{1}{(g + x)^2} \cong \frac{1}{g^2} - \frac{2x}{g^3} + P(x) \tag{2-33}$$

It may be assumed that the movement is so small compared to the gap and we can ignore  $O(x)$  and  $P(x)$ . Then the equation of motion turns out Equation (2-34):

$$m\ddot{x}(t) + b\dot{x}(t) + kx(t) = \frac{2\varepsilon LWx(t)}{g^3} V_{dc}^2 + \frac{\varepsilon LW}{g^2} V_{dc} v \cos(\omega t) \quad (2-34)$$

When we rearrange the terms of Equation (2-34) as in Equation (2-35):

$$m\ddot{x}(t) + b\dot{x}(t) + \left(k - \frac{2\varepsilon LW}{g^3} V_{dc}^2\right)x(t) = \frac{\varepsilon LW}{g^2} V_{dc} v \cos(\omega t) \quad (2-35)$$

As seen from Equation (2-35), it can be easily observed that spring constant decreases with increasing DC polarization voltage. This phenomenon is called as spring softening and using this phenomenon resonance frequency of resonators can be easily tuned [41].

After a certain voltage value, spring constant will become negative which causes instability. Normally spring force is a restoring force which pulls the movable mass to its resting state. However negative spring constant means the spring will continue to apply force in the movement direction. Therefore very small disturbance from the equilibrium point causes movable mass stick one of the electrodes and short circuit. This phenomenon is called as pull-in and pull-in voltage can be calculated equating spring constant to zero as shown in Equation (2-36).

$$k - \frac{2\varepsilon LW}{g^3} V_{pull-in}^2 = 0, V_{pull-in} = \sqrt{\frac{kg^3}{2\varepsilon LW}} \quad (2-36)$$

For DC polarization voltages higher than  $V_{pull-in}$ , even small ac voltages disturbing the equilibrium causes movable mass to stick electrodes and causes short circuit. Therefore for proper operation resonators, proof masses of resonators should be polarized with voltages lower than  $V_{pull-in}$ .

### 2.2.1.2. Varying Overlap Area Actuation

In this type of actuation, overlap area can change due to the motion of movable body while the gaps between electrodes are constant. For the parallel plate

capacitor shown in Figure 2-2, we are assuming that the movement is only in  $y$  direction. Moreover we are assuming the body is perfectly symmetric and  $V_{dc} \gg v$ .

$$F_{electrostatic} = \frac{1}{2} \varepsilon \frac{W}{g} \left( (V_{dc}^2 + (2V_{dc}v \cos(\omega t))) - V_{dc}^2 \right) \quad (2-37)$$

$$m\ddot{x}(t) + b\dot{x}(t) + kx(t) = \varepsilon \frac{W}{g} V_{dc} v \cos(\omega t) \quad (2-38)$$

As seen from Equation (2-38), electrostatic force is linear under our assumptions. Moreover this type of actuation ideally does not suffer from pull-in instability and DC polarization voltage can be increased as much as possible. However, although this actuation type serves more linear operation, the force applied is smaller.

### 2.2.2. Electrostatic Sensing

Sensing may be defined as conversion of movement to electrical current for capacitive transducers. The most general definition of output current is defined as change rate of charge.

$$i = \frac{dQ}{dt} \quad (2-39)$$

For a capacitor total charge and current can be calculated as in Equations (2-40) and (2-41).

$$Q = CV \quad (2-40)$$

$$i = \frac{dQ}{dt} = C \frac{dV}{dt} + V \frac{dC}{dt} \quad (2-41)$$

$V \frac{dC}{dt}$  term gives the information related with motion and it is much larger than the  $C \frac{dV}{dt}$  term. Therefore we can rearrange Equation (2-41) as in Equation (2-42):

$$i = V \frac{dC}{dt} = V \frac{dC}{dx} \frac{dx}{dt} \quad (2-42)$$

For a variable gap actuator the derivative of capacitor to the motion can be calculated as shown in Equation (2-43).

$$\frac{dC}{dx} = \frac{LW}{(g - x(t))^2} \quad (2-43)$$

For infinitesimal movement we can ignore the motion.

$$\frac{dC}{dx} = \varepsilon \frac{LW}{g^2} \quad (2-44)$$

$$V = V_{dc} \quad (2-45)$$

$$i = V_{dc} \varepsilon \frac{LW}{g^2} \frac{dx}{dt} \quad (2-46)$$

For a resonance system the transconductance of the system can be calculated considering Equations (2-35 and (2-46 together.

Taking Laplace transform of Equations (2-35 and (2-46, Equation (2-47) can be reached. As a result overall transfer function of transconductance of resonator system for a varying gap actuator can be calculated as Equation (2-49).

$$(ms^2 + bs + (k - \frac{2\varepsilon LW}{g^3} V_{dc}^2))X(s) = \varepsilon \frac{LW}{g^2} V_{dc} V(s) \quad (2-47)$$

$$I(s) = V_{dc} \varepsilon \frac{LW}{g^2} sX(s) \quad (2-48)$$

$$\frac{I(s)}{V(s)} = \frac{s \left[ \varepsilon \frac{LW}{g^2} V_{dc} \right]^2}{ms^2 + bs + (k - \frac{2\varepsilon LW}{g^3} V_{dc}^2)} \quad (2-49)$$

It is possible to calculate output current for a varying overlap area actuator under similar assumptions for varying gap actuator.

$$\frac{dC}{dx} = \varepsilon \frac{W}{g} \quad (2-50)$$

As seen from Equations (2-49 and (2-52, under certain assumptions current sensing is a linear operation.

However, for varying gap actuators, we can observe some harmonics even we assume that the motion is completely linear.

$$i = V_{dc} \varepsilon \frac{W}{g} \frac{dx}{dt} \quad (2-51)$$

$$\frac{I(s)}{V(s)} = \frac{s \left[ \varepsilon \frac{W}{g} V_{dc} \right]^2}{ms^2 + bs + k} \quad (2-52)$$

We can assume the motion is completely linear for the sake of simplicity.

$$x(t) = x_0 \cos(\omega t) \quad (2-53)$$

$$i = V_{dc} \varepsilon \frac{LW}{(g - x(t))^2} x_0 \omega \sin(\omega t) \quad (2-54)$$

From Taylor series expansion we can reach to Equation (2-55).

$$i \cong \frac{V_{dc} \varepsilon LW x_0 \omega \sin(\omega t)}{g^2} + \frac{V_{dc} \varepsilon LW x_0^2 \omega \sin(2\omega t)}{2g^3} \quad (2-55)$$

As seen from Equation (2-55 even if the movement is completely linear, we can see considerable amount of 2<sup>nd</sup> harmonic current at the output.

### 2.3. Damping Mechanisms Effective on Resonators Operating in Viscous Medium

Quality factor is very crucial in mass sensors and it is directly related with mass sensitivity of mass sensor. To be able to estimate quality factor of resonator correctly, damping coefficient should be modeled.

As stated in Equation (2-23, for multiple damping mechanisms the dominant damping mechanism determines quality factor of the resonator. For the resonators operating under viscous medium, the dominant damping mechanism is damping caused by fluid. In this part, air and liquid damping of resonators will be discussed in detail.

For a resonator operating in viscous medium, there are basically three fluidic damping mechanisms: slide film damping, squeeze film damping and drag forces [42].

Structures suspended over a substrate may suffer from slide film damping. In Figure 2-3, slide film damping mechanism is summarized. In slide film damping moving plate moves parallel to the substrate and ambient fluid causes energy loss of moving plate.

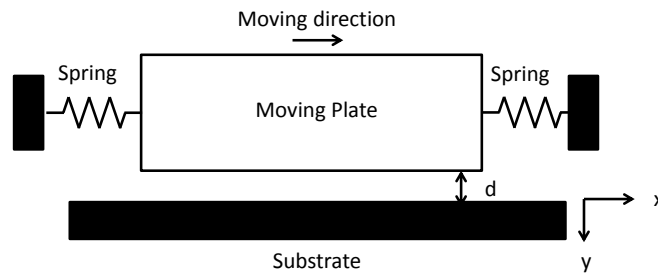


Figure 2-3: Slide film damping schematic structure

After certain distance from moving plate, liquid molecules do not cause energy dissipation significantly. This distance is named as effective decay displacement ( $\delta$ ). Effective decay displacement can be calculated as in Equation (2-56 [42].

$$\delta = \sqrt{\frac{2\mu}{\rho\omega}} \quad (2-56)$$

$\mu$  is viscosity of the fluid,  $\rho$  is the density of fluid and  $\omega$  is the frequency of movement.

If the substrate distance ( $d$ ) is much smaller than the effective decay displacement ( $\delta$ ), damping force can be calculated as in Equation (2-57) [42].

$$F = -\mu \frac{A}{d} u(t) \quad (2-57)$$

$A$  is the contact area and  $u(t)$  is the velocity of the moving plate.

If the substrate distance ( $d$ ) is much larger than the effective decay displacement ( $\delta$ ), damping force can be calculated as in Equation (2-58) [42].

$$F = -\mu \frac{A}{\delta} u(t) \quad (2-58)$$

Another important damping mechanism effective on micro-resonators is the drag force. Drag force will be applied on a body when a body is held steady in a fluid flow or a body is dragged through a steady fluid [42]. For a circular plate with radius  $r$  moving its normal direction, the drag force can be calculated as in Equation (2-59) [42].

$$F = -\frac{32}{3} \mu r u(t) \quad (2-59)$$

Another important damping mechanism is squeeze film damping force. In Figure 2-4, the mechanism of squeeze film damping is given.

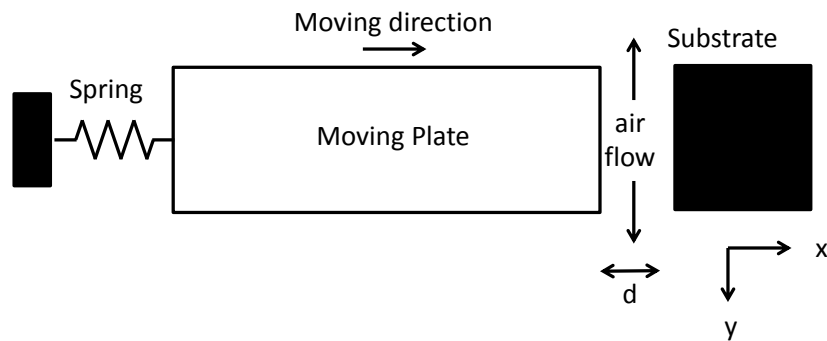


Figure 2-4: The mechanism of squeeze film damping

When the plate moves to substrate, the air between the plate and substrate squeezes and air flows out of the gap and an additional pressure is generated in the gap due to the flow of the air. On the other hand, when the plate moves away from the substrate, air flows inside the gap and the pressure in the gap decreases. In both cases, air flow causes a force against the movement. For a rectangular plate moving in z direction given in Figure 2-5, the damping force can be calculated as in Equation (2-60 [42]).

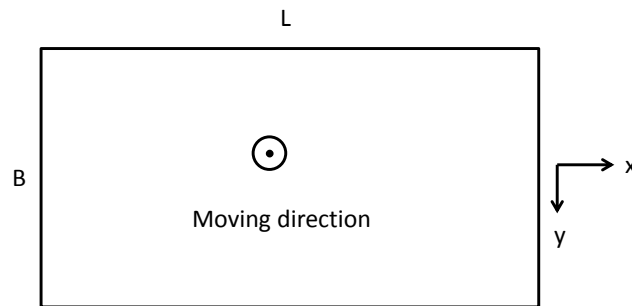


Figure 2-5: The rectangular plate which is exposed to squeeze film damping

$$F = \frac{\mu L B^3}{d^3} \beta \left( \frac{B}{L} \right) \quad (2-60)$$

$d$  is the distance between the plate and substrate and  $\beta(B/L)$  is the squeeze number which depends on  $\frac{B}{L}$ . For  $L \gg B$ ,  $\beta \cong 1$ . Variation of  $\beta$  with respect to  $B/L$  is given in Figure 2-6 [42].

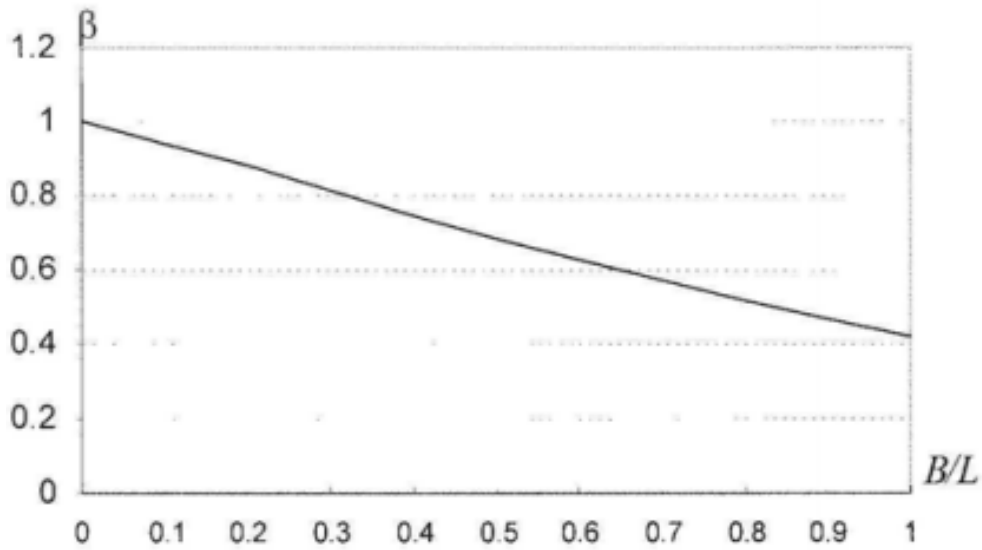


Figure 2-6: Variation of  $\beta$  with respect to  $B/L$  [42]

## 2.4. Conclusion

In this chapter background theory to be able to design a resonator is presented. Firstly, resonators may be modeled as a spring-mass-damping system and damping ratio plays a crucial role on the performance of resonators. Quality factor is determined by the damping coefficient and it is directly related with the sensing performance of resonance based sensors. The other important subject is actuation and sensing of resonators. There are many ways to actuate and sense a micro-resonator. Electrostatic actuation and sensing is a useful method due to its several advantages presented. Electrical signal can be easily converted into force and the generated force moves the resonator. Resonator movement causes capacitance change and this capacitance change can be sensed as current at the output of the resonators. As a result of electrostatic actuation/sensing, some nonlinearities occur. The first result of these nonlinearities is spring softening phenomena. Resonance frequency changes with DC polarization voltage. The other result is generation of higher order harmonic terms at the output current. As stated before, damping is very crucial in the performance of resonators. The last subject

presented in this chapter is damping mechanisms effective on resonators operating in viscous media. These mechanisms are basically slide film damping, squeeze film damping and drag forces. These forces depend on the dimensions of resonators. Therefore resonator dimensions are needed to be chosen carefully to design a resonator operating properly in air environment. In the next chapter resonator design procedures and effect of resonator dimensions on  $Q$  and transconductance of resonators will be presented.

## CHAPTER 3

### DESIGN OF RESONATORS

In this chapter, design considerations of resonators will be explained in detail and effect of resonators on  $Q$  and output current of one of the devices will be calculated. Furthermore, the designed devices will be shown. In [35] some resonator types are proposed. Their operations are verified. It is also shown the fundamental vibration modes of the resonators are lateral mode. However, their quality factors, output currents are not optimized. First of all design parameters and considerations will be explained and then designed resonators with simulation results will be given.

#### 3.1. Design Parameters

In a resonator, there are basically three design parameters: mass, spring constant and damping. These parameters determine the frequency response of the resonator.

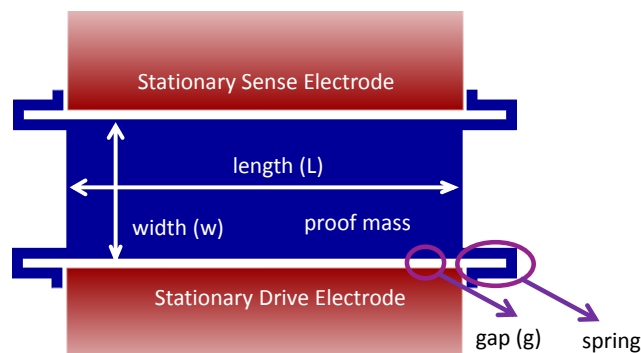


*Figure 3-1: Conceptual schematic of a lateral mode electrostatic resonator*

Therefore a resonator designer should tune these factors for proper operation of resonators. In Figure 3-1, the conceptual schematic of a lateral mode electrostatic resonator is given. The theoretical work and optimization for the remaining of this chapter is conducted using this conceptual resonator.

### 3.1.1. Spring Constant

Spring structures are utilized for anchoring the resonating mass to solid body. Moreover spring constant determines quality factor, displacement of resonator and output current of the resonator. In the literature there are lots of different spring topologies. For lateral motion, folded beam springs shown in Figure 3-2 are preferred since they are linear during deflection, provides high spring constants without losing linearity and prevent torsional modes [43]. There are four springs in the designed resonators to achieve symmetry and prevent torsional modes.

The lateral mode spring constant for the spring in Figure 3-2 can be calculated as in Equation (3-1).

$$k = E \frac{1}{2} \frac{t * w_s^3}{l_s^3} \quad (3-1)$$

E is the Young's modulus of the silicon, t is the thickness of the resonator.

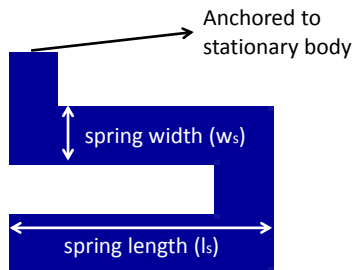


Figure 3-2: The schematic of a folded beam

Since there are four springs Equation 3-1 should be multiplied by four. Considering the effect of spring softening we reach the Equation (3-2) as the spring constant for the resonator shown in Figure 3-1.

$$k_{eff} = \frac{2Et w_s^3}{l_s^3} - \frac{2\epsilon t L V_{dc}^2}{g^3} \quad (3-2)$$

L is the length of the device and g is the actuation gap.

Spring is designed the same for all devices to prevent possible fabrication mismatches. The width of the spring is chosen as 10 μm and length is chosen as 60 μm. Device thickness is determined as 10 μm. As a result the spring constant is calculated as 12037 N/m.

### 3.1.2. Mass

Mass is the total mass of the resonator. It can be calculated summing of mass of all device layers on the proof mass. Moreover springs are also effective on the mass of resonator. Total mass load of springs on the resonator mass is calculated multiplying spring mass with 0.37 [44].

Total mass can be calculated as in Equation (3-3).

$$mass = mass\ of\ proof\ mass + 0.37 * (total\ spring\ mass) \quad (3-3)$$

Increasing mass causes decrease of mass sensitivity. Therefore total mass of resonator should be minimized as much as possible.

### 3.1.3. Damping

Damping is another design parameter of resonators. Unfortunately it is not easy to tune damping factor as mass or spring constant. There are lots of damping factors effective on micro-resonators like anchor loss, body loss, thermo-elastic damping, electrical damping. However for the resonators operating in the liquid environment the dominant damping mechanism is the damping caused by liquid. In Figure 3-3, liquid damping mechanisms for a resonator embedded on the wall of a microchannel is shown [34].

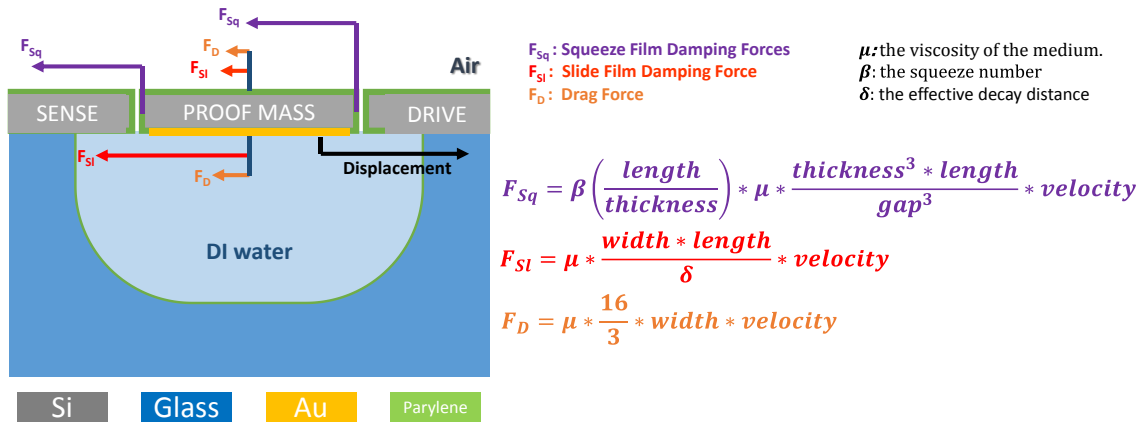


Figure 3-3: Illustration of damping in resonator-on-microchannel. There are basically three damping factors. When operated in the air, the dominant damping mechanism is squeeze film damping. However since viscosity of water is much higher than air, the dominant damping mechanism becomes slide film damping caused by DI water.

To control damping, actuation gaps, width of resonator, thickness of resonator and surface area of resonator should be well arranged. Otherwise, unpredictable damping coefficients may be obtained.

### 3.2. Design Considerations

#### 3.2.1. Quality Factor (Q)

Quality factor (Q) is a unitless expression of how underdamped a resonator is. It is defined as the ratio of stored energy to dissipated energy per cycle of steady state vibration at the resonance frequency. It can be calculated dividing the resonance frequency to -3 dB bandwidth of the resonator experimentally. Theoretical and mathematical calculation of Quality factor is mentioned in Section 21.

Higher Q systems mean sharper frequency response. It is one of the most important design considerations and directly related with minimum detectable mass. Low Q resonators have wider bandwidth and change of resonance

frequency may not be tracked easily in low Q resonators. Therefore, small mass changes may not be easily sensed using low Q resonators.

Minimum detectable mass of mass sensors can be calculated as in Equation (3-4) [43].

$$\begin{aligned}
 (\Delta m)_{min} &= \frac{4m_{resonator}}{x_{max}} \sqrt{\frac{K_b T w_m}{k Q w_0}} = \frac{4}{Q^{3/2}} * \frac{\sqrt{K_b T w_m m \sqrt{k}}}{F_{electrostatic}} \\
 &= \frac{4g^2}{Q^{3/2}} * \frac{\sqrt{K_b T w_m m \sqrt{k}}}{\epsilon L t V_{DC} \nu}
 \end{aligned} \tag{3-4}$$

$K_b$  is Boltzmann constant,  $T$  is temperature and  $w_m$  is the measurement bandwidth.

As seen from Equation (3-4) minimum detectable mass decreases with higher Q resonators. Therefore high Q resonators are better mass sensors. Quality factor depends on lots of parameters resonators operating in viscous medium. Thickness, actuation gap, surface area, spring dimensions are a few of them. To achieve maximum Q, these parameters should be tuned carefully. In Figure 3-4 and Figure 3-5 effect of thickness on Q (all other parameters are constant) of RBS in air and liquid is shown respectively. As seen from the figures, Q is initially very low and increasing with thickness since spring constant and mass increases faster than the damping. After the maximum value of Q, Q starts to decrease since squeeze film damping starts to become dominant and increases significantly. Moreover it is obviously seen that, optimum Q values in the air and liquid is different from each other. The optimum thickness depends on the other parameters of the resonator, especially length and actuation gap since they are the most effective parameters on squeeze damping. For this specific resonator optimum Q value in liquid is reached at 12  $\mu\text{m}$  thickness.

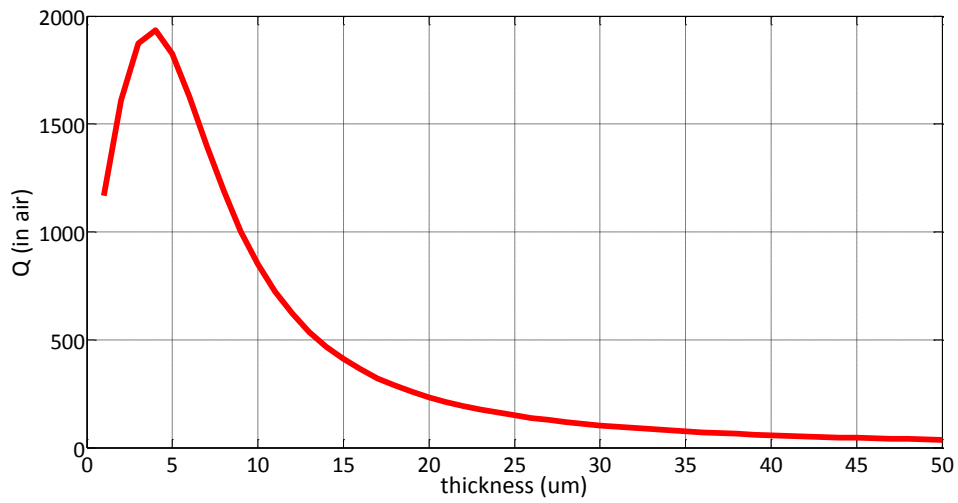


Figure 3-4: Effect of thickness to  $Q$  in air environment

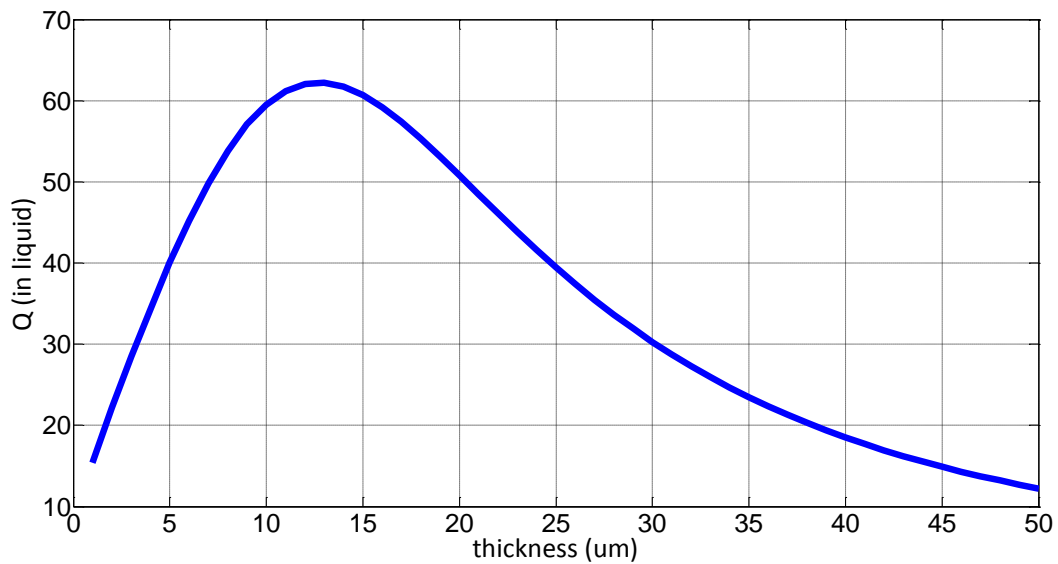
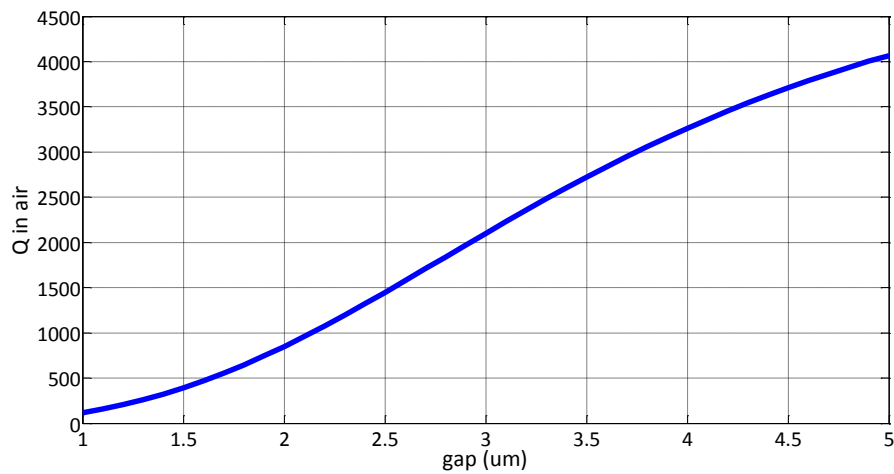


Figure 3-5: Effect of thickness to  $Q$  under liquid flow

Increasing actuation gap increases Quality factor significantly, but decreases output current. Therefore it should be tuned carefully. Moreover for operation under liquid flow, leakage from actuation gaps should be prevented. Hydrophobicity of parylene is limited. Therefore actuation gap cannot be

increased significantly. In Figure 3-6 and Figure 3-7 effect of gap on  $Q$  is illustrated. As seen from Figure 3-6  $Q$  in air environment increases monotonically with increasing gap but  $Q$  under liquid flow starts to remain almost constant after certain value of the gap since slide film damping is dominant under liquid flow. Moreover increasing gap decreases will decrease the capacitive area hence the output current and parylene hydrophobicity may not prevent liquid leakage. Therefore, we kept the actuation gap as  $2\ \mu\text{m}$ .



*Figure 3-6: Effect of gap on  $Q$  in air environment*

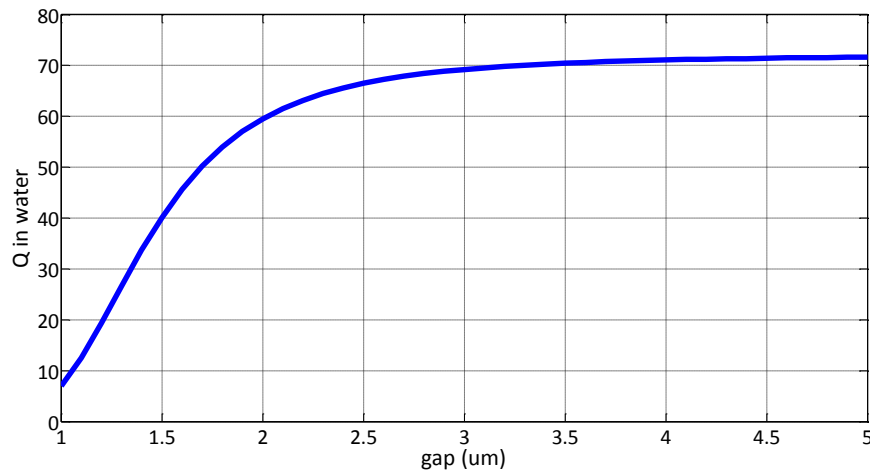


*Figure 3-7: Effect of gap on  $Q$  under liquid flow*

In Figure 3-8 and Figure 3-9 effect of length on  $Q$  in air and liquid environment is shown respectively. Increasing length will decrease  $Q$  after a certain value of length in both air and liquid environment since it increases both slide film damping and squeeze film damping. However increasing length will increase output current. Therefore it cannot be kept so small.

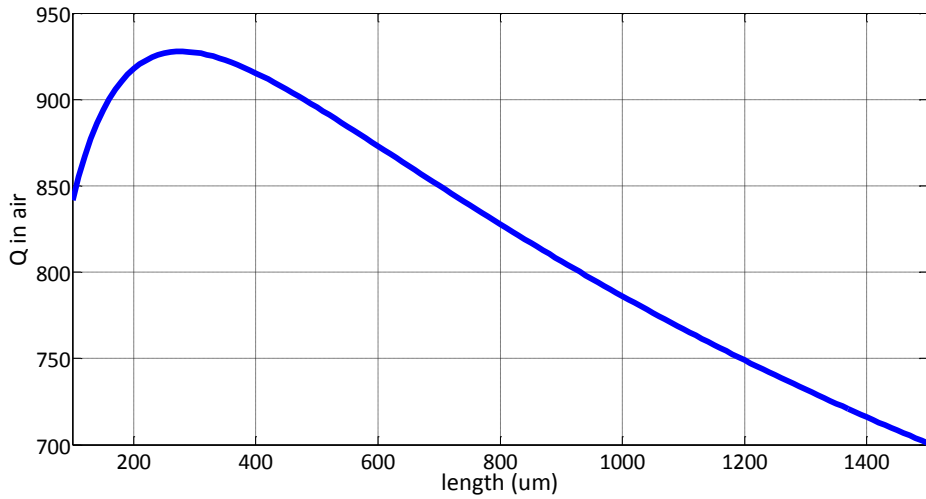


Figure 3-8: Effect of resonator length on  $Q$  in air environment

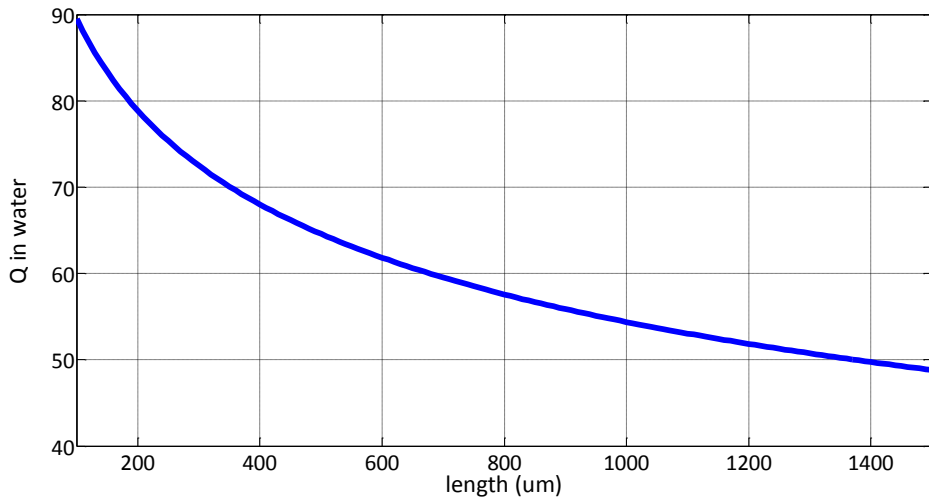
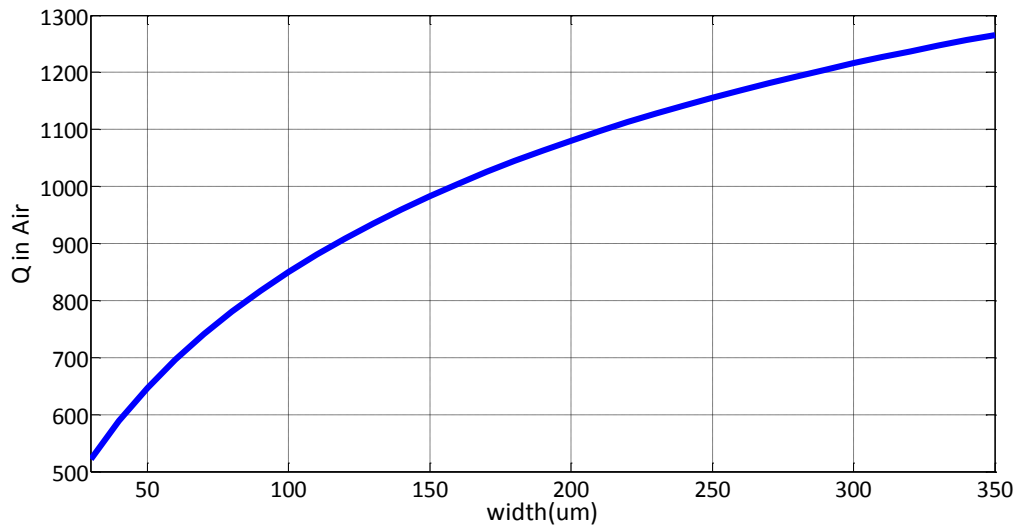
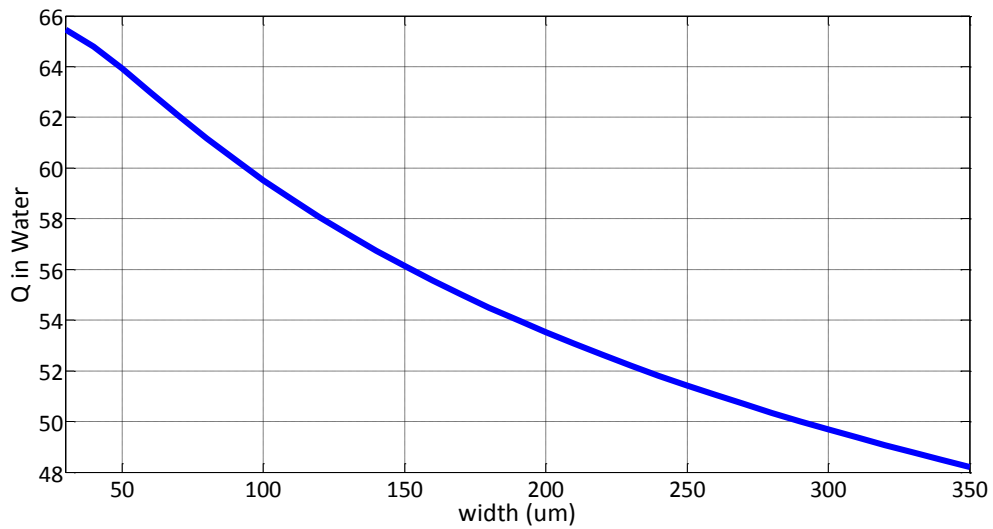


Figure 3-9: Effect of resonator length on  $Q$  in liquid environment



*Figure 3-10: Effect of resonator width on Q in air*



*Figure 3-11: Effect of resonator width on Q in liquid environment*

Increasing width will increase Q in air environment as shown in Figure 3-10 since increasing width will increase mass and decrease the effect of squeeze film damping. However it will decrease the Q in liquid environment since as seen from Figure 3-11 since slide film damping is the dominant factor under liquid flow and

slide film damping will increase with increasing width. To increase Q in liquid decreasing width is a feasible solution but decreasing width too much will cause corruption in mode shape.

### 3.2.2. Output Current

Output current is another important design parameter. Although it is not found in the minimum detectable mass formula, it plays very crucial role in detection of resonance frequency since if the output current of the resonator is high enough, effect of feedthrough current decreases significantly since resonator current dominates feedthrough current. The other important issue is about read-out circuitry. If the output current of resonator is low, it cannot be measured due to the noise of the read-out circuitry. Therefore output current of resonator should be high as much as possible.

Output current can be easily calculated finding the maximum value of the transfer function given in Equation 3-5.

$$\frac{I(s)}{V(s)} = \frac{s \left[ \varepsilon \frac{LW}{g^2} V_{dc} \right]^2}{ms^2 + bs + \left( k - \frac{2\varepsilon LW}{g^3} V_{dc}^2 \right)} \quad 3-5$$

Thickness of the resonator is one of the most effective factors on the output current. Increasing thickness increases capacitive area but also increases squeeze film damping. Therefore there is an optimum thickness which will maximize the output current. In Figure 3-12 and Figure 3-13, the graph showing variation of current with changing thickness in air and liquid is given respectively for RBS. Optimum thickness of this resonator for maximum current in liquid environment is 20  $\mu\text{m}$  but considering Q we kept our thickness as 10  $\mu\text{m}$ .

Similarly actuation gap is an important factor effective on output current. Increasing actuation gap increases electrostatic force and capacitive area. However it also increases the squeeze film damping significantly. Therefore it has

an optimum value for maximizing the output current. The optimum point may vary under liquid flow or operating in air. In Figure 3-14 and Figure 3-15 , the graph showing variation of current with changing actuation gap is given for the resonator shown in Figure 3-1.

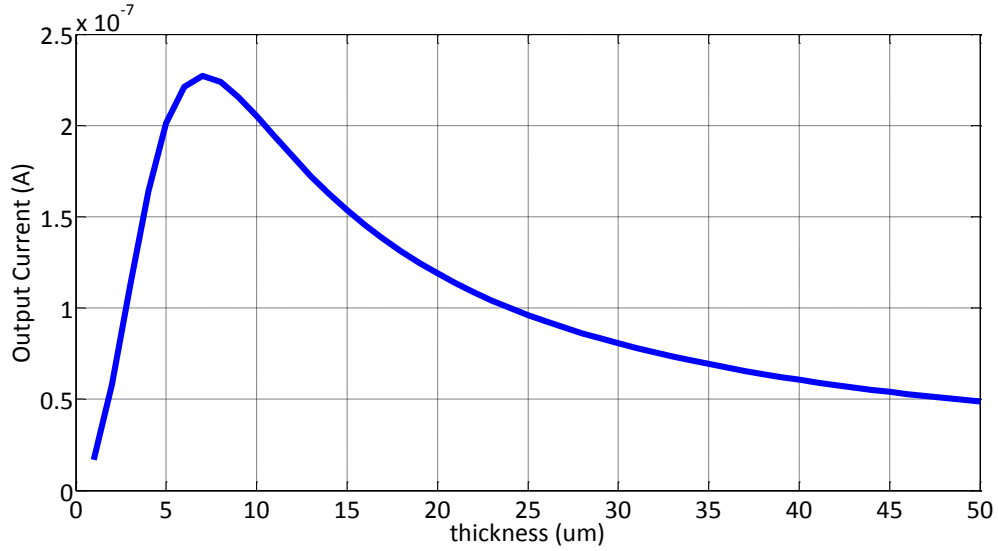


Figure 3-12: Effect of thickness on output current in air

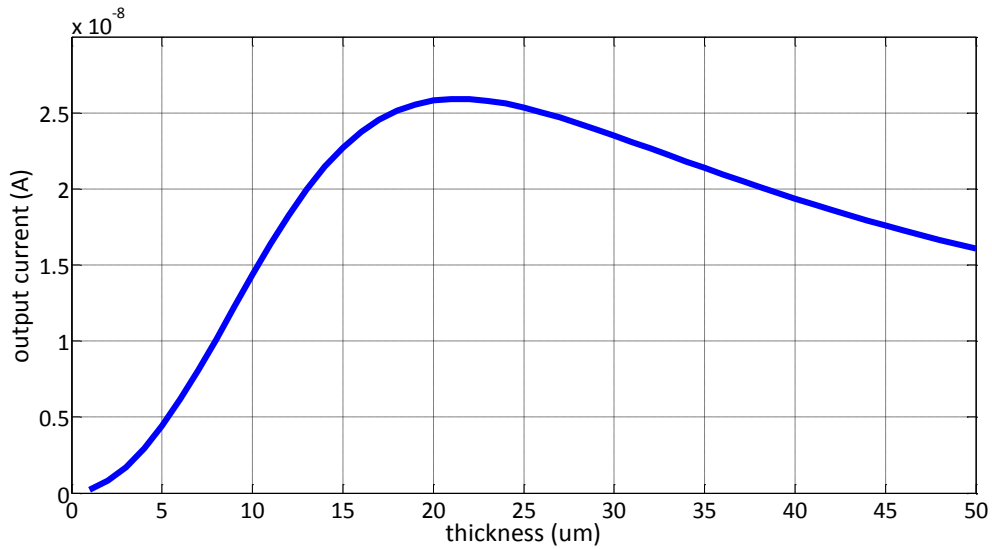


Figure 3-13: Effect of thickness on the output current in liquid environment

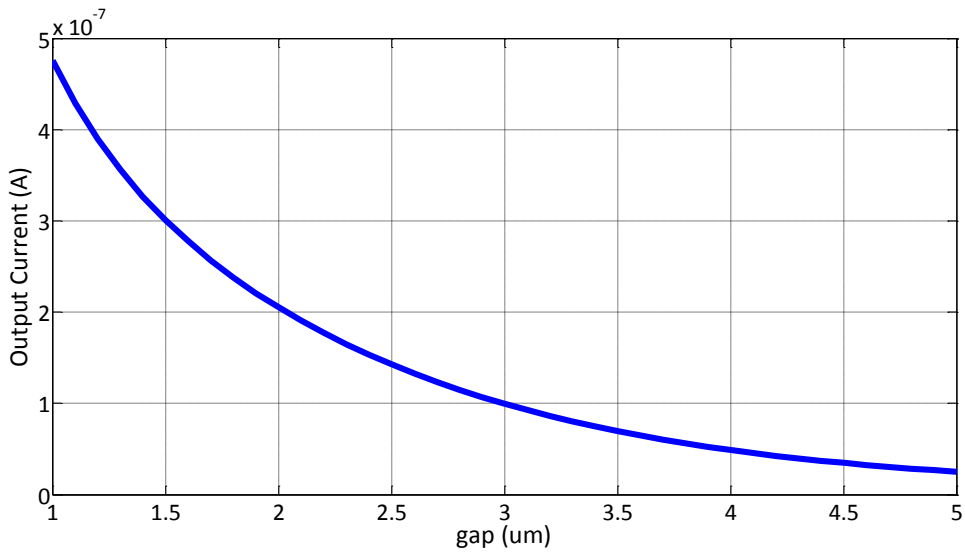


Figure 3-14: Effect of actuation gap on the output current in air

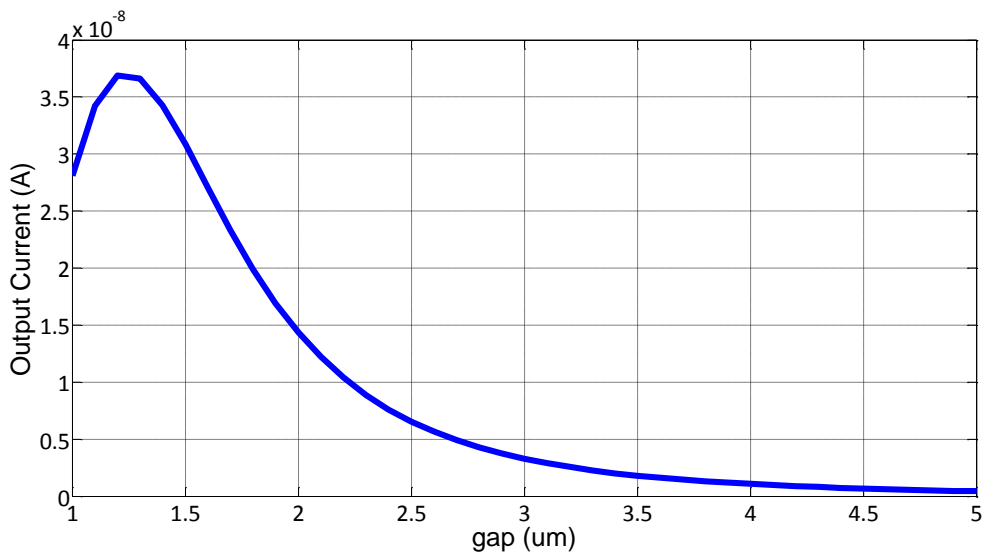


Figure 3-15: Effect of actuation gap on the output current in liquid environment

Length of resonators also affects the output current. Increasing length similarly will increase the capacitive area Q will start to decrease due to increasing slide film and squeeze film damping. In Figure 3-16 and Figure 3-17 the graph showing

the variation of output current with length is given for the resonator shown in Figure 3-1.

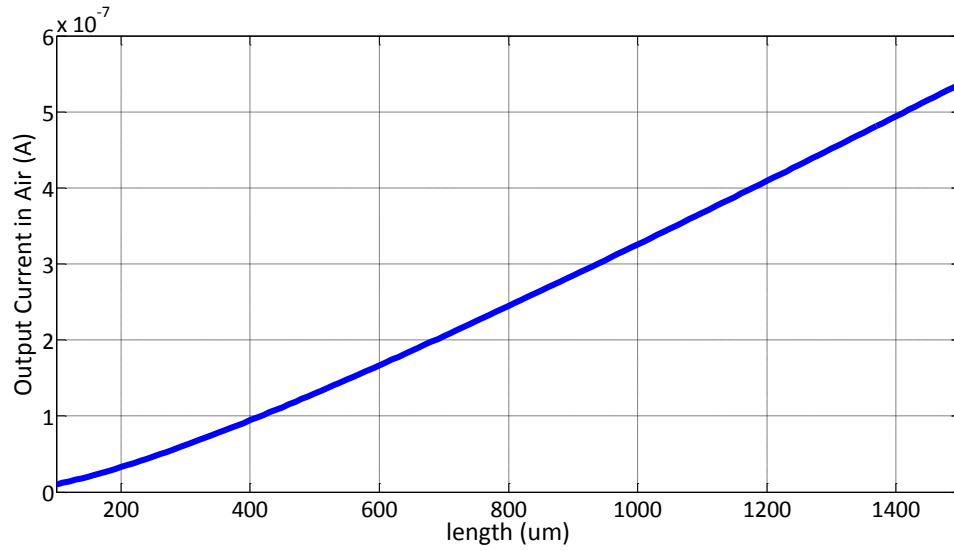


Figure 3-16: Effect of resonator length on resonator current in air

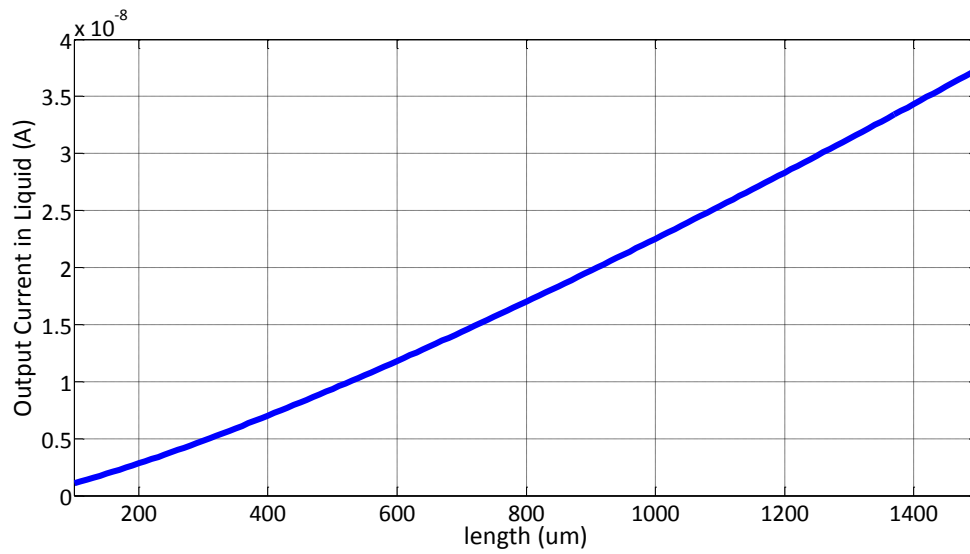


Figure 3-17: Effect of resonator length on resonator current in liquid environment

Resonator width is another parameter that is affecting resonator current. Having low resonator width will increase the output current since effect of damping will decrease. However to protect mode shape width should not be decreased too much.

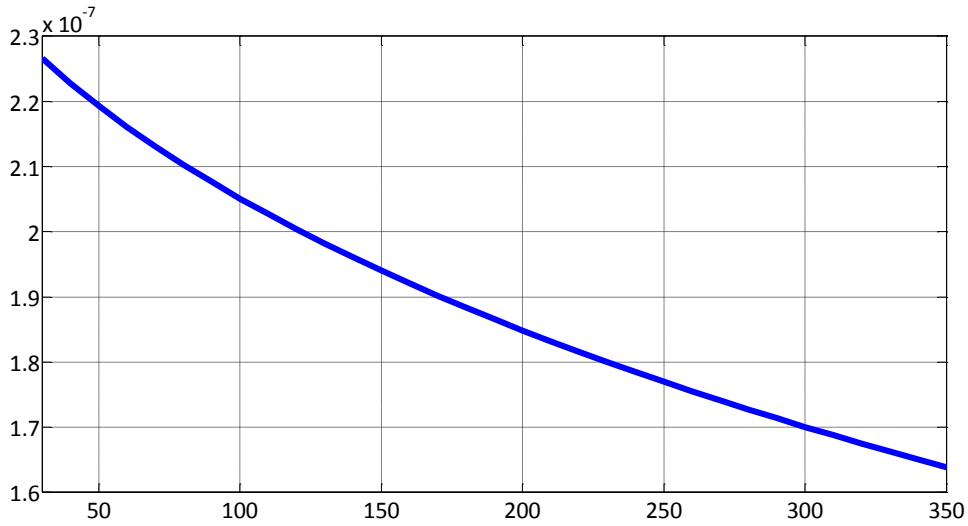


Figure 3-18: Effect of resonator width on the current in air

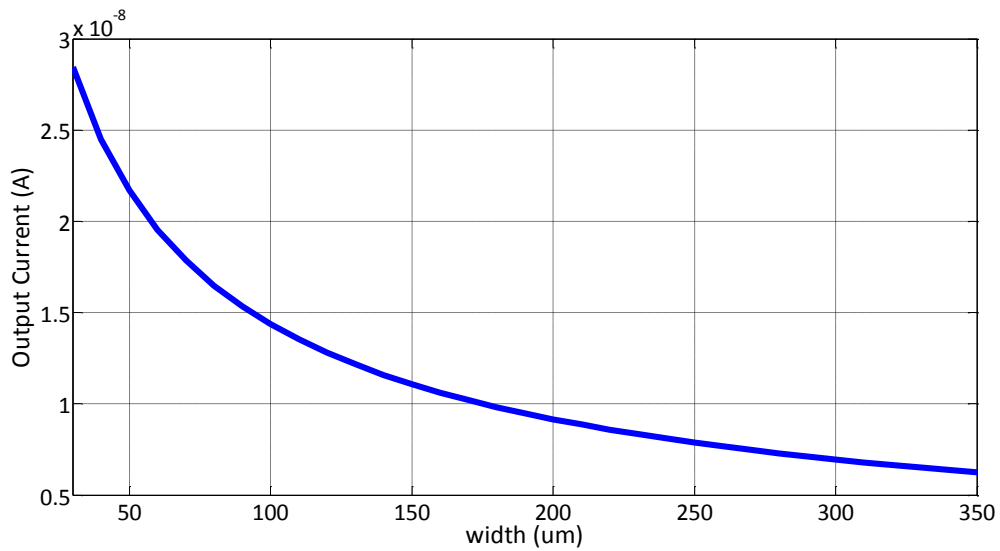


Figure 3-19: Effect of resonator width on the current in liquid environment

The other parameter affecting the output current is DC polarization voltage. Increasing DC polarization voltage will increase output current but the DC polarization voltage should be lower than the pull in voltage for stable operation of the resonators. Moreover, applying too high DC polarization voltages may cause sparks which harm resonators. Moreover for the resonator with fingers number of fingers is also critical for output current. Fingers are also increase the squeeze film damping and so optimum number of fingers should be determined properly.

### 3.3. Resonator Design

#### 3.3.1. Resonator with Basic Structure (RBS)

This resonator type is the most basic resonator. Most theoretical work is conducted on this resonator. The length of this resonator type is designed as 700  $\mu\text{m}$  and width is designed as 100  $\mu\text{m}$ . Actuation gaps are kept as 2  $\mu\text{m}$ . In Figure 3-20 the schematic of RBS with related dimensions is given

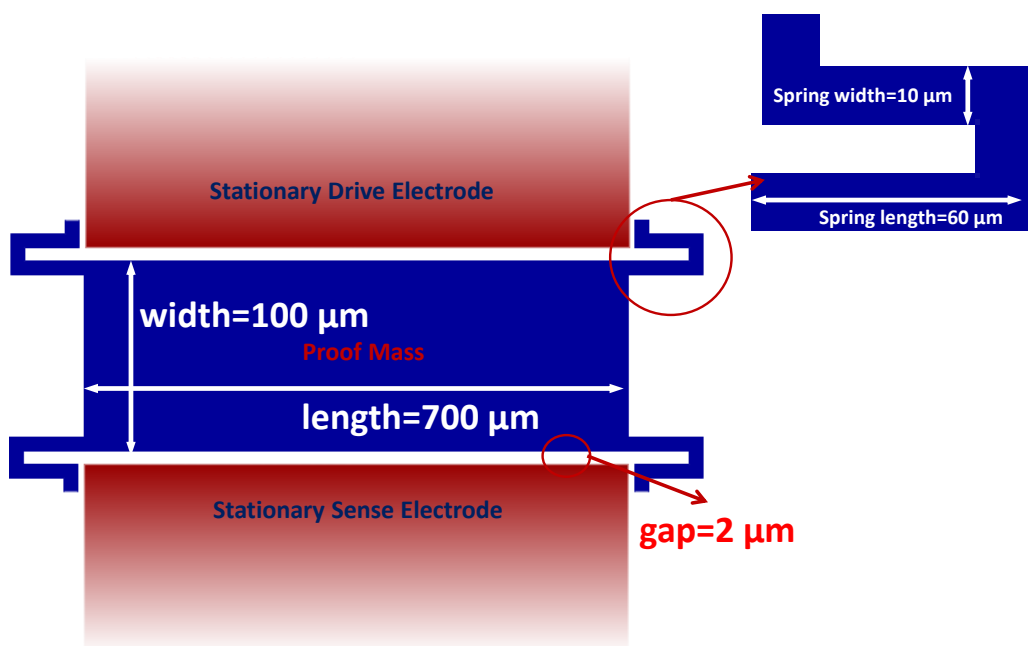


Figure 3-20: Mask drawing of RBS

The transfer function of the designed resonator is given in air and in liquid is given in Equations (3-6) and (3-7) respectively. In Figure 3-21, frequency response of the resonator is shown. The resonator without parylene coating has a Q factor 850. Q after liquid injection is calculated as 60. When the transconductance of resonators are analyzed, the transconductance in air and liquid is calculated as 250 nA/V and 14 nA/V respectively.

$$\frac{I(s)}{V(s)} = \frac{1.2 * 10^{-12} s}{2.08 * 10^{-9} s^2 + 5.85 * 10^{-6} s + 1.204 * 10^4} \quad (3-6)$$

$$\frac{I(s)}{V(s)} = \frac{1.2 * 10^{-12} s}{2.08 * 10^{-9} s^2 + 8.36 * 10^{-5} s + 1.204 * 10^4} \quad (3-7)$$

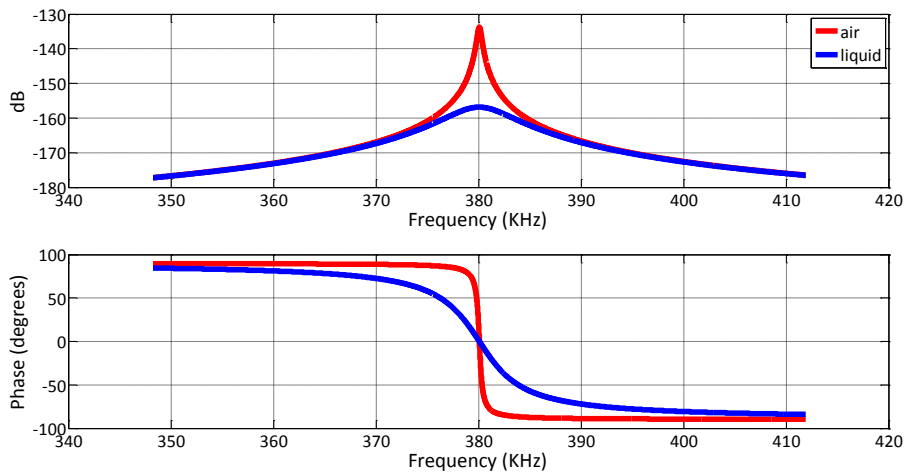


Figure 3-21: Calculated frequency response of RBS in air (red) and liquid environment (blue)

### 3.3.2. Resonator with Tree Finger Structure (RTFS)

This resonator is proposed to maximize output current to get rid of the effect of feedthrough current in [35]. However this resonator suffers from low Q. To increase Q, first of all fingers attached to the side of the resonator is removed to

decrease squeeze film damping. Therefore number of branches and number of tree structures were optimized for this resonator. Length of resonator is determined considering length and number of fingers and width was optimized to maximize the quality factor. In Figure 3-22 the schematic of RTFS is shown.

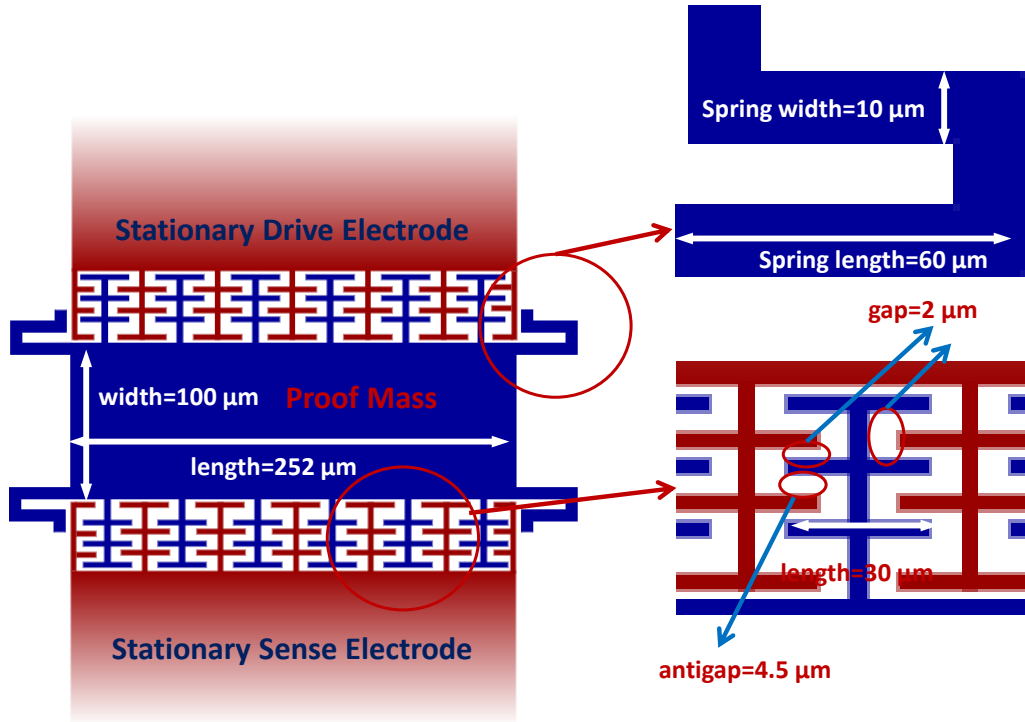


Figure 3-22: Mask drawing of RTFS with related design parameters

The transfer function of the designed resonator is given in air and in liquid is given in Equations (3-8 and (3-9 respectively. In Figure 3-23, frequency response of the resonator is shown.

$$\frac{I(s)}{V(s)} = \frac{3.43 * 10^{-13}s}{7.85 * 10^{-10}s^2 + 1.06 * 10^{-5}s + 1.204 * 10^4} \quad (3-8)$$

$$\frac{I(s)}{V(s)} = \frac{3.43 * 10^{-13}s}{7.85 * 10^{-10}s^2 + 6.61 * 10^{-5}s + 1.204 * 10^4} \quad (3-9)$$

The resonator in air has a Q factor 291 and Q after liquid injection is calculated as 44. When the transconductance of resonators are analyzed, the transconductance

in air and liquid is calculated as 33 nA/V and 5.2 nA/V respectively. Resonance frequency of the resonator is calculated as 623 kHz.

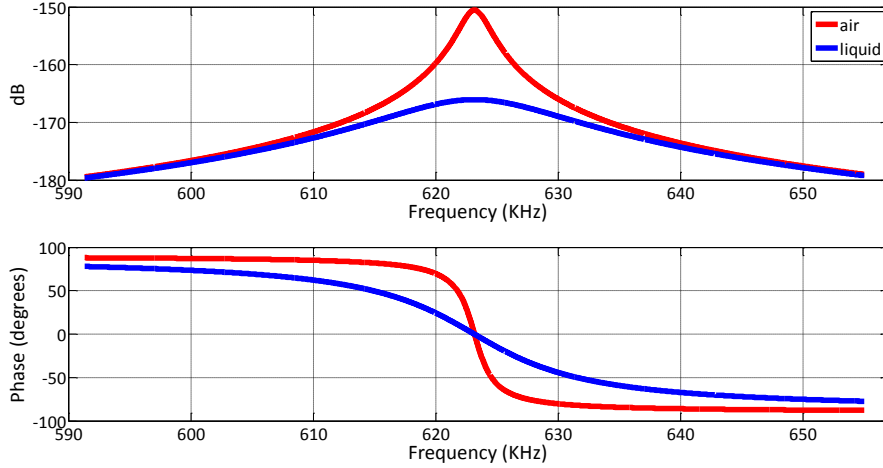


Figure 3-23: Calculated frequency response of RTFS in air (red) and liquid environment (blue)

### 3.3.3. Differential Resonator with Side Fingers (DRSF)

This resonator is designed as a differential resonator to eliminate feedthrough current. However fingers cause increase in squeeze film damping. Therefore number of fingers and length of fingers should be optimized. Length of the resonator is optimized to maximize electrostatic force and output current. In Figure 3-24 the schematic of DRSF is shown.

The transfer function of the designed resonator is given in air and in liquid is given in Equation (3-10) and (3-11) respectively. In Figure 3-25, frequency response of the resonator is shown.

$$\frac{I(s)}{V(s)} = \frac{8.93 * 10^{-13} s}{1.39 * 10^{-9} s^2 + 6.45 * 10^{-6} s + 1.204 * 10^4} \quad (3-10)$$

$$\frac{I(s)}{V(s)} = \frac{8.93 * 10^{-13} s}{1.39 * 10^{-9} s^2 + 5.7 * 10^{-5} s + 1.204 * 10^4} \quad (3-11)$$

The resonator in air has a Q factor 634 and Q after liquid injection is calculated as 72. When the transconductance of resonators are analyzed, the transconductance in air and liquid is calculated as 69 nA/V and 7 nA/V respectively. Resonance frequency of the resonator is calculated as 468 kHz.

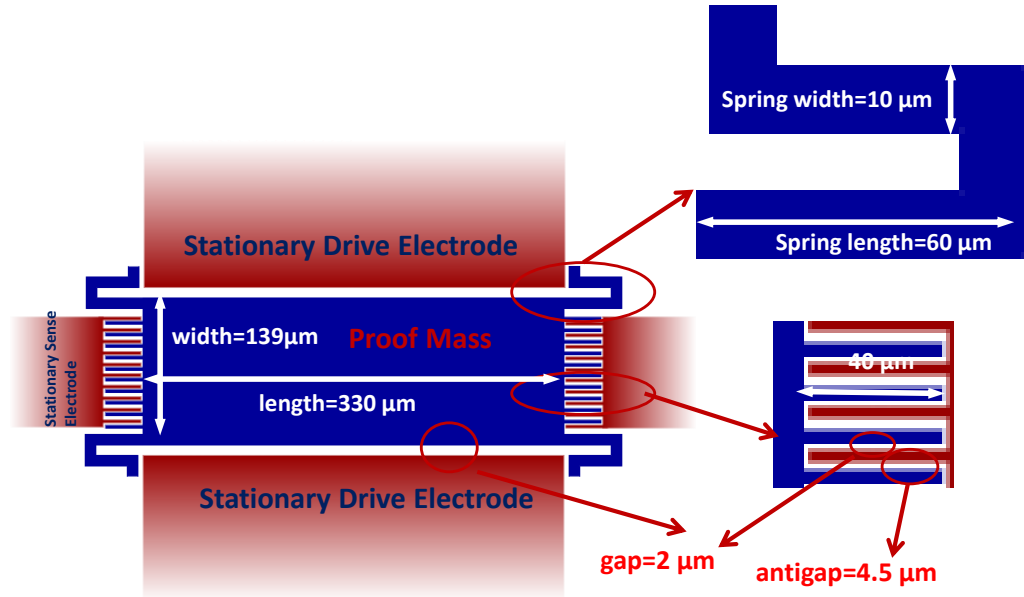


Figure 3-24: The schematic of DRSF

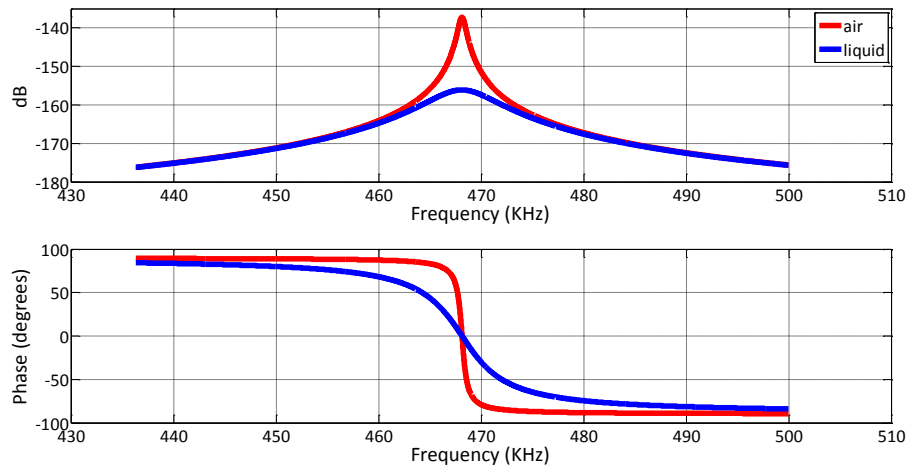


Figure 3-25: Calculated frequency response of DRSF in air (red) and liquid environment (blue)

### 3.3.4. Differential Resonator with Parallelogram Shape (DRPS)

This resonator is a novel differential resonator type to get rid of fingers in DRSF. Fingers are removed from the design and instead of fingers parallelogram shaped resonator is proposed. Doing this, Q of resonator increased while differential operation of resonator continues. In Figure 3-26 the schematic of DRPS is shown. The transfer function of the designed resonator is given in air and in liquid is given in Equations (3-13 respectively. In Figure 3-27, frequency response of the resonator is shown.

$$\frac{I(s)}{V(s)} = \frac{2.44 * 10^{-13}s}{2.55 * 10^{-9}s^2 + 1.28 * 10^{-5}s + 1.204 * 10^4} \quad (3-12)$$

$$\frac{I(s)}{V(s)} = \frac{2.44 * 10^{-13}s}{2.55 * 10^{-9}s^2 + 9.47 * 10^{-5}s + 1.204 * 10^4} \quad (3-13)$$

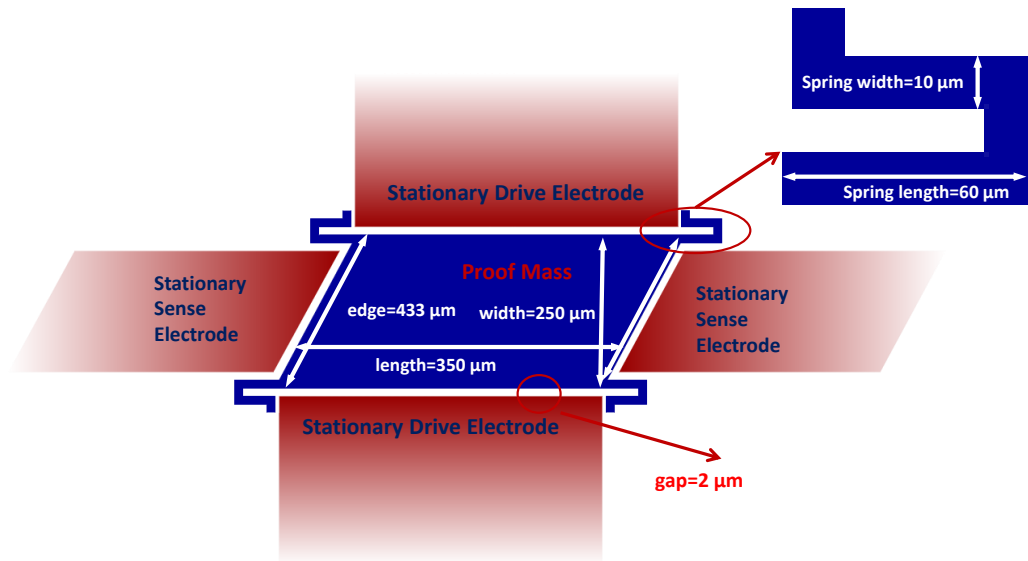


Figure 3-26: The schematic of DRPS with related parameters

The resonator in air has a Q factor 433 and Q after liquid injection is calculated as 58. When the transconductance of resonators are analyzed, the transconductance

in air and liquid is calculated as 85 nA/V and 11.5 nA/V respectively. Resonance frequency of the resonator is calculated as 346 kHz.

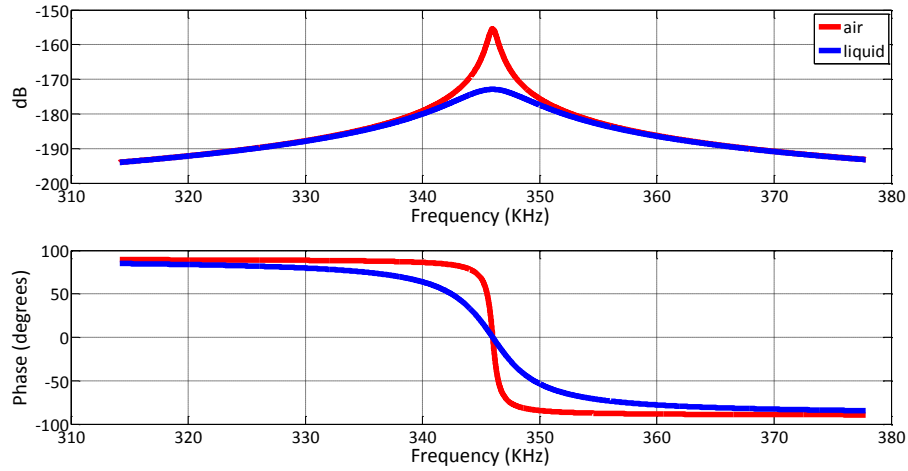


Figure 3-27: Calculated frequency response of DRPS in air (red) and liquid environment (blue)

### 3.4. Effect of Parylene Coating on the operation of resonators

Parylene is used to prevent liquid leakage inside the actuation gap and maintain the proper operation of the resonator under liquid flow. The resonator designs and all calculations under liquid flow is conducted assuming 300 nm parylene layer is coated on the resonators. In this part, effect of parylene on Q and output current in air and liquid will be discussed. Although parylene coating affects spring constant, mass and damping coefficients, for the sake of simplicity the effect of parylene on mass and spring constant is ignored.

Parylene coating decreases the gap and this causes dramatic increase in squeeze film damping. Therefore Q decreases when parylene coated to the resonators. However this drop is more dramatic in air environment since the effective damping mechanism in liquid environment is squeeze film damping. After 500 nm parylene coating, Q of RBS decreases to 123 in air and 46 in liquid

environment theoretically. In Figure 3-28 and Figure 3-29  $Q$  in air and liquid variations with different parylene thicknesses is shown.

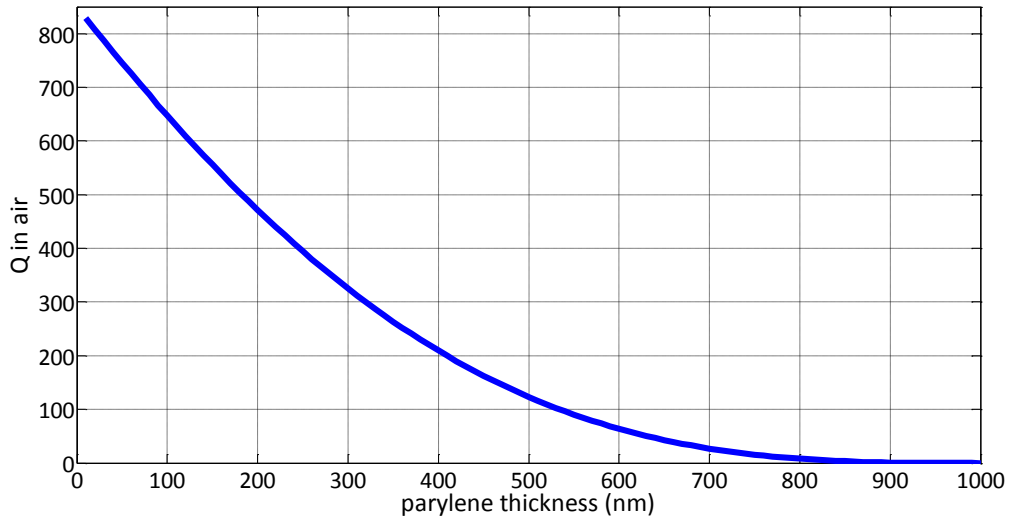


Figure 3-28: Effect of parylene coating on  $Q$  in air environment

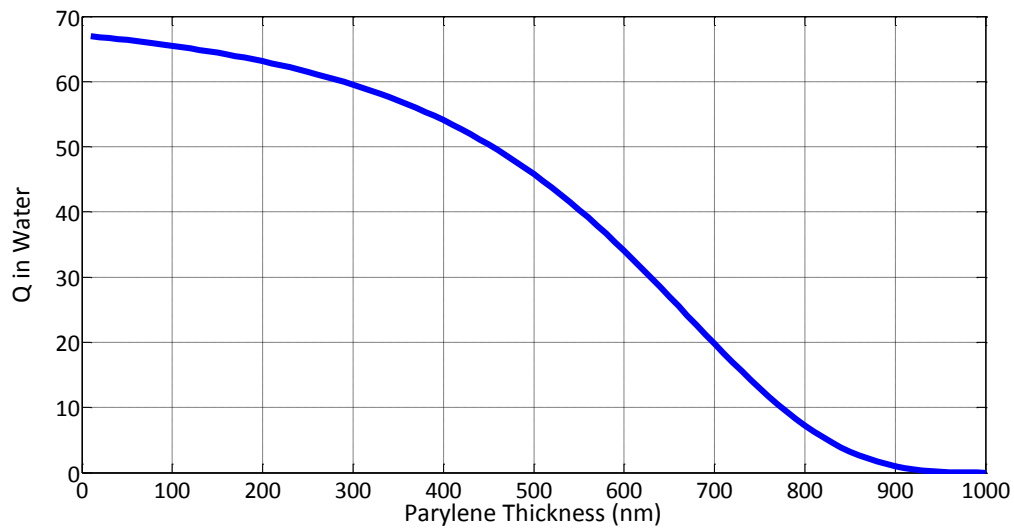


Figure 3-29: Effect of parylene coating on  $Q$  of resonator operating under liquid flow

Output current also decreases since Q decreases significantly. Although output current calculated in air environment without coating is more than 200 nA, it decreases to 30 nA after 500 nm parylene coating. Output current in liquid environment under this condition is calculated as 11 nA. In Figure 3-30 and Figure 3-31, effect of parylene coating on output current in air and liquid environment is shown respectively.

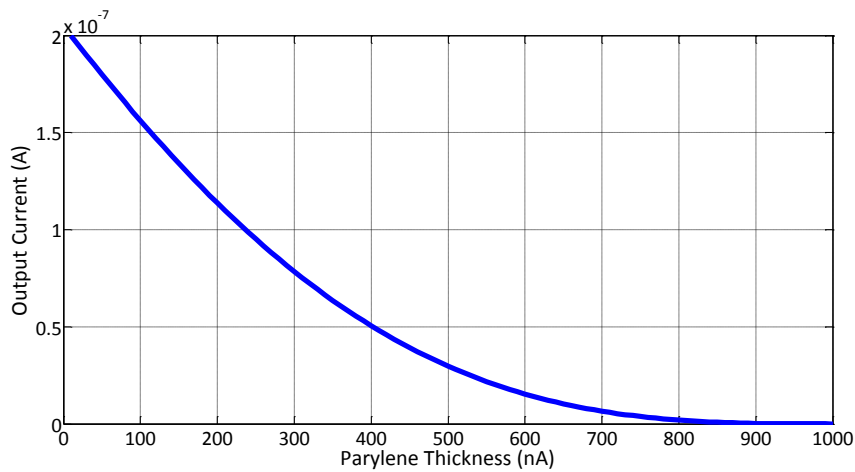


Figure 3-30: Effect of parylene coating on output current measured in air environment

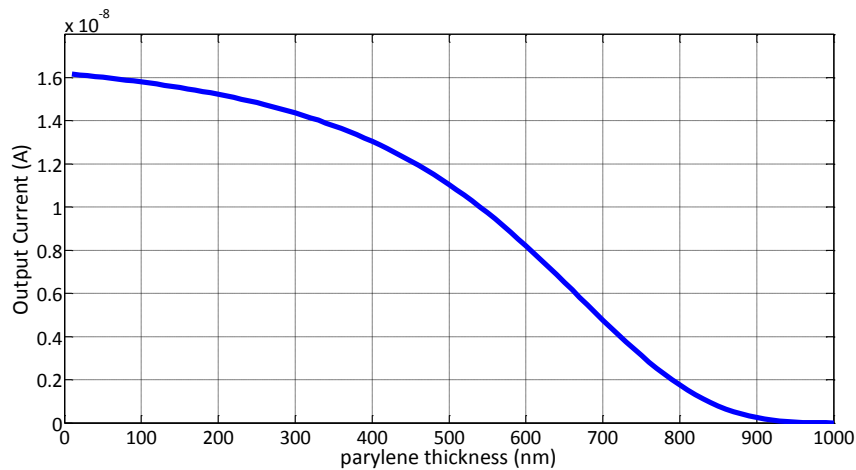


Figure 3-31: Effect of parylene coating on output current measured in liquid environment

### 3.5. Conclusion and Comparison of Designs

In this chapter design parameters of resonators are discussed in detail. Calculations and graphics are obtained for the most basic resonator type RBS. Effect of actuation gap, length, width, thickness and parylene coating on Quality factor and transconductance of resonators are discussed in detail. Different resonator types are designed considering transconductance and Quality factor of resonators. Numeric calculations for all types of the resonators are conducted and to have Q higher than 50 when the resonators are coated with 300 nm parylene layer is aimed and achieved.

*Table 3-1: Comparison of the designed resonator structure*

<b>Resonator ID</b>	<b><math>f_{\text{resonance}}</math> (KHz) (calculated)</b>	<b><math>Q_{\text{air}}</math></b>	<b><math>Q_{\text{liquid}}</math></b>	<b><math>gm_{\text{air}}</math></b>	<b><math>gm_{\text{liquid}}</math></b>
RBS	381	850	60	250	14
RTFS	623	291	44	33	5.2
DRSF	468	634	72	69	7
DRPS	346	433	58	85	11.5

As seen from Table 3-1, the highest performance resonator is RBS although it does not include any finger structure since it is easy to control damping and there are less design parameters in this resonator type. However the last two resonators are differential and feedthrough elimination using differential resonators is more efficient. Moreover the resonator with the code of RTFS includes more nonlinearity which may be used in different read-out techniques.

In the next chapter, feedthrough elimination methods in the literature will be presented and a novel solution to the feedthrough current problem will be proposed.

## **CHAPTER 4**

### **FEEDTHROUGH CURRENT ELIMINATION AND SECOND HARMONIC METHOD**

#### **4.1. Feedthrough Current**

Feedthrough current can be considered as direct coupling between drive and sense electrodes. With decreasing resonator dimensions and increasing resonance frequency, feedthrough phenomena may dominate resonator current and resonance frequency and amplitude of resonator may not be measured directly. Feedthrough current is usually capacitive; therefore it increases with increasing operation frequency.

To observe open loop characteristics of a resonator directly is not possible if feedthrough current dominates resonator characteristics. In this situation post processing may be necessary. To do this first of all proof mass of resonator is polarized and frequency characteristics of device are collected. After collecting active frequency data, proof mass of the resonator is grounded and then current data is collected again. The collected data are subtracted from each other and as a result pure resonance characteristics are obtained. However, this method is not useful for real time observation of resonance characteristics and extra post-processing is required for this method. Moreover without real time elimination of feedthrough current closed loop operation of resonators is not possible.

There are basically two different methods proposed in the literature. First one is based on creating a current that is equal to feedthrough current in terms of

magnitude but lagging  $180^\circ$  to the feedthrough current [45]. To achieve this, two resonators are utilized and one of resonators is polarized and the other resonator is not polarized. Their sense electrodes are shorted each other and drive electrodes are excited with out of phase signals. As a result feedthrough currents cancels each other and only resonator current is observed at the output. In Figure 4-1, this method is shown [46].

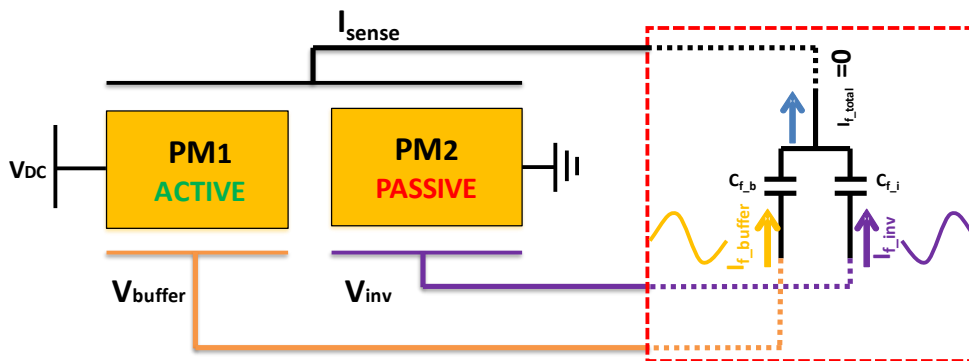


Figure 4-1: The feedthrough current elimination method based on utilizing two resonators

However this method has some drawbacks. First of all feedthrough capacitances of two resonators may not match exactly. In this case feedthrough currents will not be equal to each other and as a result, feedthrough current will not be eliminated completely. Moreover, the  $180^\circ$  phase difference and amplitude matching of drive signals may not be achieved. The details and results of these drawbacks has been discussed by Kangul et. al. in [46].

The other method is utilization of differential resonators. In this method there are one or two drive electrodes and two sense electrodes. The main purpose of this method is generating in phase resonator current and out of phase feedthrough current in sense electrodes or generating out of phase resonator currents and in phase feedthrough currents in sense electrodes. If resonator currents are in phase, sense electrodes are shorted each other and feedthrough currents cancels out each

other or two sense signals are summed with a summing amplifier [46]. If resonator currents are out of phase, sense signals are subtracted from each other and resonator currents are obtained. In Figure 4-2, an example schematic for utilization of differential resonators is given in [46].

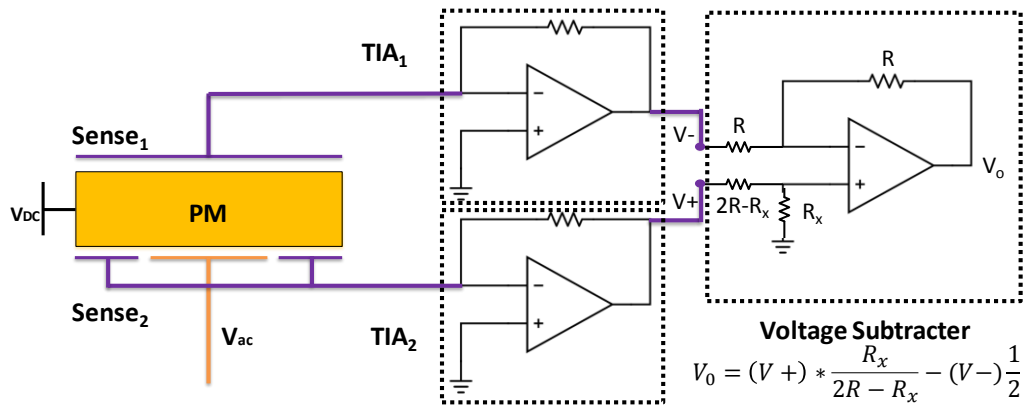


Figure 4-2: The feedthrough current elimination method using differential resonators

In the method used in Figure x, only one drive signal is utilized. Therefore there is no phase mismatch. Possible amplitude mismatches may easily be compensated arranging subtraction coefficients of voltage subtractor. The tests conducted with two methods and conclusion of tests are given in [46].

Another popular method to eliminate feedthrough current is biasing proof mass with ac signal and utilizing the resonator as mixer. In this case feedthrough current and resonator current are separated in frequency domain and resonance current can be extracted using a simple filter. However, generating high frequency and high amplitude signals for proof mass biasing is a challenging task, so this method may not be applicable if proof mass voltage requirement is high.

Although our group is successful for capacitive feedthrough elimination, liquid injection poses problem for proper operation of resonators. Firstly liquid injection decreases resonator current and increases feedthrough current since liquid

injection introduces extra damping and electrical permittivity of water is 80 times higher than the electrical permittivity of air. Moreover since injected liquid is conductive, resistive feedthrough current will be added. Mismatches of parameters (feedthrough current mismatch, amplitude mismatch or phase mismatch) during the elimination of feedthrough current become more critical when liquid is injected since resonator current decreases and feedthrough capacitance increases significantly. Moreover elimination of resistive feedthrough and capacitive feedthrough is not possible with a single stage feedthrough elimination circuit. Utilization of two stage elimination circuit requires extra tuning of circuit.

Although applying ac signal to the proof mass is applicable for such condition, increasing damping causes higher voltage requirement of proof mass voltage.

Instead of applying a sinusoidal signal to the proof mass of the resonator, resonator current and feedthrough current should be separated from each other using another method. As stated in Equation (2-55), sense current in electrostatically actuated includes a second harmonic term. However, feedthrough current is linear since capacitor and resistor are linear elements. Therefore instead of tracking main tone, second harmonic term can be observed to obtain resonator characteristics.

In the rest of this chapter, this new method will be investigated in detail.

#### **4.2. A novel read-out method: Second Harmonic Method**

Although micro-resonator systems are usually considered as linear systems, these systems include nonlinear effects. In Chapter 2, resonator system is considered as linear to understand resonator behavior completely. However to understand second harmonic tone at the output current, nonlinear behavior of the resonator should also be considered.

For an electrostatically actuated varying gap actuator illustrated in Figure 2-2, electrostatic force can be calculated as in Equation (4-1):

$$\begin{aligned}
 F_{electrostatic} &= \nabla E \\
 &= \frac{1}{2} \varepsilon \frac{LW}{(g - x(t))^2} \left( \left( V_{dc}^2 + \frac{v^2}{2} \right) + (2V_{dc}v \cos(\omega t)) \right. \\
 &\quad \left. + \left( \frac{1}{2} v \cos(2\omega t) \right) \right) - \frac{1}{2} \varepsilon \frac{LW}{(g + x(t))^2} V_{dc}^2
 \end{aligned} \tag{4-1}$$

The electrostatic force includes two nonlinearity effects. First of all the force is proportional with the square of voltage difference between electrodes. Therefore second harmonic and dc forces are generated. Moreover force changes simultaneously with changing displacement. This also creates nonlinear effects.

The generated electrostatic force actuates the resonating system according to Equation (4-2).

$$mx''(t) + bx'(t) + kx(t) = F_{electrostatic}, \quad x(0) = 0, \quad \dot{x}(0) = 0 \tag{4-2}$$

Eq. 2 is a nonlinear differential equation. It can be discretized to solve it numerically.

In this case electrostatic force can be discretized in Equation (4-3).

$$\begin{aligned}
 F_{electrostatic} &= \frac{1}{2} \varepsilon \frac{LW}{(g - x[n])^2} \left( \left( V_{dc}^2 + \frac{v^2}{2} \right) + (2V_{dc}v \cos(\omega n T_s)) \right. \\
 &\quad \left. + \left( \frac{1}{2} v \cos(2\omega n T_s) \right) \right) - \frac{1}{2} \varepsilon \frac{LW}{(g + x[n])^2} V_{dc}^2
 \end{aligned} \tag{4-3}$$

where  $T_s$  is sampling rate. Second derivative in differential to difference conversion:

$$x''(t) = \frac{x[n+2] + x[n] - 2x[n+1]}{T_s^2} \quad (4-4)$$

$$x'(t) = \frac{x[n+1] - x[n]}{T_s} \quad (4-5)$$

Combining Equations (4-3), (4-4) and (4-5) we will reach Equation (4-6).

$$\begin{aligned} m \frac{x[n+2] + x[n] - 2x[n+1]}{T_s^2} + b \frac{x[n+1] - x[n]}{T_s} + kx[n] \\ = \frac{1}{2} \varepsilon \frac{LW}{(g - x[n])^2} \left( \left( V_{dc}^2 + \frac{v^2}{2} \right) + (2V_{dc}v \cos(\omega n T_s)) \right. \\ \left. + \left( \frac{1}{2} v \cos(2\omega n T_s) \right) \right) \\ - \frac{1}{2} \varepsilon \frac{LW}{(g + x[n])^2} V_{dc}^2, \quad x[0] = x[1] = 0 \end{aligned} \quad (4-6)$$

For the RBS resonator designed solution of displacement in time and frequency domain when the resonator is excited at. Moreover solution of the equation with excitement signal at 176 kHz (half of the resonance frequency), 280 kHz (a random frequency), 382 kHz (the resonance frequency) and 764 kHz (twice of the resonance frequency) is given at Figure 4-3.

As seen from Figure 4-3, the displacement of resonator does not include higher harmonic terms due to its bandpass nature. However when excited at the other frequencies, higher order terms are observed. In fact, when the resonator is excited with half of the resonance frequency, the dominant frequency term at the output is observed at the resonance frequency. However since the displacement is too small, such an actuation is not proper for resonance frequency sensing.

To calculate the output current we should use Equation (4-7).

$$i = V_{ac}\epsilon \frac{LW}{(g - x(t))^2} \frac{dx}{dt} \quad (4-7)$$

To solve the equation, Equation (4-7) is needed to be discretized as in Equation (4-8).

$$i[n] = V_{ac}\epsilon \frac{LW}{(g - x[n])^2} * \frac{x[n + 1] - x[n]}{T_s} \quad (4-8)$$

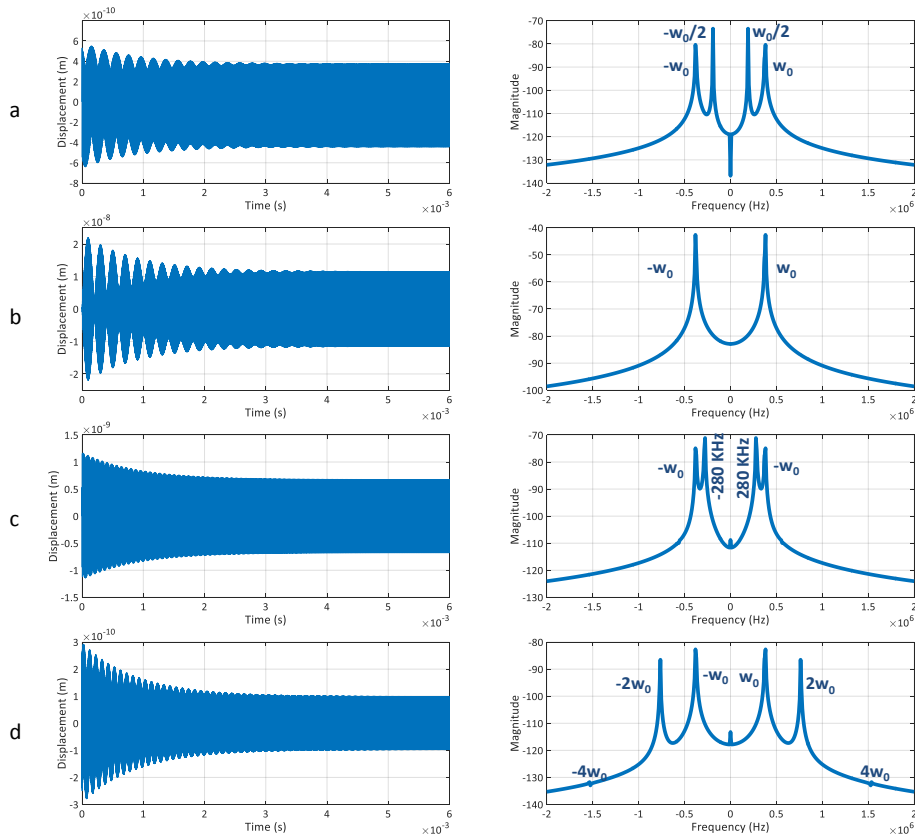


Figure 4-3: Time and frequency domain solutions of nonlinear differential equations with different excitation frequencies. In (a), the resonator is excited with  $\omega_0/2$ . Although it was excited with half of the resonance frequency second harmonic term at the electrostatic force causes second harmonic term at the displacement. In (b), the resonator is excited with  $\omega_0$ . Higher order harmonics components of the force are filtered out by the

*resonator itself and there is no distortion term. In (c), resonator is excited with 280 KHz excitation signal. Although it is not subharmonic or superharmonic of the resonance frequency resonance frequency component is observed at the displacement due to the transient response of the resonator. In (d) the resonator is excited with  $2\omega_0$  and the resonance frequency component is observed at the spectrum of displacement.*

In Figure 4-4, time and frequency domain solution of output current is shown when the resonator is excited its resonance frequency at 176 kHz, 280 kHz, 382 kHz and 764 kHz.

As seen from Figure 4-4, the output term includes second harmonic term at the output when it is excited at its resonance frequency although there is no higher harmonic term at the displacement. Therefore to calculate second harmonic term at the output we can ignore the nonlinearities of electrostatic force and assume the movement is completely linear for the frequencies close to the resonance frequency.

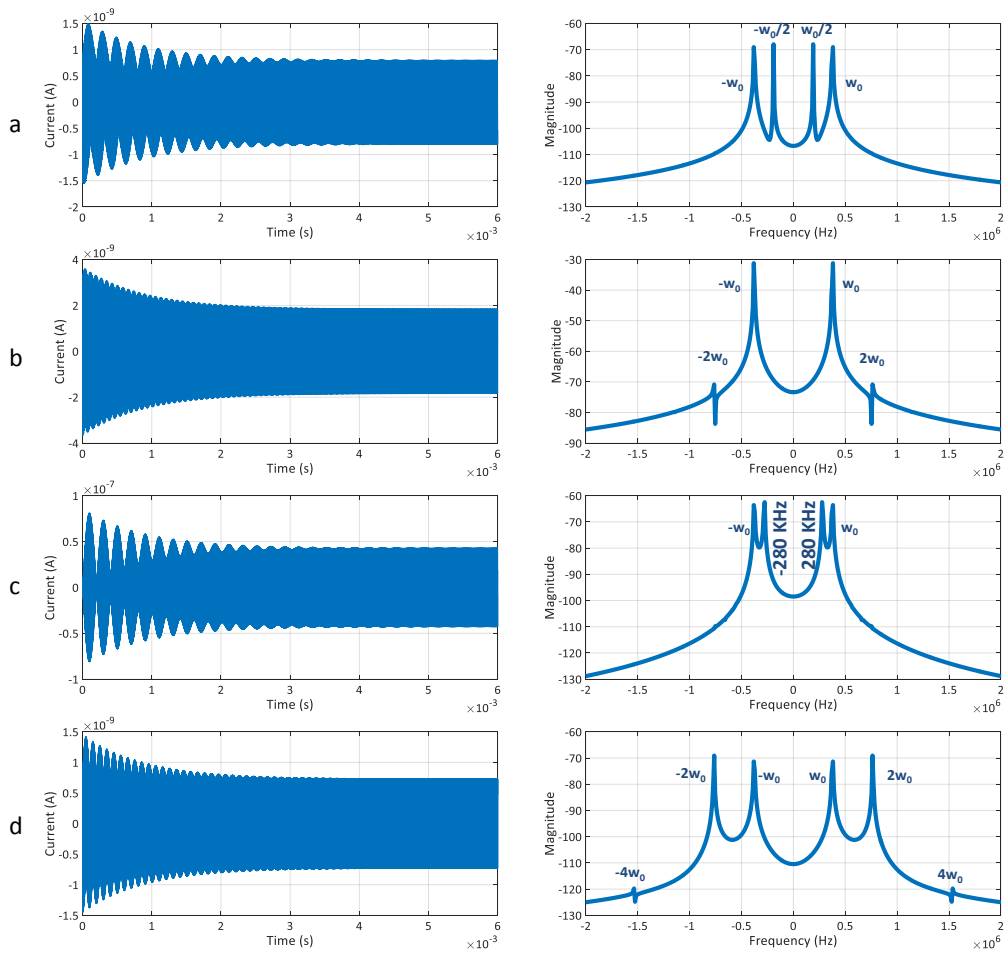


Figure 4-4: Time and frequency domain solutions of output current expression with different excitation frequencies. In (a) the resonator is excited with  $\omega_0/2$  and the resonance frequency term at the displacement is reflected into the output current. In (b), the resonator is excited with its resonance frequency  $\omega_0$  and despite of the fact that displacement is almost completely linear, there is second harmonic term at the output due to the nonlinearity of sensing mechanism. In (c) the resonator is excited with 280 KHz signal and the resonance frequency term at the displacement is reflected into output current term. In (d) the resonator is excited with  $2\omega_0$  but the resonance frequency term observed at the displacement term is reflected into output current term.

In the light of the observations, now we are assuming that the movement is completely linear.

$$x(t) = x_0 \sin(\omega t) \quad (4-9)$$

$$i_{sense} \cong V_{DC} * \varepsilon \frac{A}{(d)^2} \left( \left( 1 - \frac{2x}{d} + \frac{3x^2}{d^2} \right) * \dot{x} \right) \quad (4-10)$$

$$i \cong V_{DC} \varepsilon \frac{A}{(d)^2} x_0 \omega \left( \left( \left( \left( 1 + \frac{3x_0^2}{4d^2} \right) \cos(\omega t) \right) - \left( \frac{2x_0}{d} \sin(2\omega t) \right) \right. \right. \\ \left. \left. + \left( \frac{3x_0^2}{4d^2} \cos(3\omega t) \right) \right) \right) \quad (4-11)$$

As seen from Equation (4-11), we can calculate second harmonic term easily with linear displacement assumption for the frequencies close to the resonance frequency. Moreover we observe that second harmonic term is proportional with the square of the displacement which causes sharper frequency response.

### 4.3. The proposed read-out method

The new method is based on sensing second harmonic term to track resonance frequency of the resonator. To do this, the resonator is needed to be excited and the output current will be converted into voltage. After converting the current to voltage, this voltage is multiplied with the excitation signal. As a result main tone at the resonator output is modulated to DC and 2<sup>nd</sup> harmonic terms. 2<sup>nd</sup> harmonic term at the resonator output is modulated to main tone and 3<sup>rd</sup> harmonic terms. Therefore 2<sup>nd</sup> harmonic term at the output can be observed from the network analyzer. Since feedthrough current is capacitive, it is generated in main tone. 2<sup>nd</sup> harmonic term has sharper frequency response which provides a resonator system with higher Q. The other very important output component, the feedthrough current, on the other hand, ideally appears only on the main tone. Therefore, a

frequency window in the second harmonic will decrease the feedthrough current to the noise level. This theoretically implies complete separation of the feedthrough current and the resonator current from each other at the output.

In Figure 4-5, schematic of the proposed method is given.

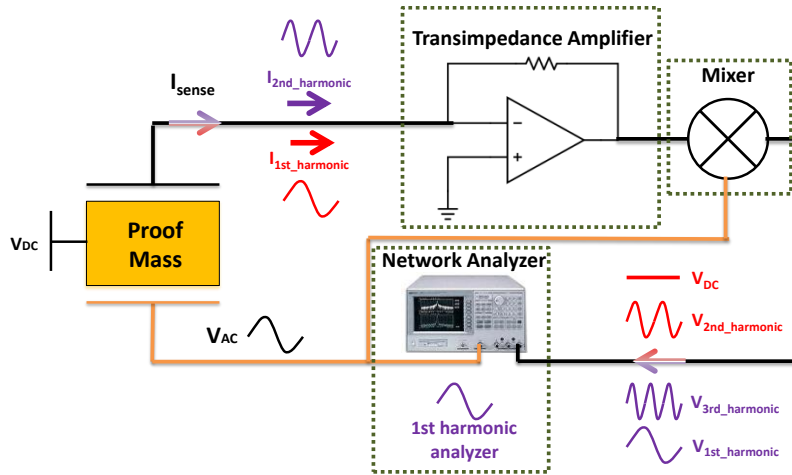


Figure 4-5: The schematic of the proposed method

For RBS resonator amplitude of main harmonic and second harmonic terms are investigated using MATLAB and in Figure 4-6, the simulation result is shown. Q of the resonating system increased from 855 to 1342 (55%). It can be seen that, when the proposed method is used higher Q will be observed. Higher Q system will increase minimum detectable mass. Moreover thanks to this method Q drop under liquid flow will also be compensated.

Although ideally there is no feedthrough in the second harmonic term, it can be observed at the output of mixer. Inputs of mixers are not completely isolated from output and so they can couple to the output of mixer which generates extra feedthrough to the second harmonic term. Therefore while using this method mixer should be chosen very carefully. Feedthrough of mixer and minimum operating voltage of mixer should be especially considered.

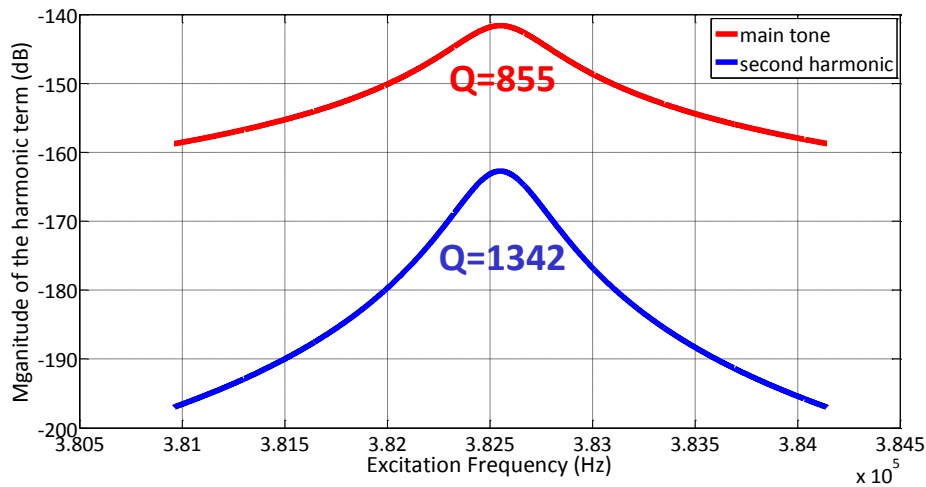


Figure 4-6: Magnitudes of second harmonic and main tone signals with different excitement frequencies

#### 4.4. Conclusion

In conclusion there are a few methods to eliminate feedthrough current in the literature. These methods are based on creating out of phase copy of feedthrough current and cancelling it on sense electrode or subtracting the total signal from the copy of feedthrough elimination. However these methods are very sensitive to parasitic and mismatches. Therefore these methods are not applicable for resonators operating inside liquid medium. The proposed method is based on utilization of internal nonlinearities of electrostatic resonator. In this method output signal of resonator is modulated with the actuation signal, second harmonic at the output is detected. The proposed method is a good candidate to be used in resonators for gravimetric mass sensing applications, where the resonator size must be minimized to have a high mass sensitivity and Q of the resonator drops significantly due to interaction with viscous media [38].

## CHAPTER 5

### FABRICATION OF RESONATORS

In the previous chapter novel resonator structures are designed and a novel read-out technique is introduced. Although it is not mentioned in the design chapter, fabrication of resonators is a challenge and affects the performance of resonators significantly. Embedding the designed resonators on top wall of a microchannel is a challenging task and its process requires high care in all steps of the fabrication. The resulting device is a microchannel carrying suspended resonators and they are so delicate. Moreover dimensions of resonators are so critical. For example even small changes or nonuniformities in actuation gaps may cause unpredictable changes of the performance of resonators. Since there have been studies on resonators more than ten years in our group, a robust and high yield fabrication process is available. However, there are some problems in the current process flow and they should be chosen for implementation of high performance resonators on microchannels. In this chapter, fabrication process of the designed resonators will be explained in detail.

#### **5.1. Former Fabrication Process**

A high yield fabrication method for the gravimetric sensors has been developed by T. Toral [47]. Although with this fabrication process yield increased significantly, some problems of proposed fabrication method have been solved by

M. Kangul and the modified high yield fabrication process proposed by Kangul, is shown in Figure 5-1.

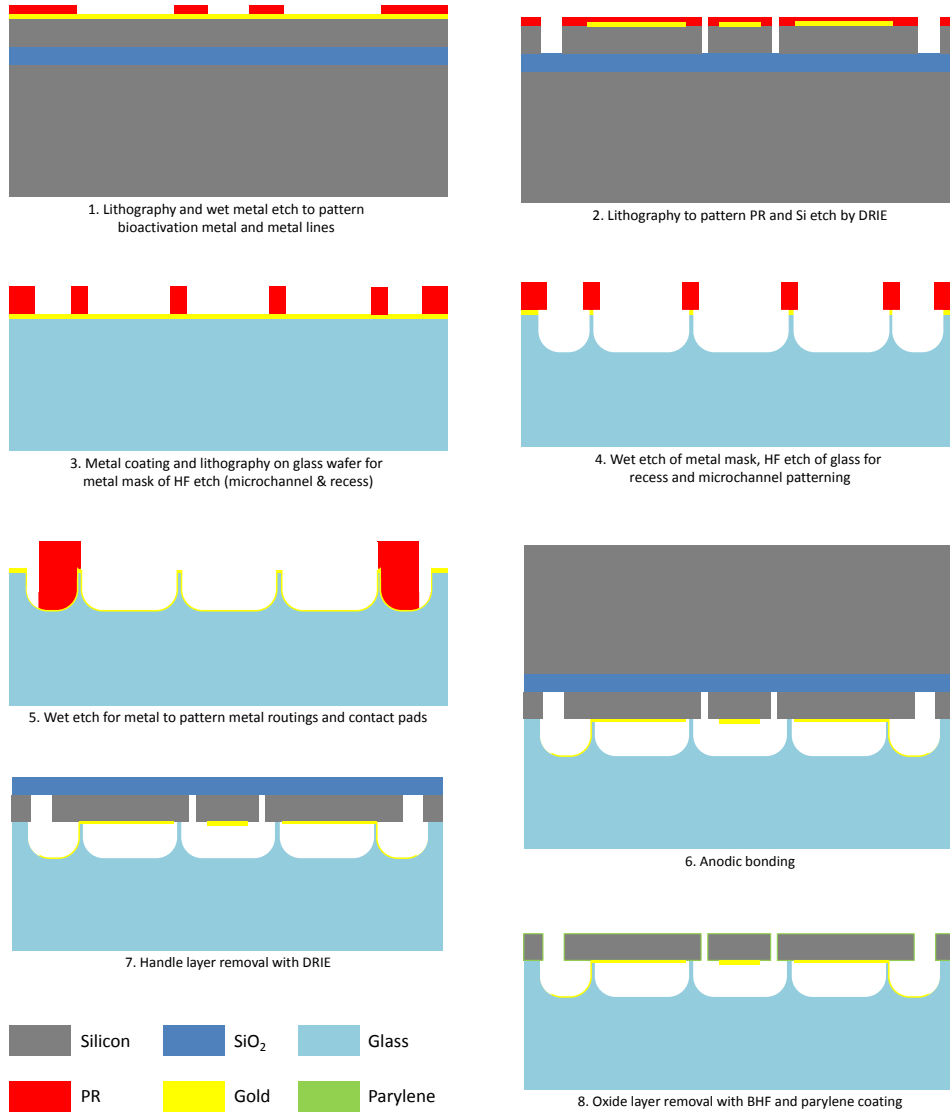


Figure 5-1: The former fabrication process of resonators[35]

With this fabrication process, most problems have been solved but there are still some problems.

First problem is observed due to metal residue on silicon. Sputtered chrome on silicon diffuses through the silicon and this residue cannot be etched completely

with chrome etchant. The diffused chrome layers prevent proper operation of Deep Reactive Ion Etching (DRIE). As a result, resonator structure cannot be built properly. To solve this problem, metal should not touch the whole silicon area. Therefore utilization of lift of process is a good solution for this problem.

Another problem is electrical insulation of proof mass from microchannel. When liquid is injected inside microchannel, a path between microchannel and ground may be generated if any defect is observed in parylene layer. This causes electrolysis of liquid inside microchannel. Therefore proof mass and microchannel should be isolated from each other. To do this, bio-activation gold should not touch silicon directly.

Furthermore, during anodic bonding temperature is increased to 370°C. This temperature causes metals diffuse inside silicon and also disruption of metals. To prevent this, a thermally insulating layer between silicon and metal layers should be placed.

## 5.2. The New Fabrication Process

In this section, the new fabrication flow will be presented firstly and then all process steps will be explained in detail. In Table 5-1 process flow of the fabrication flow is given.

*Table 5-1: The proposed fabrication step with explanations*

Step	Process description	Cross-section after process
1.	Start with a 4-inch (100) SoI wafer	

Table 5-1 continued

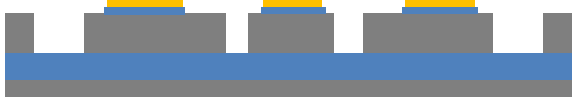
2.	PECVD Oxide coating and patterning with 1:5 BHF	
3.	Lithography, Cr/Au Sputtering and Lift off (50 nm/150 nm)	
4.	DRIE, Resonator construction	
5.	4 inch glass wafer	
6.	Metal coating and patterning for HF etch	
7.	HF etching	
8.	PR and metal stripping	

Table 5-1 continued

9.	Metal coating and electrode patterning	
10.	Anodic Bonding	
11.	Handle layer removal (DRIE)	
12.	Buried oxide layer removal (BHF) and releasing of suspended structures with acetone-IPA-methanol	

### 5.2.1. Wafer selection and Cleaning

For this process, 4" SoI wafers with 10  $\mu\text{m}$  active device thickness is used. High mass sensitivity, high quality factor and high output current are important considerations while designing resonators. Decreasing thickness will increase mass sensitivity but, there is an optimum SoI thickness for high Q and output current. Having an SoI with lower thicknesses will make fabrication harder and

decrease the yield. However having an SoI with higher thickness will increase damping. Therefore resonators are optimized considering a layer of 10  $\mu\text{m}$ .

Moreover, again 4" glass wafers will be used to construct the microchannel and the recesses. The glass wafer will be bonded anodically to the SoI wafer.

### **5.2.2. Coating with an isolation layer**

An isolation layer is required on the proof mass since it is supplied with 100 Volts DC. Without an isolation layer, electrolysis may be observed during in liquid tests. Moreover, addition of the insulation layer will prevent diffusion of gold into silicon during bonding processes since they are performed at relatively high temperatures (anodic bonding is performed at 370°C).  $\text{SiO}_2$  is used as the insulation layer. In Figure 5-2 patterned  $\text{SiO}_2$  is shown.  $\text{SiO}_2$  is patterned using 1:5 BHF with photoresist mask.

### **5.2.3. Metal Routing on Silicon**

After deposition of the insulation layer, it will be patterned and a routing on silicon will be created using liftoff. In this step, proof mass activation layers will also be constructed. To have sharper photoresist walls, image reversal photoresist (AZ-5214) is used. Moreover thickness of metals is arranged approximately one tenth of resist thickness (30 nm Cr/ 150 nm Au). In Figure 5-3, bio-activation layer of RTFS is shown. To prevent short circuit while liquid is flowing from microchannel, bio-activation layer is constructed on insulator silicon layer. Moreover it prevents metal diffusion inside silicon and change of metal shape during anodic bonding process. To use conductivity of silicon layer, there is no oxide layer at the beginning and the end of the routing.

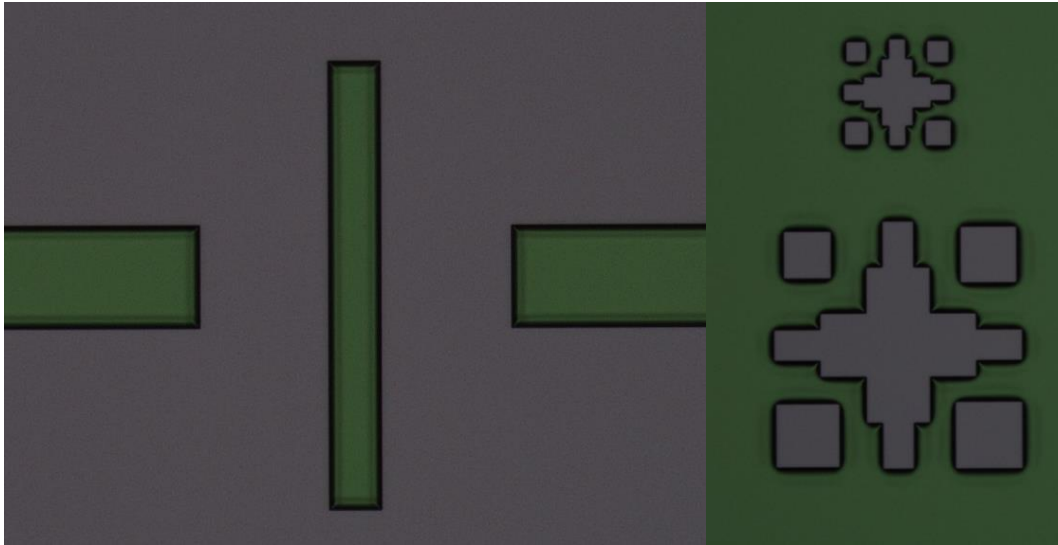


*Figure 5-2: Patterned SiO<sub>2</sub> layer on the silicon surface. As seen, BHF etching is isotropic and corners are rounded due to the overcut of BHF*

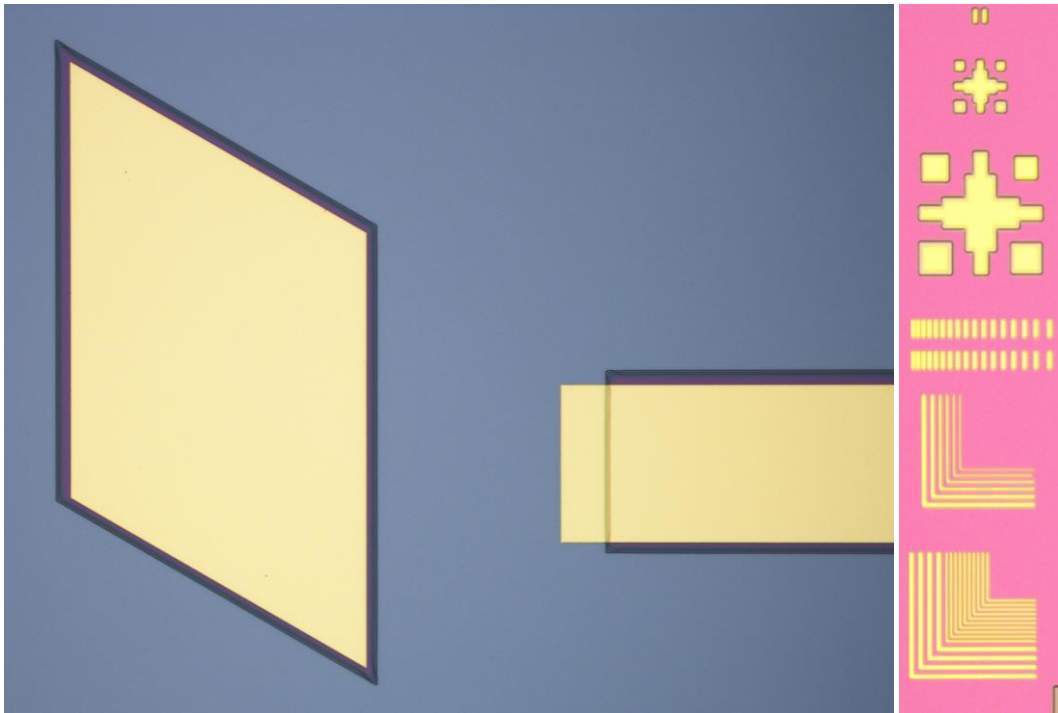


*Figure 5-3: Photograph of the silicon surface after lift-off process*

#### 5.2.4. Device patterning

In this step, devices will be constructed using DRIE. The minimum gap we need is  $2\ \mu\text{m}$ . We need precise dimensions and straight side walls. We cannot achieve these requirements using wet etching techniques. Therefore, we used DRIE. In Figure 5-4 and Figure 5-5 microscope views and SEM photographs of patterned devices are shown. Moreover as seen from **Hata! Başvuru kaynağı bulunamadı.**, minimum gap requirement has been achieved successfully and finger of resonators has been constructed properly.

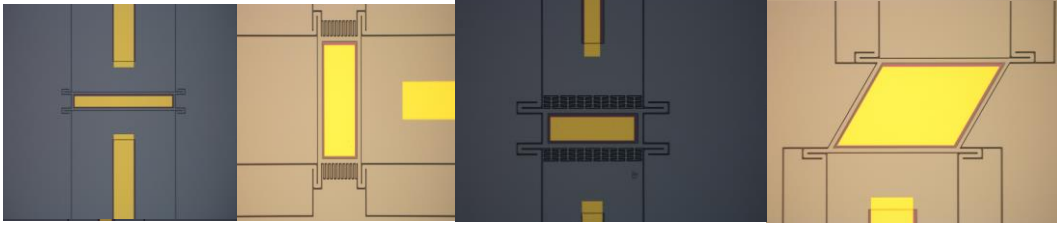


Figure 5-4: Microscope views of patterned devices

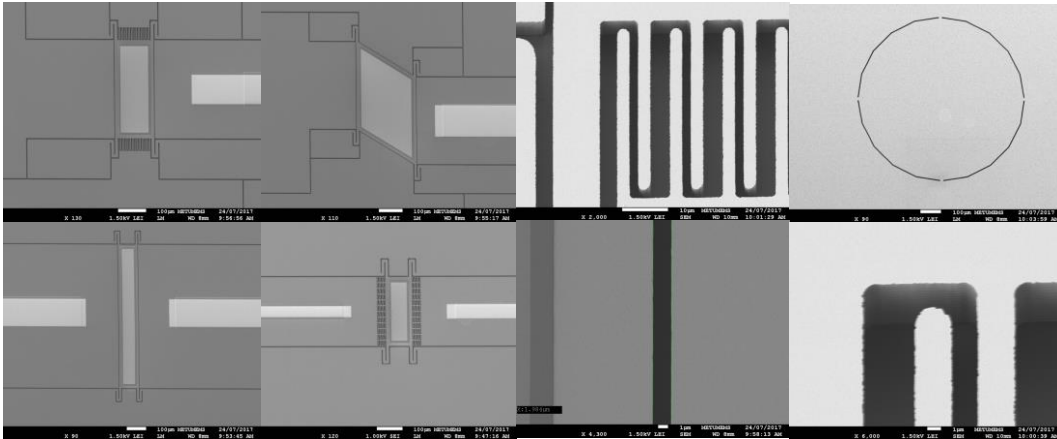


Figure 5-5: SEM images of patterned devices and various regions of wafer. As seen,  $2\ \mu\text{m}$  gap is achieved and scallops on the walls are observed

#### 5.2.5. Microchannel and Recess Construction

The liquid will flow through the microchannel. The depth of the microchannel should be arranged considering the dimensions of CTCs. A  $20\ \mu\text{m}$ -deep channel is

comparable with CTC dimensions (The dimensions of CTCs are range from 10  $\mu\text{m}$  to 20  $\mu\text{m}$ ). Smaller channel depth may cause squeezing of the cells inside the microchannel. Larger channel depth may cause reduce the chance of interaction between the cells and the resonator surface and consequently preventing proper operation of the resonator. Therefore, we should keep the depth of microchannel about 20  $\mu\text{m}$ .

Recess is required to maintain bonding areas due to metal routings. Therefore, we are opening recesses below metal routings. In this process recesses and the microchannel is constructed in same mask. In this case recess depth is supposed to be equal to microchannel depth.

First, the glass wafer is coated with Cr/Au layer and then it is patterned. The metal masked glass wafer is etched using 50% HF in order to construct the 20  $\mu\text{m}$  deep microchannel. Afterwards, microchannel and recess construction metals will be stripped and the glass wafer is put in 1:7 BHF to smooth edges of recesses for electrodes.

While drawing microchannel and recess mask, one should consider the undercut issue. HF's undercut ratio is 1.5 [47], which means we will observe 25-30  $\mu\text{m}$  undercut to the right and left for a 20  $\mu\text{m}$  microchannel.

In Figure 5-6, glass wafer after microchannel construction is shown.

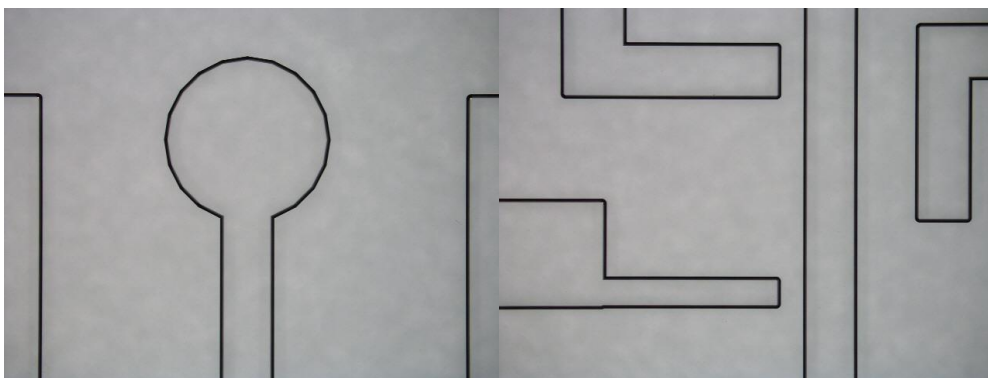


*Figure 5-6: Microchannel and recess opened on glass wafer*

### 5.2.6. Electrode Formation

Electrodes will be constructed on the glass wafer and will contact the routing during the bonding process. Electrodes may be patterned with wet metal etch process using commercial etchants. As electrode/pad material we will use 50 nm Cr/300 nm Au layer. Pads will be on glass since pins will apply pressure to the pads. If the pads were constructed on Silicon layer, they would probably be broken after the first test. Therefore, pads should be on the glass wafer. In Figure 5-7, the microscope image of electrodes and METU symbol constructed with metal etching technique is shown.

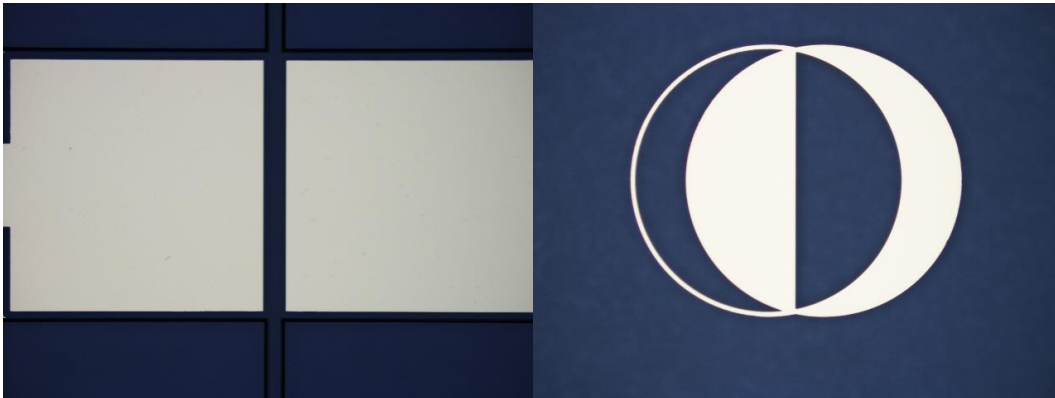


*Figure 5-7: Electrodes constructed on the glass wafer*

### 5.2.7. Anodic Bonding

Glass and SoI wafers will be bonded using anodic bonding technique. Before doing this process both wafers are cleaned with piranha solution and silicon wafer put inside 1:7 BHF to activate the silicon surface and etch native oxide. Anodic bonding process was performed at 370°C temperature with 1200 Volts voltage and 1000 Newton force. All silicon islands should be shorted each other to prevent sparks during anodic bonding. The shorting should be done at the edge of the dies to get rid of short circuits after dicing. For further measurement the current should be limited as well. The metals on silicon and glass are bonded each other and construct contact as shown in Figure 5-8. There are some unbonded

regions which can be seen around the metal-metal bonding area. However there is no such region around the microchannel. Therefore any liquid leakage is not observed during the operation of resonators.



*Figure 5-8: Contact regions of metals and resonating devices after anodic bonding*

#### **5.2.8. Handle layer and buried Oxide Removal.**

To make the resonator movable, it should be suspended. However, handle and buried oxide layers prevent the movement of the resonator. Therefore, after bonding, handle layer of SoI wafer will be removed using grinder and DRIE respectively. Handle layer of the wafers are 350  $\mu\text{m}$  and first 250  $\mu\text{m}$  of handle layer is removed with grinder. Further handle layer removal with grinder becomes risky since it may break the wafer. Last 100  $\mu\text{m}$  of the handle silicon layer was etched using DRIE. 2  $\mu\text{m}$  buried oxide is removed using 1:5 BHF for 35 minutes.

### 5.2.9. Releasing Suspended Structures

To prevent stiction, suspended structures are released by washing in Acetone, IPA and methanol, respectively. After methanol washing wafer is dried using a hot plate with temperature 70°C. Using critical point dryer is another alternative. In Figure 5-9 the microscope images of suspended devices are given. As seen, there is no notching due to DRIE. In Figure 5-10 a pad and microchannel inlet are shown. After releasing the resonators, the lids of pads and microchannel inlets/outlets are broken.

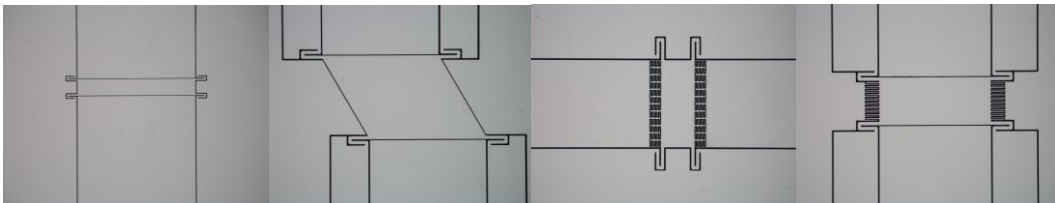


*Figure 5-9: microscope views of suspended resonators*



*Figure 5-10: Pads and microchannel inlets after breaking the lids*

### 5.2.10. Parylene Coating

To achieve hydrophobicity and biocompatibility devices are coated with 500 nm parylene layer after releasing them.

### 5.3. Parylene Bonding Process

Although this fabrication process solves metal diffusion problems and electrical insulation problems, bio-activation is not reliable since it is not possible to etch parylene selectively in this process. To achieve this, the designed devices are fabricated a new fabrication method proposed by Gokce et. al. [48].

Parylene will be used in these devices due to its electrical properties, hydrophobicity and suitability as a bonding material. First, parylene provides electrical insulation between the electrodes and the liquid. Consequently, sense and drive electrodes are not directly coupled to water, thanks to parylene. Moreover, parylene prevents liquid leakage between gaps on top of the microchannel due to its hydrophobicity. Another property of parylene is its biocompatibility. Cells should touch a biocompatible surface. The last property of parylene is its utilization/availability as a bonding material. Since we need all properties mentioned above, we chose parylene for this process.

A 0.5  $\mu\text{m}$ -thick parylene layer will be coated on the Silicon layer and then it will be patterned using RIE. Having a thicker parylene layer will result in a more conformal coating and decrease liquid leakage possibility. However, doing this will increase squeeze film damping significantly. Increasing gaps for thicker parylene coating may be useful but it will increase the output current. After patterning parylene, processing of the SoI wafer will be finished.

Glass and SoI wafers will be bonded using parylene bonding technique.

In the previous processes which were explained, we were using anodic bonding. In anodic bonding process, there are two problems. The first problem we faced was that it is not possible to coat the wafer with parylene before bonding. Therefore, we were not able to etch parylene selectively. Therefore, we were not sure about electrical insulation, biocompatibility and bareness of the bioactivation gold. The other problem we faced was that routing metals were diffusing into

silicon and their shape was changing. Coating insulation layer would probably prevent this problem. However since parylene bonding process is realized at lower temperatures, metal diffusion problem is completely solved by parylene bonding process.



*Figure 5-11: Cross section of wafers and process masks*

In Figure 5-11 cross section of wafers and process masks with addition parylene mask is given. If the parylene mask is excluded from the mask set, same mask set can be used for anodic bonding process.

In Figure 5-12, the parylene bonding process flow proposed by Gokce et al. [48] is given. The designed devices are fabricated with both anodic bonding and parylene bonding processes.

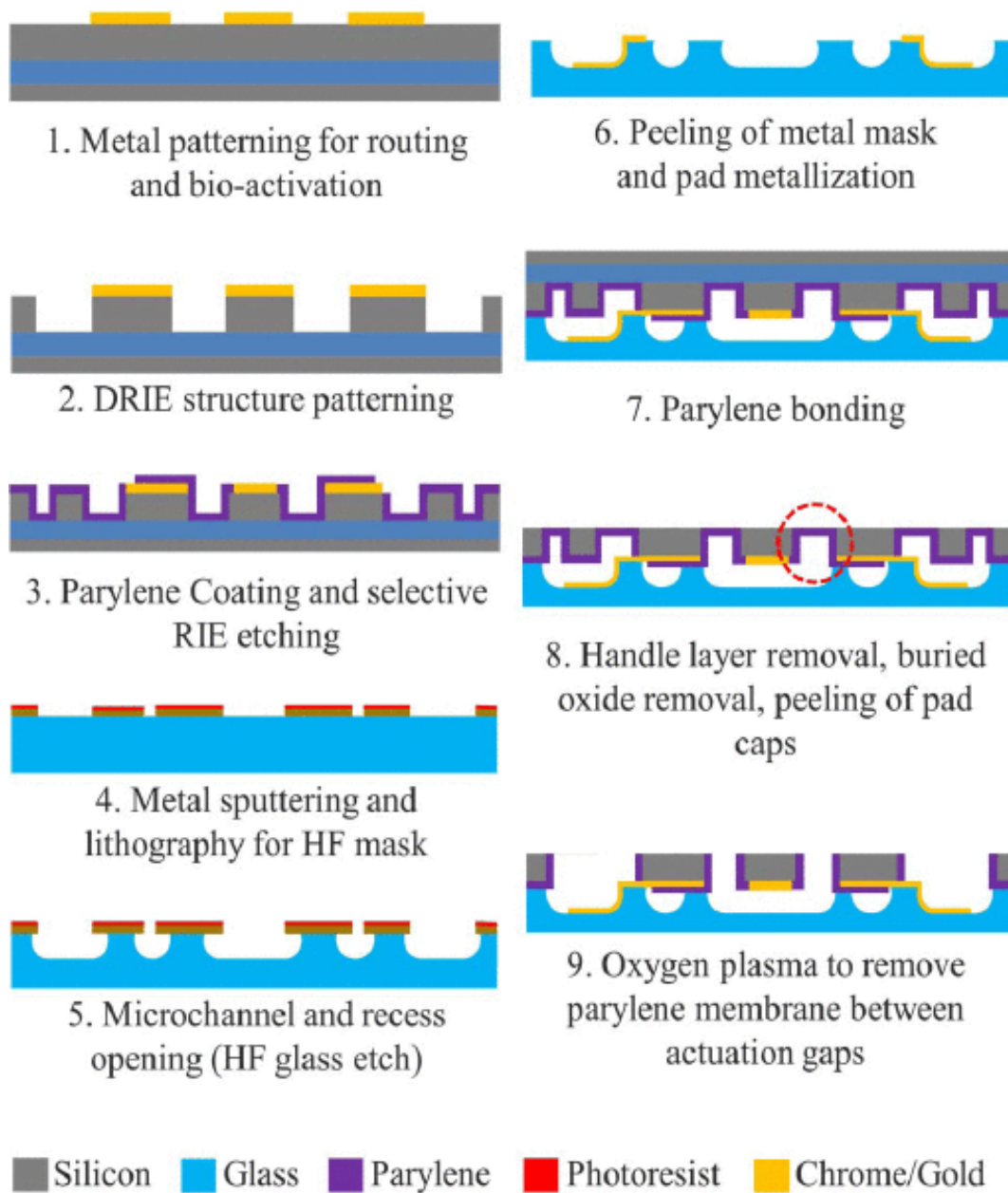
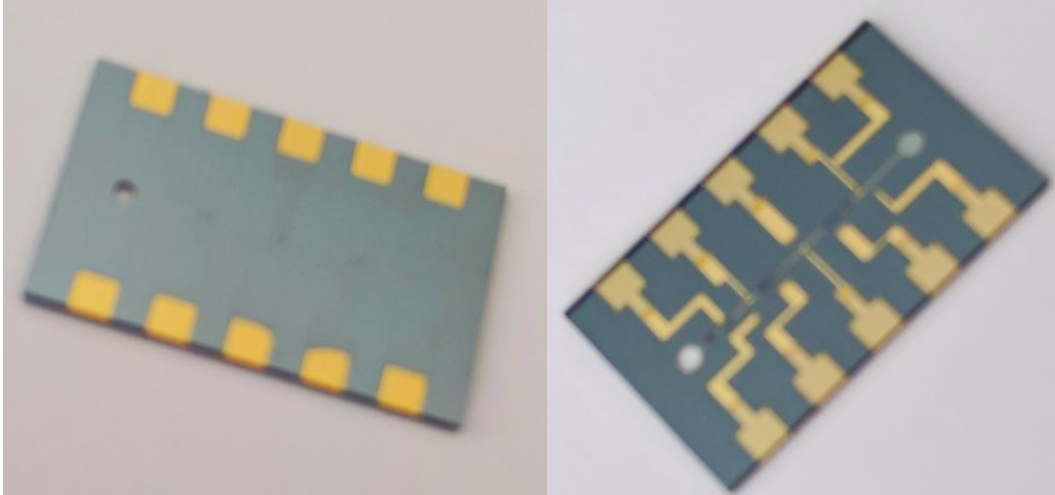


Figure 5-12: Parylene bonding process proposed by Gokce et. al. [48]

#### 5.4. Conclusion

In this chapter fabrication steps for the designed resonators are presented in detail. Fabrication processes for similar devices was discussed and their problems are mentioned. After all, new fabrication process is proposed and all fabrication steps

are presented in detail. After each fabrication step, detailed inspection is performed and photos are shown for further explanations. In Figure 5-13 the photograph of the fabricated die is shown.



*Figure 5-13: Fabricated die photographs (left: top view, right: bottom view)*

Moreover a new fabrication process based on parylene bonding proposed by Gokce et. al.[48] is presented in this chapter.

In the next chapter test setup and test results of the resonators will be presented.

## CHAPTER 6

### EXPERIMENTAL RESULTS

This chapter explains experimental work performed with the designed resonators. First experimental setup and the designed circuit for second harmonic method will be explained. After explaining test setup, characterization results of resonators will be given and then second harmonic test results will be given.

#### 6.1. Test Setup and Read-out Circuitry

The designed resonators are tested utilizing two different test setups. In the first test setup probe station is used. Read-out circuitry and resonators are connected each other using the probe station. In Figure 6-1, the test setup is shown. High voltage DC supply is utilized to polarize the device under test and power supply is utilized to power up read out electronics. Resonator is directly excited using RF output of network analyzer. Sense current is converted into voltage thanks to 1 M $\Omega$  transimpedance amplifier (TIA) and the output of TIA is given as input to the network analyzer. Network analyzer compares its input and output signals in terms of amplitude and phase and gives phase response of the resonator.

Due to the feedthrough current, it is not possible to directly obtain resonator characteristics. Elimination of feedthrough current is possible using different methods as explained in Chapter 4. However there is another method to obtain resonator characteristics directly. In this method, proof mass is grounded after obtaining characteristics of resonator when proof mass is polarized and in this

case resonator system is inactive and so only feedthrough current is measured. After collecting data, the results are subtracted from each other and as a result pure resonance characteristics are obtained.

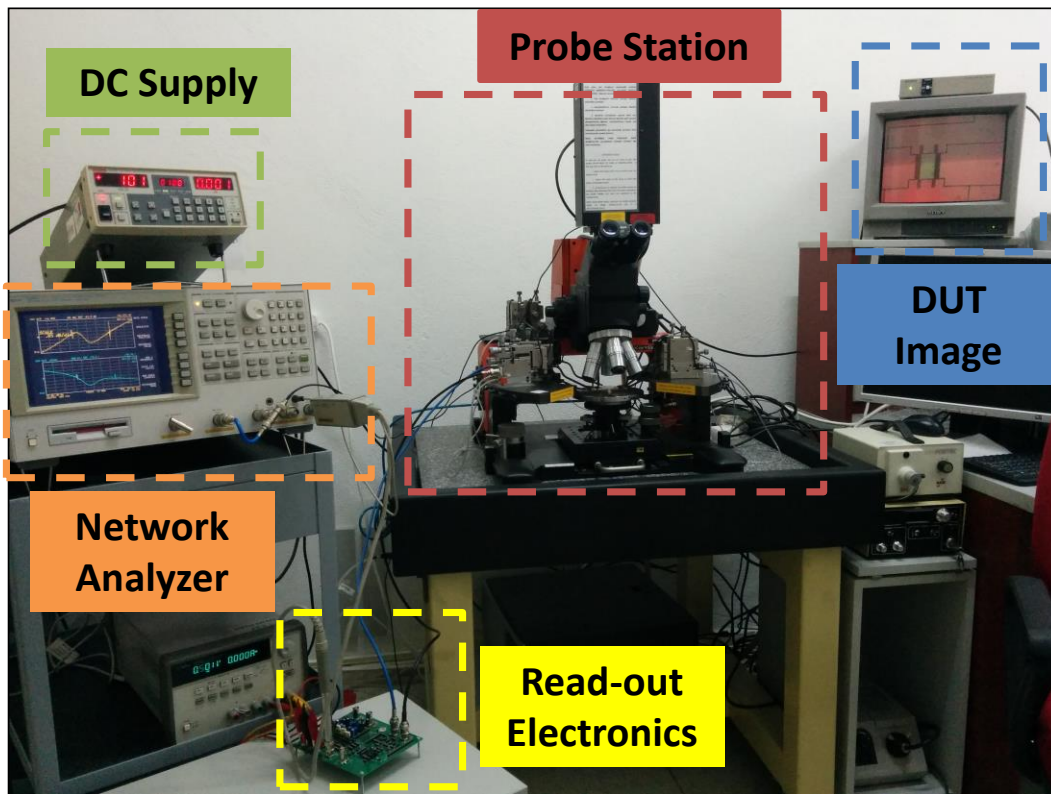


*Figure 6-1: The test setup with probe station*

The other test setup for the resonators is utilized a custom designed chip holder shown in Figure 6-2. The holder has two parts. In the first part the chip is placed inside a recess. Microchannel part is visible and observable using inverted microscope. The other part of the holder carries electrical and microfluidic connections. Electrical connections are achieved using pogo-pins that touches pads of the device under test. Pogopins are connected to headers that can be used as input or output. Proof mass of resonators can be polarized using headers. Resonators are also excited applying signal to the related header and output

current can be read from headers. Microchannel inlet and outlet of the resonator is reachable from the holder. The high voltage DC supply, network analyzer, power supply and the read-out circuitry is required for this test setup as well.

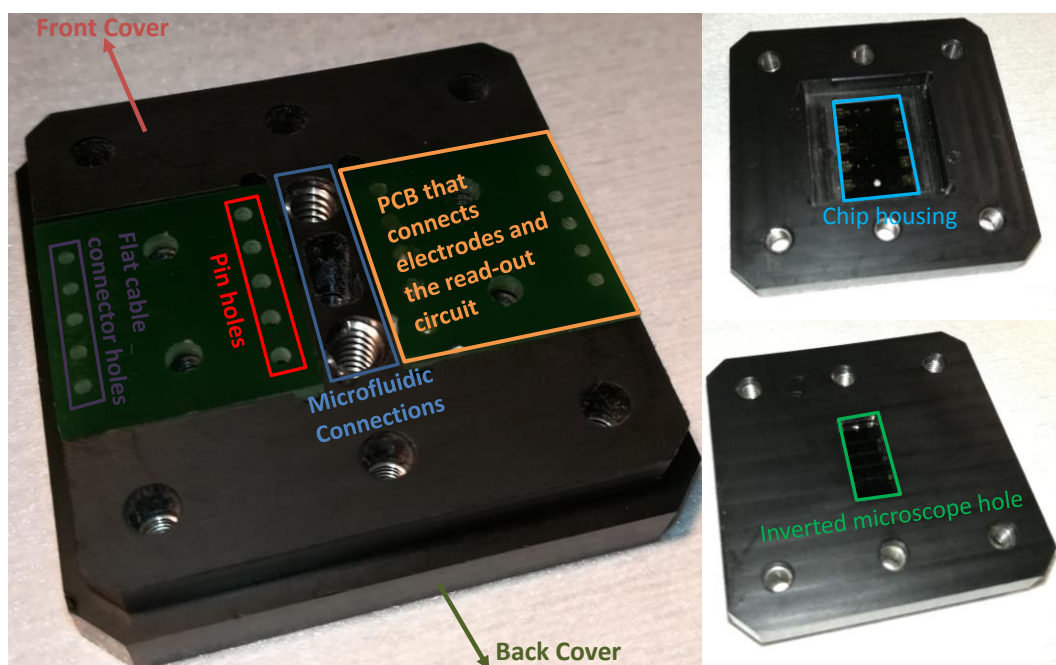


*Figure 6-2: Image of the holder designed to test resonators. After resonators are placed inside the chip housing front cover is closed on the back cover. Electrical and microfluidic connections are done from the front cover. Liquid flow may be observed from the microscope hole.*

For characterization purpose a transimpedance amplifier is utilized. Both inverting and noninverting transimpedance amplifiers are available shown in Figure 6-3. The major drawback of noninverting transimpedance amplifier is that there is no virtual ground at the sense electrode and the resistance connected between sense electrode and ground applies a feedback to the resonating system. Therefore we chose to use inverting transimpedance amplifier for characterization of resonators. LM741 and OPA656 opamps are utilized in transimpedance amplifiers. For second harmonic measurements, output of TIA is multiplied with the drive signal

utilizing a modulator with the model of AD630 produced by Analog Devices. The schematic of readout circuitry and measurement nodes are shown in Figure 6-4.

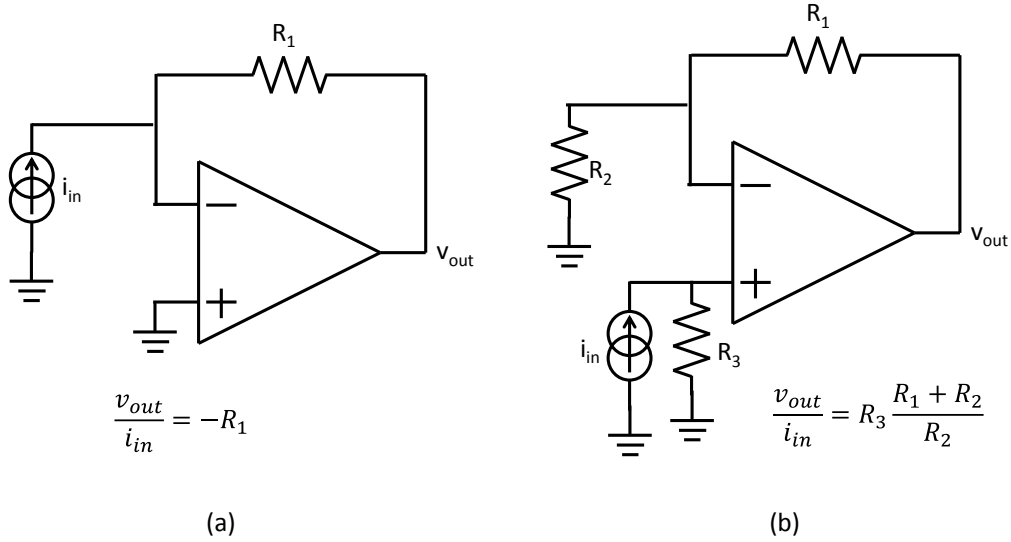


Figure 6-3: Schematics of inverting (a) and noninverting (b) transimpedance amplifiers

## 6.2. Resonator Characterization Results and Comparison of Experimental Results and Simulation Results

### 6.2.1. RBS

In Figure 6-6 and Figure 6-7, raw and postprocessed characterization result of RBS resonator is shown.

The resonator is polarized with 100 Volts DC and excited with 14.4 dBm power. As seen from the raw data, output current is so high that it is 10 dB higher than the feedthrough level. After postprocessing it is seen that, peak value of the voltage gain measured is -5 dB. The gain of TIA is 120 dB and as a result 560 nA/V transconductance is obtained at the resonance frequency. Q and resonance frequency of the resonator are measured as 590 and 330.5 kHz respectively.

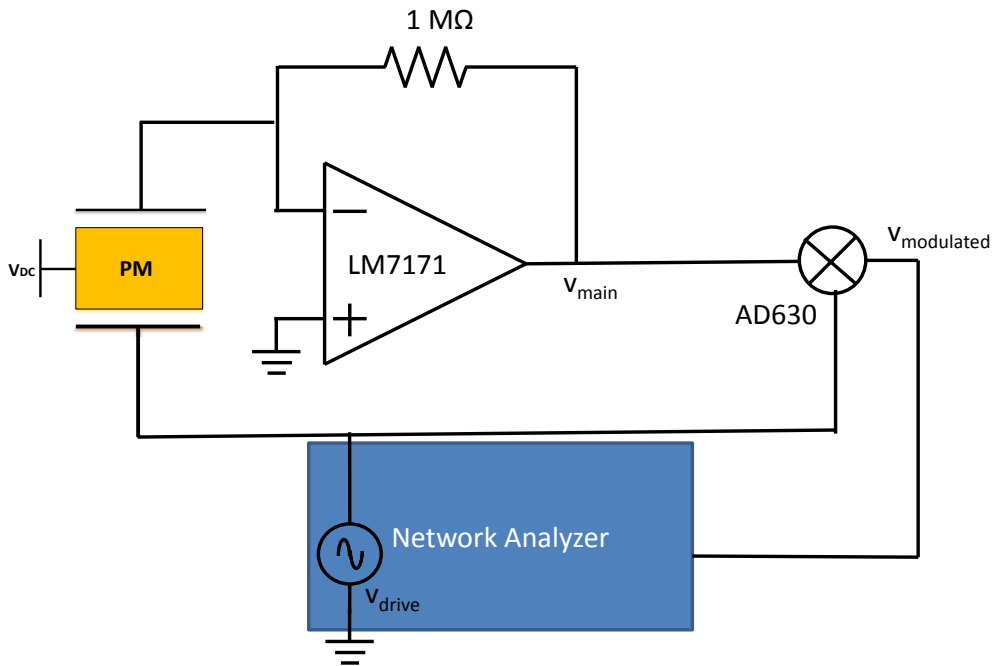


Figure 6-4: Schematic of second harmonic measurement setup

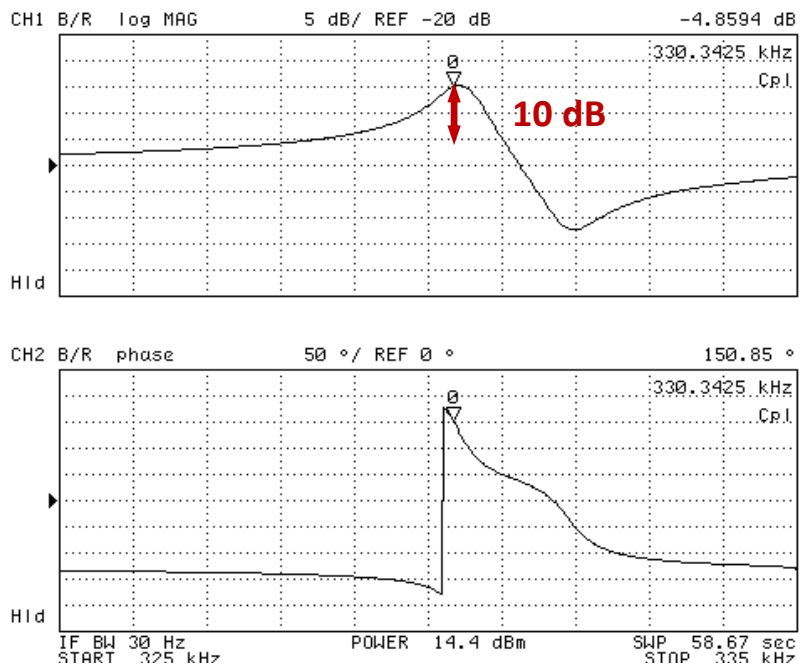
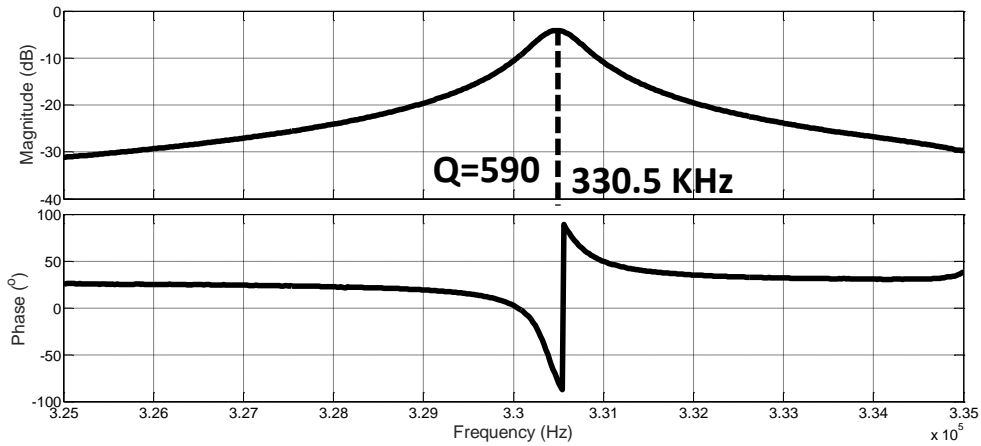


Figure 6-5: Raw frequency response of RBS taken from the network analyzer



*Figure 6-6: Postprocessed characterisation of RBS*

### **6.2.2. RTFS**

This resonator is tested utilizing the test setup with holder. Moreover resonator fabricated with parylene bonding technique is tested. For characterization proof mass is polarized with 80 Volt DC and the resonator is excited with 15 dBm excitation voltage. Since there are lots of fingers in this structure, nonlinearity is observed obviously in the resonance characteristics. In Figure 6-7 and Figure 6-8, raw and postprocessed characterization result of RTFS resonator is shown respectively. Q and resonance frequency of the device under test is measured as 310 and 579.6 KHz respectively. The transconductance at the resonance frequency was measured as 31.6 nA/V.

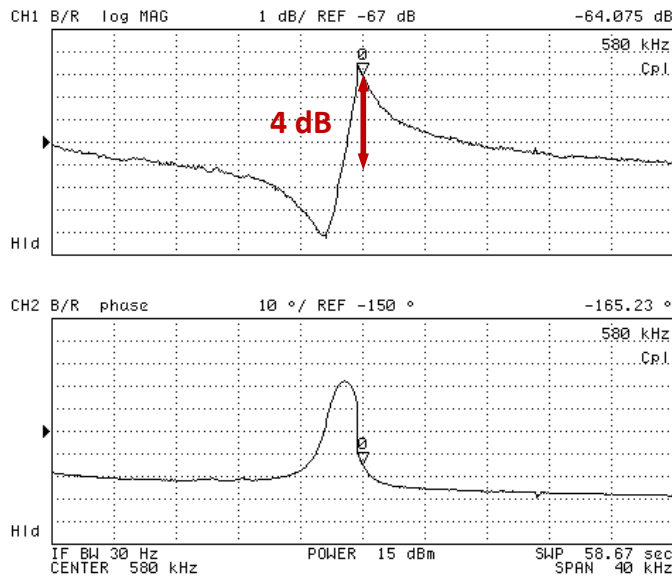


Figure 6-7: Raw frequency response of RTFS taken from the network analyzer

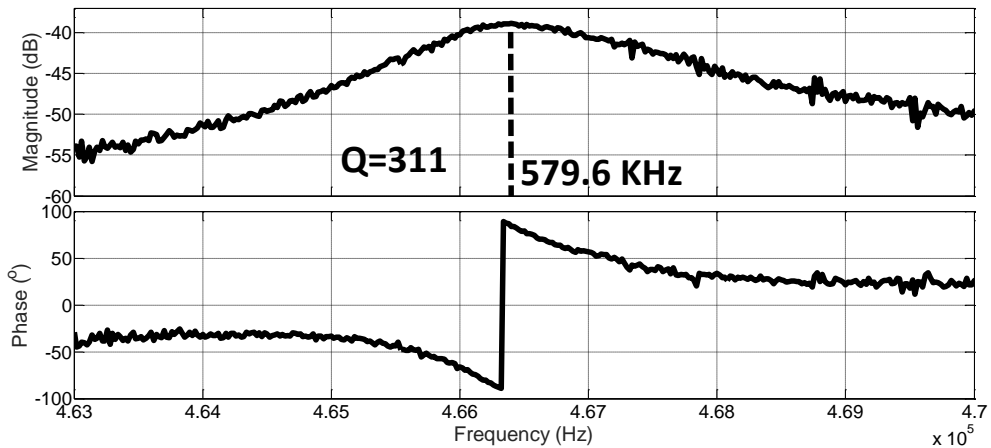


Figure 6-8: Postprocessed resonance characteristics of RTFS

### 6.2.3. DRSF

This resonator is tested with probe station. It was excited with -10 dBm RF power and proof mass was polarized with 80 Volts DC. In Figure 6-9 and Figure 6-10, raw and postprocessed characterization result of DRSF resonator is shown .

As seen from Figure 6-10, resonance frequency is measured as 466.4 KHz and Q is measured as 311. The transconductance at the resonance frequency is measured as 11 nA/V.

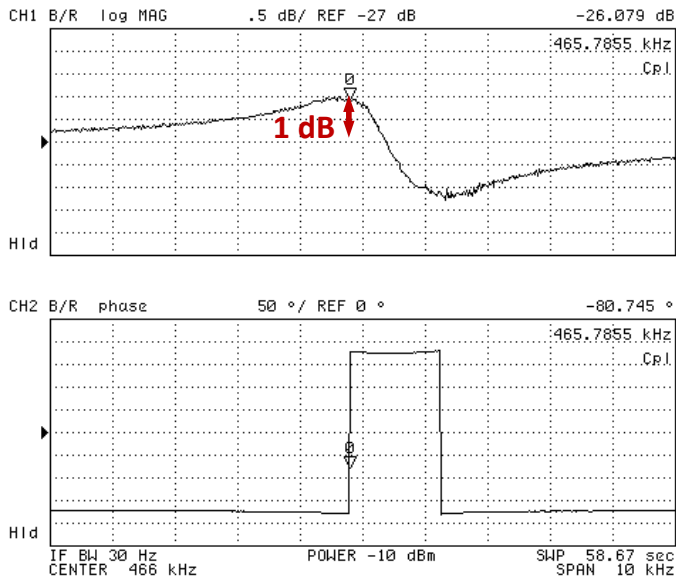


Figure 6-9: Raw frequency response of DRSF taken from the network analyzer

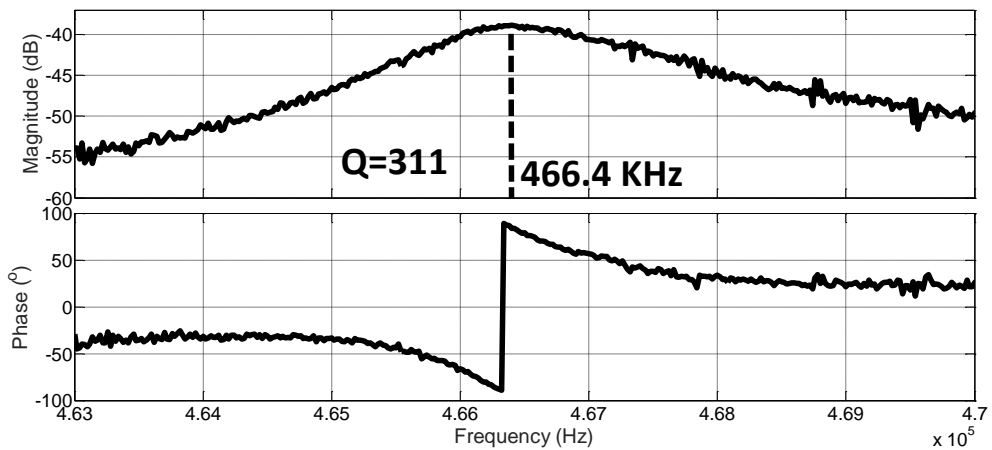


Figure 6-10: Postprocessed resonance characteristics of DRSF

#### 6.2.4. DRPS

This resonator is tested with probe station. The proof mass polarization voltage is 80 Volts and the excitation power 0 dBm. The resonance frequency of this resonator is measured as 360 KHz and Q is measured as 202. The maximum transconductance at the resonance frequency is measured as 5 nA/V. In Figure 6-12 and Figure 6-13, raw and postprocessed characterization result of DRPS resonator is shown respectively.

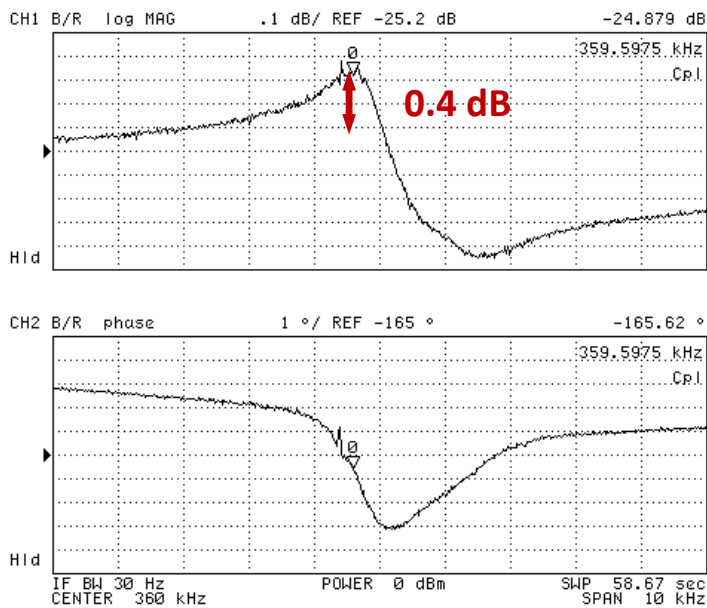


Figure 6-11: Raw frequency response of DRPS taken from the network analyzer

#### 6.2.5. Comparison of Experiments and Simulations

In Table 6-1, the measured and simulated resonance frequency, Q and maximum transconductance values are compared. As seen from the table, resonance frequencies of all resonators calculated consistent with the experimental results. However Q of the systems are measured lower than the expected values. In simulations the only damping mechanism is considered as air damping and the other damping mechanisms are ignored. Therefore deviation of Q values are quite

normal. Since damping values could not be calculated exactly, the maximum transconductances are calculated higher than the measured values.

Although simulations are not fitting exactly with the experiments, simulations are giving important and meaningful data about the performances of the resonators.

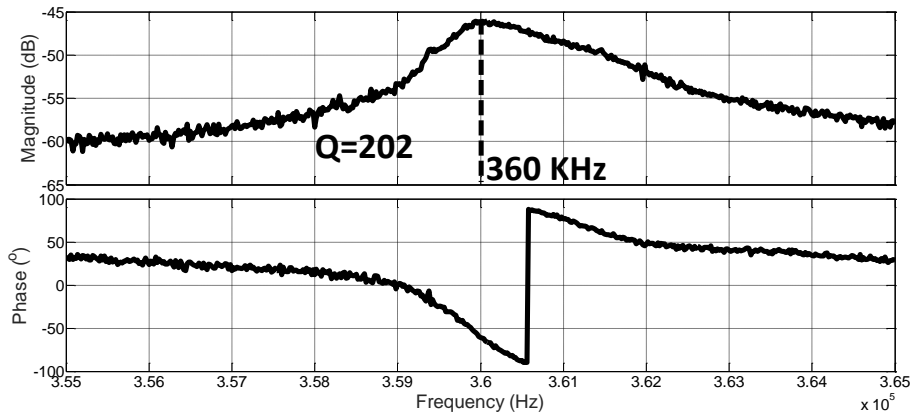


Figure 6-12: Postprocessed resonance characteristics of DRPS

Table 6-1: Comparison of calculations with experiments

Resonator ID	$f_{\text{resonance}}$ (KHz) (calculated)	$f_{\text{resonance}}$ (KHz) (measured)	Q (calculated)	Q (measured)	gm (nA/V) (calculated)	gm (nA/V) (measured)
RBS	381	330.5	850	590	250	500
RTFS	623	579.6	291	310	33	31.6
DRSF	468	466.4	634	311	69	11.2
DRPS	346	360	433	202	85	5

### 6.3. Test of parylene coated devices and test under liquid flow

The device with the code RBS, is coated with 500 nm parylene and tested. Test result is taken directly from the network analyzer shown in

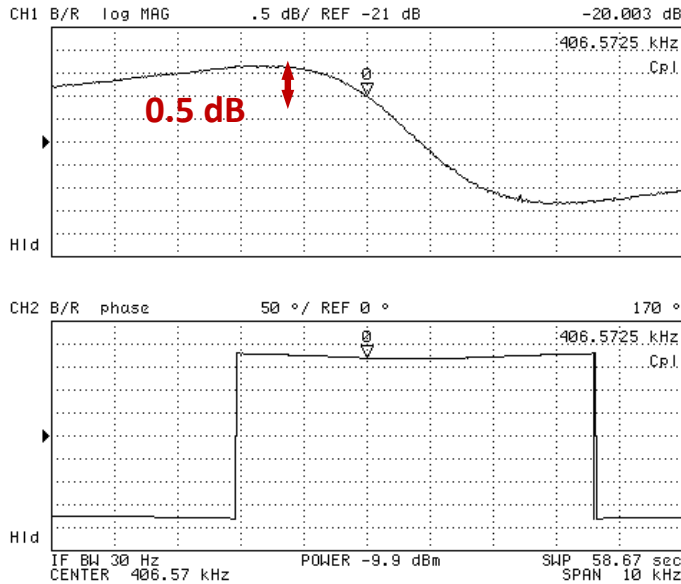


Figure 6-13: The test result of parylene coated device. Resonance frequency increased after parylene coating. This means parylene coating does not only increase the damping coefficient also increases the spring constant

Q and resonance frequency of the device under test is measured as 93 and 407 KHz respectively. The transconductance at the resonance frequency was measured as 32 nA/V. Although decrease of current and Q is expected, resonance frequency unexpectedly 23%.

After this test, liquid injected inside the microchannel of device under test and resonance characteristics was measured. In Figure 6-15, the raw data taken from the network analyzer is shown. Although the resonance peak is very small compared to our other results, this is the first raw data in the literature for lateral mode electrostatic resonators.

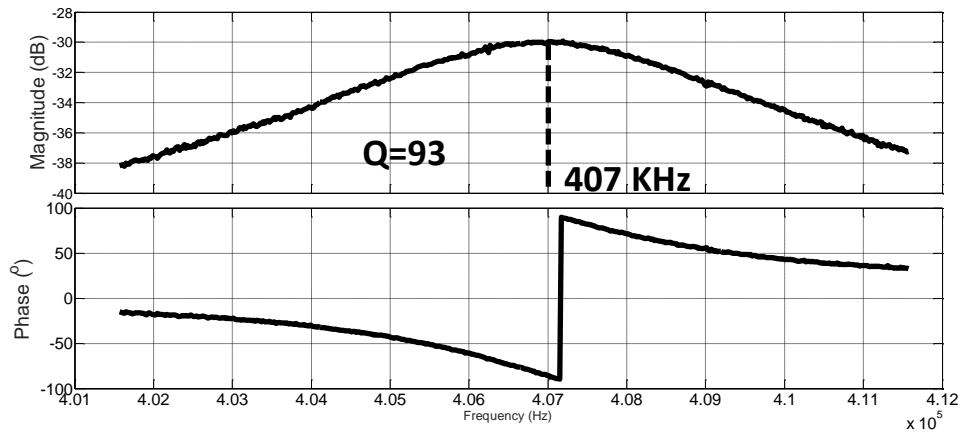


Figure 6-14: Postprocessed test result of parylene coated RBS

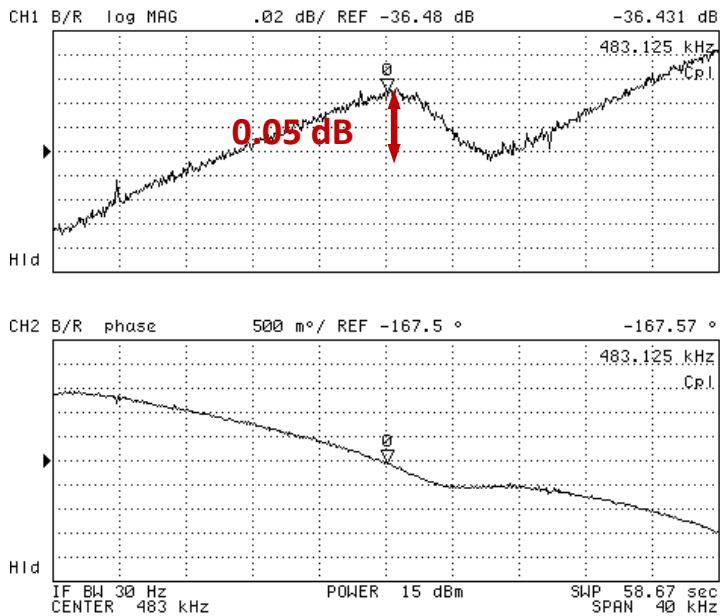
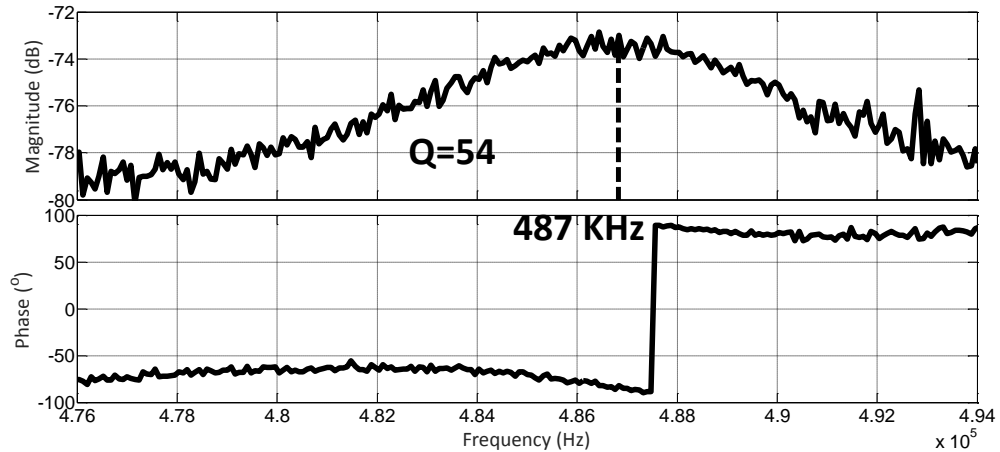


Figure 6-15: Raw frequency response of RBS taken from the network analyzer after liquid injection inside the microchannel

In figure 6-16, postprocessed test result after liquid injection is shown. Q and resonance frequency of the device under test is measured as 54 and 487 KHz respectively. The transconductance at the resonance frequency was measured as 223 pA/V. Although Q decrease of the resonator is expected, the dramatic drop of

transconductance and 20% increase of resonance frequency is not an expected result. However, increase of resonance frequency may be understood since slide film effect includes not only damping but also spring effect. However for fast and easy calculation spring effect of the liquid inside the microchannel is ignored.



*Figure 6-16: Postprocessed resonance characteristics of RBS when liquid injected inside the microchannel*

#### **6.4. Second Harmonic Measurements**

Second harmonic tests are performed using RBS resonators with probe station. The device under test is polarized with 100 Volts and excited with 14.4 dB RF power. In Figure 6-14 the resonance characteristics obtained using second harmonic method is given. As seen from Figure 6-17, 35 dB resonance peak is observed at 10 KHz measurement span. Although 35 dB resonance peak is observed using second harmonic method, only 1 dB resonance peak is observed when the measurement performed at the same condition using the traditional method as seen from Figure 6-18.

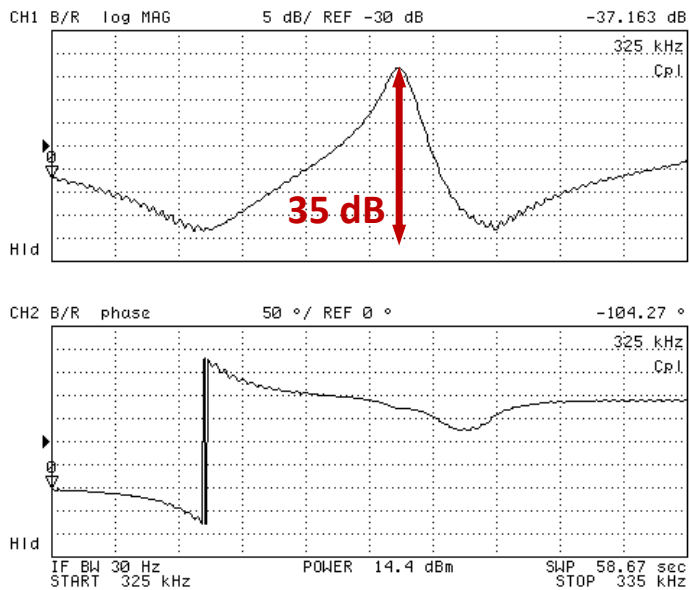


Figure 6-17: Second harmonic characterization of RBS

Under liquid flow, resistive feedthrough current is also expected in addition to the capacitive feedthrough current. However for now we could not make our resonators resonate in liquid environment. Therefore we connected a parallel 6 M $\Omega$  resistance to our resonator. In Figure 6-19 second harmonic and main tone results are shown. Although there is more than 20 dB resonance peak when the measurement is performed with second harmonic method, there is only 0.1 dB resonance peak when the measurement is performed using the traditional method.

To make the conditions more challenging, we connected one 1 pF capacitor parallel to 6 M $\Omega$  resistance. The result is shown in Figure 6-20. We observe 2 dB resonance peak using second harmonic method when 1 pF and 6 M $\Omega$  feedthrough components are connected. On the other hand at the same time we observe only 0.04 dB resonance peak with the traditional method.

Although the performance of second harmonic method decreases due to the practical limitations of the mixer used (i.e. feedthrough of mixer itself), the resonance peak is still higher than the resonance peak of measurement performed

with the traditional method without any additional resistance or capacitance. Therefore 2<sup>nd</sup> harmonic method is a good candidate for eliminating resistive and capacitive feedthrough current without any differential resonator structure or complex circuit design.

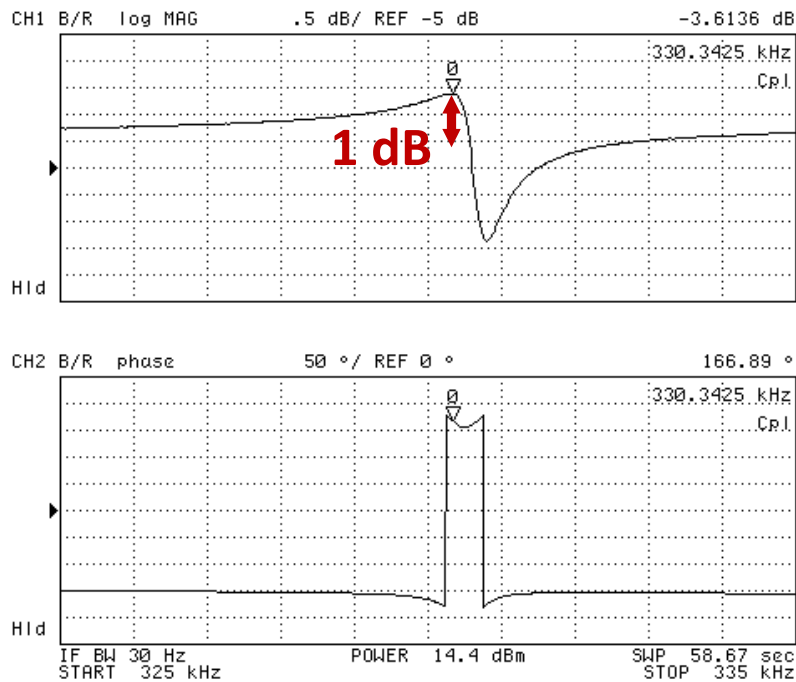


Figure 6-18: Characterization of RBS performed with the traditional method

The other advantage of second harmonic method is enhancement of Q. Q is one of the most important parameters in mass sensors. Therefore a resonating system with higher Q is more desirable since it increases the minimum mass to be measured. The Q of system increases 66% theoretically. Experimentally second harmonic resonance data is subtracted from the second harmonic feedthrough data and Q is calculated as 971 as shown in Figure 6-18.

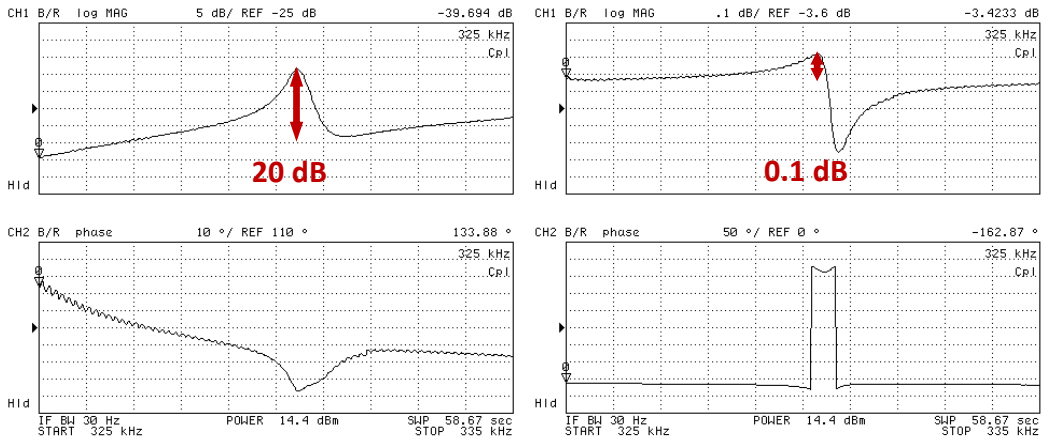


Figure 6-19: Characterization of resonators with second harmonic method (left), and the traditional method (right) when an external  $6\text{ M}\Omega$  resistance is connected between the drive and sense electrodes of the resonator

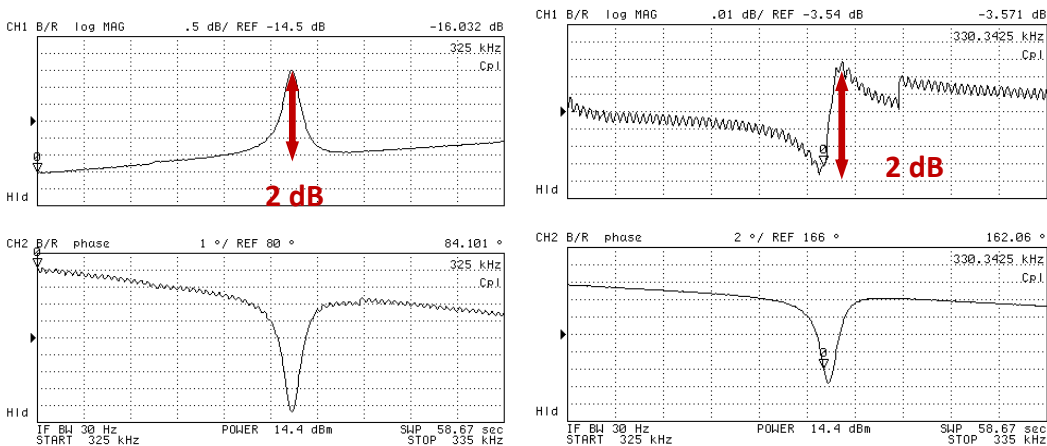


Figure 6-20: Characterization of resonators with second harmonic method (left), and the traditional method (right) when an external  $6\text{ M}\Omega$  resistance and  $1\text{ pF}$  capacitor is connected between the drive and sense electrodes of the resonator

The mechanic Q of the same resonator is measured as 590. Utilizing second harmonic method Q of resonating system is increased to 971 which is 65% higher

than the mechanical Q of the resonator. The enhancement measured is consistent with the calculations.

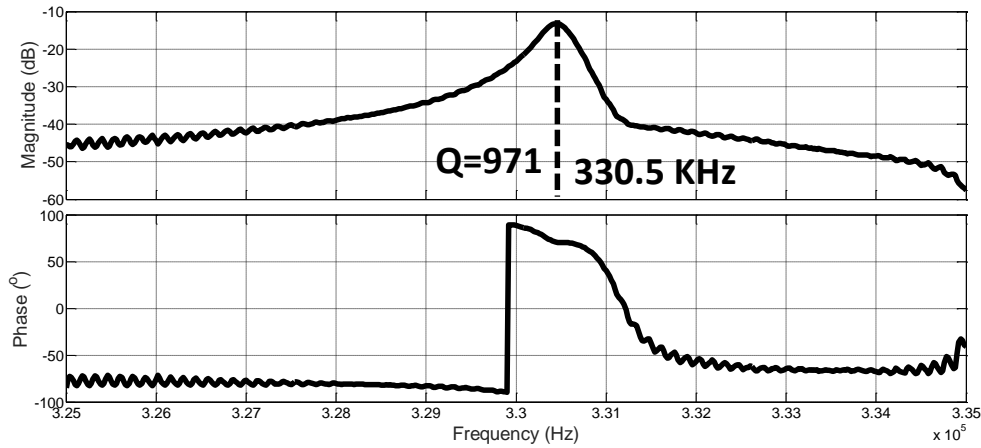


Figure 6-21: Postprocessed data extracted from second harmonic measurements

## 6.5. Conclusion

As a result, designed resonators are characterized using different test setups. Although test results are not exactly the same with simulations, the results are quite close to the simulation results. However to be able to compute Q and transconductance of the system, the other damping mechanisms should also be considered. Furthermore effect of parylene coating is observed in the tests. Q of RBS dropped to 93 from 590 after parylene coating. Moreover its resonance frequency increased to 407 KHz which was an unexpected result. This may be due to increase of spring constant because of parylene coating. After testing parylene coating RBS, liquid injected inside the microchannel of RBS and resonance observed at 480 KHz with 54 Q. This is the first time observation of resonance in liquid without postprocessing. In Figure 6-22, test results of RBS are shown and resonance characteristics are put in the same graph. Drop in Q and output current and increase of resonance frequency is seen clearly. Q drop in parylene coating

and liquid injection cases are expected and were calculated numerically before. On the other hand, although current drop after parylene coating was in expected range, in liquid current decrease are much more dramatic than the expectation. Resonance frequency increase after liquid injection was an unexpected situation but liquid inside the microchannel behaves as both spring and damper. Because of this reason resonance frequency increase may be expected. However as seen from Figure 6-22, test results are not completely consistent with the simulations. Resonator model should be upgraded for better estimations of performance of resonators.

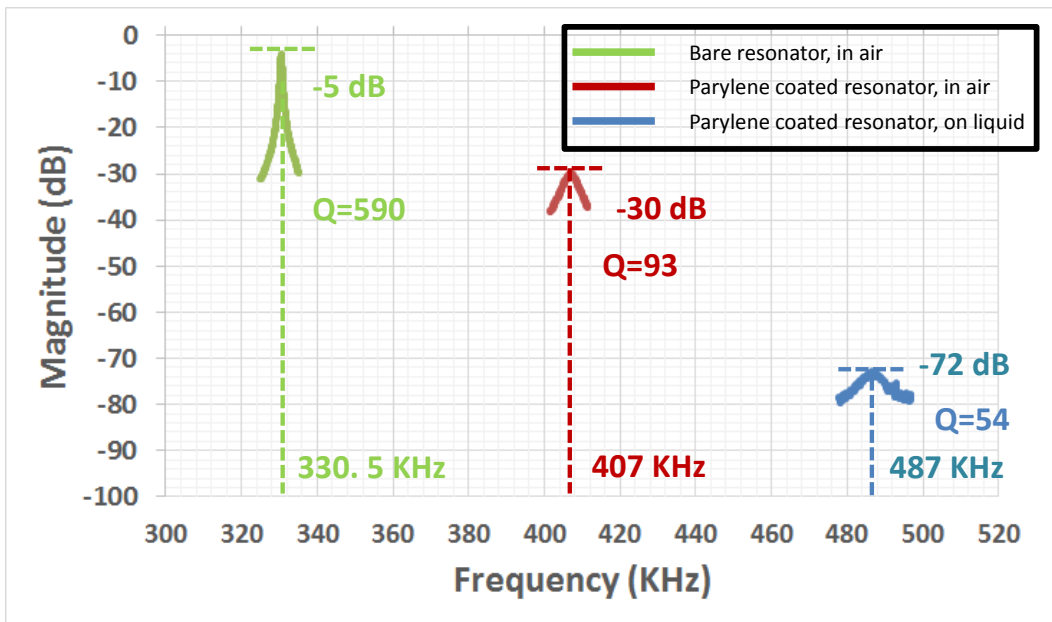


Figure 6-22: Resonance characteristics of RBS under different conditions

Moreover it is shown that second harmonic term is useful for the environments where capacitive feedthrough current is too high and resistive feedthrough current is observed. The proposed method works even extremely high feedthrough currents. It was shown that resonance peak increased from 1 dB to 35 dB with this method. Furthermore the proposed method, Q of the resonating system enhanced 65%. In Figure 6-23, postprocessed test results of RBS with the traditional method

and second harmonic method. Although 10 dB gain decrease is observed in second harmonic method, 65% Q increase of systems are shown clearly from the figure.

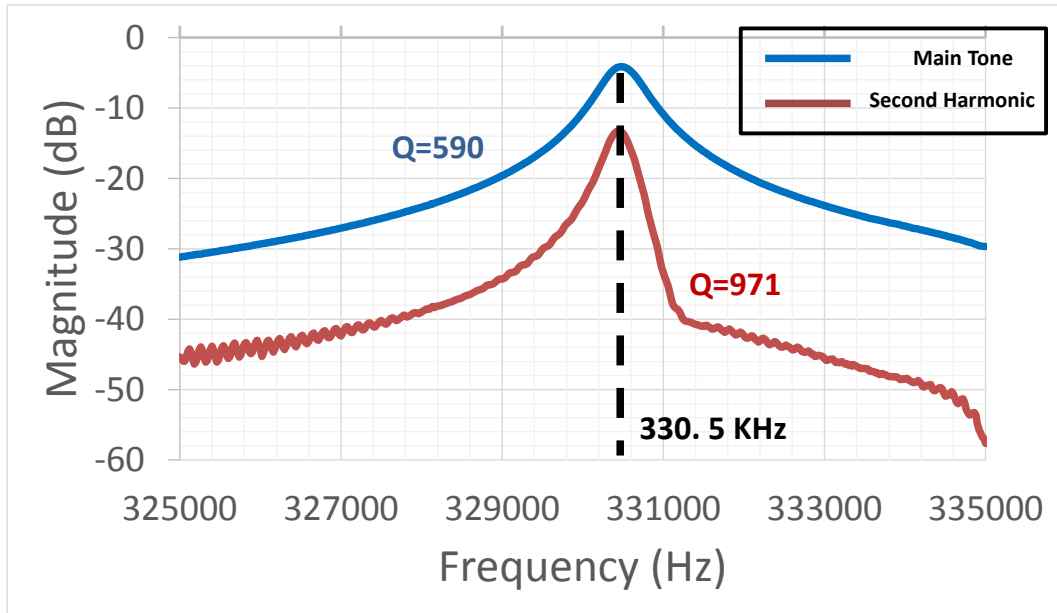


Figure 6-23: Postprocessed test results of RBS in air environment with the traditional method and second harmonic method



## **CHAPTER 7**

### **CONCLUSION AND FUTURE WORK**

In this thesis, implementation of resonators embedded on top wall of a microchannel for biosensing applications and a new read-out technique for performance improvement of designed resonators. Although the intended application of these resonators is CTC detection, the designed resonators may be utilized a variety of applications such as bacteria detection, cell growth observation or chemical analyte sensing in liquid or gas.

The research conducted can be summarized as follows:

- Theory of micro-resonators is studied in detail and resonating devices are modeled using a mass-damper and spring system.
- Electrostatic actuation and sensing mechanisms are studied. Design parameters affecting sensing current are identified. Nonlinearity sources of actuation and sensing mechanisms are also studied and effect of second harmonic component at the output is analyzed. Mass, damping ratio and spring constants are formulized for future designs. Design parameters affecting the Q and transconductance of resonators are also studied. As a result four new resonator structures designed taking damping into account are proposed.

- A new read out method is developed to measure second harmonic at the output to eliminate feedthrough current and enhance Q of resonating system.
- Designed resonators are fabricated using . The designed devices are fabricated using silicon glass process with anodic bonding and parylene bonding methods.
- A read-out circuit for test of resonators is designed using commercial components. Using this circuit both main tone and second harmonic measurements can be performed.
- Designed resonators are tested in air.

As a result achievements and outcomes of this thesis can be listed as follows

- Designed resonators are fabricated using silicon-glass anodic bonding method in METU MEMS Research and Application Center. In this fabrication familiarity to lithography processes and equipment, wet etching of SiO<sub>2</sub>, glass and metals, lift-off process, PECVD process, DRIE, anodic bonding and parylene coating process is gained.
- Designed resonators are tested using different test setups. It is seen that, calculated resonance frequencies are consistent with the test results. However Q and output current are not exactly consistent. In some designs output current is ten times lower than the calculated ones. These results show that, other damping mechanism should also be taken into account and the resonator model should be improved further.
- Second harmonic method is verified using newly designed resonators. Utilizing this method, resonance peak increased to 35 dB from 1 dB. Moreover resonance was observed even virtual 1 pF capacitive and 6 M $\Omega$  resistive feedthrough is connected to the resonator. Furthermore 65% Q

enhancement in resonating system has accomplished. A patent application for this method was filed [49]

- Effect of parylene coating on resonators was observed. Q decreased from 590 to 93 in RBS. However unexpected resonance frequency increase was observed. It is observed that, parylene coating makes springs stiffer and increases the spring constant.
- Liquid injected inside the microchannel and observation of resonator directly from network analyzer is achieved. This is the first time observation of resonance while the microchannel is filled with liquid. Q drop is observed as expected in this situation. However, increase in resonance frequency is observed under this condition as well. This situation can be explained as the liquid inside the microchannel does not only increase the damping coefficient but also behaves as spring and increase spring constant. Modeling of resonators under liquid should be improved further to explain these observations more correctly.

As a result of this thesis it is shown that one type of the designed resonators works properly under liquid flow. Therefore, such resonators may be used for in liquid biosensing applications. Moreover it is observed that second harmonic current is a good solution for resonance frequency tracking even in extremely high feedthrough environment that enhances sensing performances of the sensor systems.

Future work on these sensors may be summarized as:

- Resonator model should be improved further taking different damping mechanisms into account. Furthermore, effect of parylene and liquid injection on the other parameters (spring constant and mass) of resonator should be investigated. The methods to decrease the effect of the other damping mechanisms should be considered.

- Second harmonic tests should be performed under liquid flow.
- Closed loop operation using second harmonic method should be achieved.
- Real time mass measurement tests should be performed.
- Device should be combined a cell separation device for cell detection applications.
- Gold surface of the designed devices should be activated for biosensing applications

## REFERENCES

- [1] J. L. Lopez, J. Verd, A. Uranga, J. Giner, G. Murillo, F. Torres, G. Abadal, N Barniol, "A CMOS–MEMS RF tunable bandpass filter based on two high- Q 22-MHz polysilicon clamped-clamped beam resonators," *IEEE Electron Device Lett.*, vol. 30, no. 7, pp. 718–720, Jul. 2009.
- [2] C. Cassella, G. Chen, Z. Qian, G. Hummel, and M. Rinaldi, "RF passive components based on aluminum nitride cross-sectional Lamé mode MEMS resonators," *IEEE Trans. Electron Devices*, vol. 64, no. 1, pp. 237–243, Jan. 2017.
- [3] S. Sonmezoglu, S. E. Alper, and T. Akin, "An automatically mode-matched MEMS gyroscope with wide and tunable bandwidth," *J. Microelectromechanical Syst.*, vol. 23, no. 2, pp. 284–297, Apr. 2014.
- [4] K. Azgin, Y. Temiz, and T. Akin, "An SOI-MEMS tuning fork gyroscope with linearly coupled drive mechanism," in *2007 IEEE 20th International Conference on Micro Electro Mechanical Systems (MEMS)*, 2007, pp. 607–610.
- [5] J. Chae, H. Kulah, and K. Najafi, "An in-plane high-sensitivity, low-noise micro-g silicon accelerometer," in *The Sixteenth Annual International Conference on Micro Electro Mechanical Systems, 2003. MEMS-03 Kyoto. IEEE*, pp. 466–469.
- [6] M. Y. Chao, A. Ali, S. Ghosh, and J. E.-Y. Lee, "An aluminum nitride on silicon resonant MEMS accelerometer operating in ambient pressure," in *2017 19th International Conference on Solid-State Sensors, Actuators and Microsystems (TRANSDUCERS)*, 2017, pp. 607–610.
- [7] C. D. Do, A. Erbes, J. Yan, K. Soga, and A. A. Seshia, "Vacuum packaged low power resonant MEMS strain sensor," *J. Microelectromechanical Syst.*, vol. 25, no. 5, pp. 851–858, Oct. 2016.
- [8] R. Vermeer, E. Berenschot, E. Sarajlic, N. Tas, and H. Jansen, "Fabrication of novel AFM probe with high-aspect-ratio ultra-sharp three-face silicon nitride tips," in *14th IEEE International Conference on Nanotechnology*, 2014, pp. 229–233.
- [9] E. Bayraktar, D. Eroglu, A. T. Ciftlik, and H. Kulah, "A MEMS based gravimetric resonator for mass sensing applications," in *2011 IEEE 24th International Conference on Micro Electro Mechanical Systems*, 2011, pp.

817–820.

- [10] M. Nagaraju *et al.*, “A fully integrated wafer-scale sub-mm<sup>3</sup> FBAR-based wireless mass sensor,” in *2014 IEEE International Frequency Control Symposium (FCS)*, 2014, pp. 1–5.
- [11] F. Ayazi, “Multi-DOF inertial MEMS: From gaming to dead reckoning,” in *2011 16th International Solid-State Sensors, Actuators and Microsystems Conference*, 2011, pp. 2805–2808.
- [12] D. E. Serrano and F. Ayazi, “MEMS inertial sensors,” in *Resonant MEMS: Fundamentals, Implementation, and Application*, Wiley-VCH Verlag GmbH & Co. KGaA, 2015, pp. 327–353.
- [13] D. D. Shin, Y. Chen, I. B. Flader, and T. W. Kenny, “Epitaxially encapsulated resonant accelerometer with an on-chip micro-oven,” in *2017 19th International Conference on Solid-State Sensors, Actuators and Microsystems (TRANSDUCERS)*, 2017, pp. 595–598.
- [14] T. A. Roessig, R. T. Howe, A. P. Pisano, and J. H. Smith, “Surface-micromachined resonant accelerometer,” in *Proceedings of International Solid State Sensors and Actuators Conference (Transducers '97)*, vol. 2, pp. 859–862.
- [15] J. Bernstein, S. Cho, A. T. King, A. Kourepenis, P. Maciel, and M. Weinberg, “A micromachined comb-drive tuning fork rate gyroscope,” in *[1993] Proceedings IEEE Micro Electro Mechanical Systems*, pp. 143–148.
- [16] M. F. Zaman, A. Sharma, and F. Ayazi, “The resonating star gyroscope: A novel multiple shell silicon gyroscope with sub-5 deg/hr Allan deviation bias instability,” *IEEE Sens. J.*, vol. 9, no. 6, pp. 616–624, Jun. 2009.
- [17] H. Johari and F. Ayazi, “Capacitive bulk acoustic wave silicon disk gyroscopes,” in *2006 International Electron Devices Meeting*, 2006, pp. 1–4.
- [18] A. Alessandrini and P. Facci, “AFM: a versatile tool in biophysics,” *Meas. Sci. Technol.*, vol. 16, no. 6, pp. R65–R92, Jun. 2005.
- [19] R. R. Knight, A. A. Frederick, C. Mo, and W. W. Clark, “Tuning of sol–gel derived PZT MEMS resonators,” *J. Micromechanics Microengineering*, vol. 20, no. 12, p. 125028, Dec. 2010.
- [20] X. Peng, Y. Wen, P. Li, A. Yang, and X. Bai, “Enhanced acoustoelectric coupling in acoustic energy harvester using dual helmholtz resonators,” *IEEE Trans. Ultrason. Ferroelectr. Freq. Control*, vol. 60, no. 10, pp. 2121–2128, Oct. 2013.

- [21] B. N. Johnson and R. Mutharasan, "Biosensors," in *Resonant MEMS: Fundamentals, Implementation, and Application*, Wiley-VCH Verlag GmbH & Co. KGaA, 2015, pp. 391–426.
- [22] B. Ilic, D. Czaplewski, M. Zalalutdinov, H. G. Craighead, P. Neuzil, C. Campagnolo, and C. Batt, "Single cell detection with micromechanical oscillators," *J. Vac. Sci. Technol. B Microelectron. Nanom. Struct.*, vol. 19, no. 6, p. 2825, 2001.
- [23] G. A. Campbell and R. Mutharasan, "Detection of Bacillus anthracis spores and a model protein using PEMC sensors in a flow cell at 1mL/min," *Biosens. Bioelectron.*, vol. 22, no. 1, pp. 78–85, Jul. 2006.
- [24] E. Timurdogan, B. E. Alaca, I. H. Kavakli, and H. Urey, "MEMS biosensor for detection of Hepatitis A and C viruses in serum," *Biosens. Bioelectron.*, vol. 28, no. 1, pp. 189–194, Oct. 2011.
- [25] W. Shu, E. D. Laue, and A. A. Seshia, "Investigation of biotin–streptavidin binding interactions using microcantilever sensors," *Biosens. Bioelectron.*, vol. 22, no. 9–10, pp. 2003–2009, Apr. 2007.
- [26] H. Sharma and R. Mutharasan, "Rapid and sensitive immunodetection of *Listeria monocytogenes* in milk using a novel piezoelectric cantilever sensor," *Biosens. Bioelectron.*, vol. 45, pp. 158–162, Jul. 2013.
- [27] H. Sharma and R. Mutharasan, "*hly* A Gene-Based sensitive detection of *Listeria monocytogenes* using a novel cantilever sensor," *Anal. Chem.*, vol. 85, no. 6, pp. 3222–3228, Mar. 2013.
- [28] D. Maraldo, F. U. Garcia, and R. Mutharasan, "Method for quantification of a prostate cancer biomarker in urine without sample preparation," *Anal. Chem.*, vol. 79, no. 20, pp. 7683–7690, Oct. 2007.
- [29] B. Ilic, Y. Yang, and H. G. Craighead, "Virus detection using nanoelectromechanical devices," *Appl. Phys. Lett.*, vol. 85, no. 13, pp. 2604–2606, Sep. 2004.
- [30] K. Park and R. Bashir, "MEMS-based resonant sensor with uniform mass sensitivity," in *TRANSDUCERS 2009 - 2009 International Solid-State Sensors, Actuators and Microsystems Conference*, 2009, pp. 1956–1958.
- [31] T. P. Burg, M. Godin, S. M. Knudsen, W. Shen, G. Carlson, J. S. Foster, K. Babcock, and S. R. Manalis "Weighing of biomolecules, single cells and single nanoparticles in fluid," *Nature*, vol. 446, no. 7139, pp. 1066–1069, Apr. 2007.
- [32] D. Eroglu, E. Bayraktar, and H. Kulah, "A laterally resonating gravimetric sensor with uniform mass sensitivity and high linearity," in *2011 16th*

- International Solid-State Sensors, Actuators and Microsystems Conference*, 2011, pp. 2255–2258.
- [33] D. Eroglu and H. Kulah, “Quality Factor Enhancement of Lateral Microresonators in Liquid Media by Hydrophobic Coating,” *J. Microelectromechanical Syst.*, vol. 20, no. 5, pp. 1068–1070, Oct. 2011.
- [34] M. Kangül, E. Aydın, F. Gökçe, T. Toral, O. Zorlu, and H. Kùlah, “Design of a Resonator-on-Microchannel (RoM) for Gravimetric Detection Applications in Liquid Environment,” *Procedia Eng.*, vol. 168, pp. 506–509, 2016.
- [35] Kangül Mustafa, “MEMS based resonant mass sensors with feedthrough current elimination for in liquid cell detection applications,” M.S. Thesis, Middle East Technical University, 2015.
- [36] S. M. Heinrich and I. Dufour, “Fundamental theory of resonant MEMS devices,” in *Resonant MEMS: Fundamentals, Implementation, and Application*, Wiley-VCH Verlag GmbH & Co. KGaA, 2015, pp. 3–27.
- [37] J. Zhao, H. Ding, S. Ni, L. Fu, W. Wang, and J. Xie, “High-resolution and large dynamic range electrometer with adjustable sensitivity based on micro resonator and electrostatic actuator,” in *2016 IEEE 29th International Conference on Micro Electro Mechanical Systems (MEMS)*, 2016, pp. 1074–1077.
- [38] E. Aydın, M. Kangul, F. Gokce, O. Zorlu, and H. Kulah, “A novel characterization method for MEMS based electrostatic resonators for Q enhancement and feedthrough current elimination,” in *2016 IEEE SENSORS*, 2016, pp. 1–3.
- [39] Hsin-Hung Liao, Hsin-Hong Shen, Bo-Ting Liao, Yao-Joe Yang, Yu-Chun Chen, and Woei-Wu Pai, “A MEMS electrostatic resonator for a fast-scan STM system,” in *2010 IEEE 5th International Conference on Nano/Micro Engineered and Molecular Systems*, 2010, pp. 549–552.
- [40] G. K. Fedder, “Capacitive resonators,” in *Resonant MEMS: Fundamentals, Implementation, and Application*, Wiley-VCH Verlag GmbH & Co. KGaA, 2015, pp. 119–146.
- [41] C. P. Le and E. Halvorsen, “Wide tuning-range resonant-frequency control by combining electromechanical softening and hardening springs,” in *2013 Transducers & Eurosensors XXVII: The 17th International Conference on Solid-State Sensors, Actuators and Microsystems (TRANSDUCERS & EUROSENSORS XXVII)*, 2013, pp. 1352–1355.
- [42] M.-H. Bao, *Analysis and design principles of MEMS devices*. Elsevier, 2005.

- [43] Ekrem Bayraktar, “Design and implementation of a MEMS based gravimetric detector for cytometry applications,” M.S. Thesis, Middle East Technical University, 2010.
- [44] W. Wai-Chi, A. A. Azid, and B. Y. Majlis, “Formulation of stiffness constant and effective mass for a folded beam,” *Arch. Mech*, vol. 62, no. 5, pp. 405–418, 2010.
- [45] J. E.-Y. Lee and A. A. Seshia, “Parasitic feedthrough cancellation techniques for enhanced electrical characterization of electrostatic microresonators,” *Sensors Actuators A Phys.*, vol. 156, no. 1, pp. 36–42, Nov. 2009.
- [46] M. Kangul, E. Aydin, F. Gokce, O. Zorlu, and H. Kulah, “Analysis and elimination of the capacitive feedthrough current on electrostatically actuated and sensed resonance-based MEMS sensors,” *J. Microelectromechanical Syst.*, pp. 1–7, 2017.
- [47] T. B. Toral, “Development of a high yield fabrication process for MEMS based resonant mass sensors for cell detection applications,” M.S. Thesis, Middle East Technical University, 2014.
- [48] F. Gokce, E. Aydin, M. Kangül, T. B. Toral, O. Sardan-Sukas, O. Zorlu, and H. Kulah, “A parylene bonding based fabrication method for gravimetric resonant based mass sensors,” in *2017 19th International Conference on Solid-State Sensors, Actuators and Microsystems (TRANSDUCERS)*, 2017, pp. 1195–1198.
- [49] E. Aydin, M. Kangül, F. Gokce, Ö. Zorlu, and H. Külâh, “Elektrostatik MEMS rezonatörlerde kalite faktörünü yükselten ve kaçak akımını düşüren ikinci harmonik okumaya dayalı bir karakterizasyon/sürüş yöntemi,” *TPE* 2016/14871, 2016.